Impact and Shedding of Microdroplets on Hydrophilic and Superhydrophobic Surfaces

Hany Gomaa

A Thesis

In the Department

of

Mechanical and Industrial Engineering

Presented in Partial Fulfillment of the Requirements

For the Degree of Doctor of Philosophy (Mechanical Engineering) at

Concordia University

Montreal, Quebec, Canada

May 2015

CONCORDIA UNIVERSITY
SCHOOL OF GRADUATE STUDIES

This is to certify that the thesis prepared,

By: **Hany Gomaa**

Entitled: **"Impact and Shedding of Microdroplets on Hydrophilic and Superhydrophobic Surfaces"**

and submitted in partial fulfillment of the requirements for the degree of

Doctor of Philosophy (Mechanical Engineering)

Complies with the regulations of this University and meets the accepted standards with respect to originality and quality.

Signed by the Final Examining Committee:

_____ Chair
Dr. Deborah Dysart-Gale

_____ Internal Examiner
Dr. Christian Moreau

_____ Internal Examiner
Dr. Hoi Dick Ng

_____ Concordia External Examiner
Dr. Kash Khorasani
Electrical and Computer Engineering Department

_____ External Examiner
Dr. Louis Fradette
École Polytechnique de Montréal, Chemical Engineering Department

_____ Supervisor
Dr. Ali Dolatabadi

_____ Supervisor
Dr. Nabil Esmail

Approved by: _____
Dr. Ali Dolatabadi, PhD Program Director
Department of Mechanical and Industrial Engineering

_____
Dean Dr. Amir Asif
Faculty of Engineering & Computer Science

Date: _____

Abstract

Impact and Shedding of Microdroplets on
Hydrophilic and Superhydrophobic Surfaces

Hany Gomaa, Ph.D.
Concordia University, 2015

The impact and shedding phenomena of water microdroplets on substrates with various wettabilitties are studied in this work. The analysis is aimed at illustrating the differences in behavior between micro, sub-millimeter and millimeter-sized droplets. This involved the evaluation of different parameters such as droplet maximum spreading, contact time, restitution coefficient as well as the critical air velocity for droplet shedding. The work focuses on the results obtained using a hydrophilic aluminum surface, which is the standard material used in aeronautics, and a superhydrophobic surface. After a comparative study on droplet size and surface wettability, the surface roughness effect on the impact of droplets is reported for both substrates. In addition, the adhesion of a sessile droplet on the two substrates is related to its corresponding shedding velocity. The analysis is considered a step forward in studying the behavior of cloud-sized (less than 100 μm) droplets especially on superhydrophobic surfaces. The first step of the current investigation was to design a dedicated test rig to work experimentally with microdroplets. The setup is developed to allow the microdroplet generator, camera, lighting and the designed shedding nozzle to work together without interfering with droplets imaging. Since the impact, deformation/bouncing, and shedding of the microdroplets occur in a matter of microseconds, high speed imaging is implemented. In addition, the MATLAB image processing toolbox is used to quantify the required parameters from the camera raw images by tracking their boundaries. The impact results show that the maximum spreading and recoiling of cloud-sized droplets on superhydrophobic surfaces are reduced when compared to sub-millimeter and millimeter sized droplets. This is depicted to the fact that the roughness of the superhydrophobic surface is in the same order of magnitude as the microdroplet size.

Furthermore, the shedding tests illustrate that the smaller the droplet size, the higher the free stream incipient velocity needed for its shedding. The results also demonstrate the ease to remove impinged droplets from the superhydrophobic substrate when compared to the hydrophilic substrate, even at sub-zero temperatures.

DEDICATED TO MY MOTHER AND MY FATHER ALAA GOMAA
(GOD BLESS HIS SOUL)

Acknowledgements

I would like to take this opportunity to thank very much both my supervisors, Professor Nabil Esmail and Professor Ali Dolatabadi, for their great guidance and flooding continuous support. Their valuable supervision and helpful suggestions were the driving force behind the current work achievements.

Also, I would like to recognize and admire the support given to the current study from the Natural Sciences and Engineering Research Council of Canada (NSERC), Bombardier Aerospace, Pratt & Whitney Canada the Consortium de Recherche et d'Innovation en Aerospatiale au Quebec (CRIAQ),

In addition, the huge contribution of Mousier Norman Hébert through the Norman D. Hébert Fellowship in Micro and Nanotechnology, through which the current work, turned to be a concrete accomplishment.

A special thank you goes to my friends Nick major, Dennis De Pauw, Percival Graham, Ahmad Abo-Mathkour, Ramin Motamadhi, Fadhel Ben Ettol and Moussa Tembely, who helped in different aspects of the current work.

Moreover, thanks for the kindness and great support of Concordia University Mechanical Engineering department administrative staff, especially Mrs. Leslie Hosein.

The CES department chair, Professor Deborah Dysart-Gale, provided me with tremendous help and advice all through the years of my PhD study. No words can describe how thankful and appreciative I am to her remarkable input and overflowing nonstop kindness and support.

Finally, to my family (mother, father, brother and wife) whom I owe everything to, thank you for being there for me at all times. To my father: "I wish you were here to witness this moment".

Table of Contents

Chapter 4

Chapter 5

List of Figures

List of Tables

Nomenclature

Acronyms

CAH	contact angle hysteresis
FPS	frames per second
HSC	high speed camera
LED	light emitting diode
PFV	Photron FASTCAM viewer
SEM	scanning electron microscope
SHS	superhydrophobic surfaces
VOF	volume of fluid method

Symbols

A	droplet frontal area (m^2)
D_o	initial diameter of the droplet (μm)
D_{max}	maximum spreading diameter (μm)
dx	displacement of the three phase contact line (μm)
g	gravitational acceleration (m^2/s)
L_b	length of the droplet contact line (μm)
r	surface roughness parameter (μm)
R_a	average surface roughness (μm)
t	time (s)
t_c	contact time (s)
u	velocity profile inside the boundary layer (m/s)
U_∞	free stream velocity (m/s)
$U_{\infty crit}$	critical air velocity needed for the incipient of motion (m/s)
V_1	droplet impact velocity (m/s)
V_2	droplet rebounding velocity (m/s)

Dimensionless terms and coefficients

Re	Reynolds number
We	Weber number
D_{max}/D_o	maximum spreading coefficient
R_a/D_o	relative roughness
ε	restitution coefficient

Greek Symbols

θ_A	advancing contact angle (°)
θ_R	receding contact angle (°)
θ_s	static contact angle (°)
$\Delta\theta$	contact angle hysteresis (°)
θ^*	apparent contact angle (°)
θ_{min}	minimum contact angle (°)
θ_{max}	maximum contact angle (°)
δ	boundary layer thickness (μm)
γ	surface tension (mJ/m^2) or (mN/m)
γ_{ls}	liquid-solid interfacial energy (mJ/m^2) or (mN/m)
γ_{lv}	liquid-vapor interfacial energy (mJ/m^2) or (mN/m)
γ_{sv}	solid-vapor interfacial energy (mJ/m^2) or (mN/m)
ρ	fluid density (kg/m^3)
μ	viscosity (Pa.s, N s/m^2)

Chapter 1

Introduction and Literature Review

1.1 Background and motivation

The impact of liquid droplets on different substrates has been a flourishing field of research for over a complete century. Worthington, one of the pioneers, focused on this phenomenon as early as the late 19th century [1, 2]. His work on impingement of water and milk droplets in liquid pools, paved the way for understanding the behavior of droplets impact. He was able to observe droplets bouncing, resting on a liquid pool, splashing and jetting due to cavity collapse. This can be illustrated in Figure 1.1. Nowadays, novel complex high speed imaging equipment combined with advanced image processing algorithms allow for much better viewing of the details of the impact process. As a result plenty of new discoveries on droplets behavior were achieved. However, several unresolved issues are yet to be addressed.

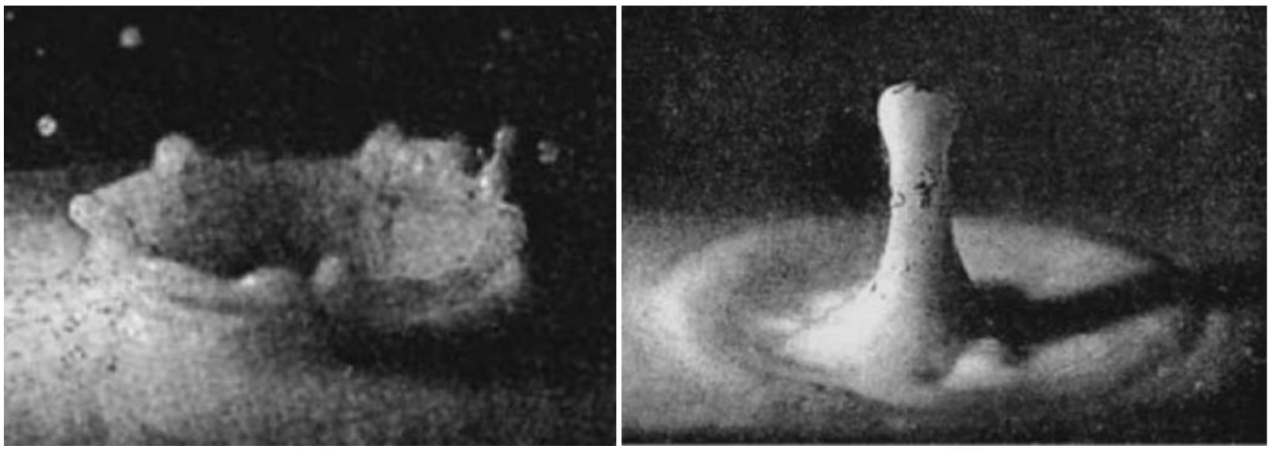

(a) (b)

Figure 1.1 Water droplets impacting a mixed pool of water and milk (a) crown formed after impact and (b) Worthington jet rising [2]

The accumulation of water droplets on surfaces occur naturally, as observed with rain drops on different objects. This accumulation starts by the impact of a single droplet on a dry surface which is then followed by the coalescence of several other droplets. Such criteria exist in several industrial applications that include ink jet printing [3-5], spray coating [6-8],

painting [9, 10], deicing [11-13] and the fuel cell [14-16]. Research studies are directed towards comprehending the relationship between impact parameters and its outcome results [17-19]. The impact and accumulation of water droplets can also be unfavorable as they might lead to many problems. This is especially true when accompanied by wind shedding of the accreted drops. This can lead to the erosion of building facades [20], erosion of gas turbine engines, and at a much larger scale soil erosion [21]. These negative consequences are elevated when freezing conditions exist and the threat of icing is added. The buildup of ice on power lines [22-25], or wind turbines [26, 27], or aircrafts [28, 29] could lead to very dangerous conditions. The consequences of ice accretion on an aircraft include a loss of lift, an increase in drag force, and possible damage of control surfaces or blocking of mechanical parts (e.g. carburetor icing) [28, 29]. All of which can lead to fatal catastrophes, as can be seen in Figure 1.2.

Figure 1.2 Accumulation of snow on the wing of an airplane leading to a deadly crash [30]

In order to prevent such disasters, researchers continuously look for ways to prevent the undesired impingement and accumulation of droplets. Imitating a wide variety of water repellent surfaces that are easily found in nature can help in such a task. For example, the lotus leaf has excellent properties regarding water repellency and mobility. Accordingly, the impacting water droplets bounce and roll off its surface removing the attached dust and dirt particles. This is achieved by the slight tilt of the leaf surface and defines its self-cleaning feature, see Figure 1.3. In 1992, the ‘Lotus concept’ was introduced [31-33] through Scanning Electron Microscopy

(SEM). Since then, the lotus leaf became the prototype for water repellency and self-cleaning properties. In addition, water repellency can also be found in the large wings of insects, which are unable to clean their wings, such as butterflies and dragon-flies [34]. Accordingly, the lotus effect works in this situation to preserve the flight capability of those insects as well as cleaning and removing particles [35].

Figure 1.3 Droplets rolling over a highly repellent lotus leaf [36]

Recently, the lotus leaf effect has been implemented in the production of highly water repellent surfaces [37] where bouncing, rolling and droplet shedding are enhanced in order to protect exposed structures. This is especially necessary when icing conditions exist [38-41]. This is illustrated clearly in Figure 1.4, which describes a substrate with different water repellent characteristics. On the left side of the substrate, the surface is aluminum. Because of its low water repelling properties, the aluminum surface accumulates a considerable amount of ice. The right side of the substrate is superhydrophobic i.e. water repellent, that managed to stay almost entirely ice-free. This shows a huge potential for such repellent surfaces to be applied in different industrial applications such as in aeronautics. Aircrafts are generally designed to fly in icing conditions consisting of droplets of different sizes. Starting from cloud-sized droplets (less than 100 μm) and ending by millimeter-sized droplets. Accordingly, an enormous range of droplet

sizes needs to be considered while studying ice related processes. Furthermore, the types of ice accretion on different exposed surfaces in aeronautics can be classified according to the size of droplets causing it, where glaze ice is obtained by large droplets and rime ice by smaller droplets [42].

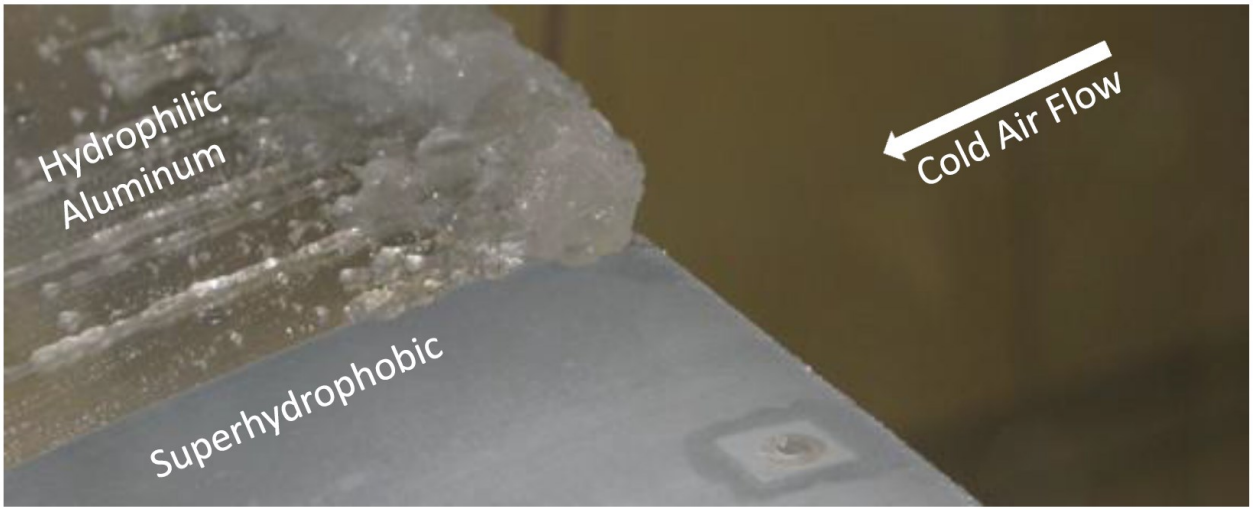

Figure 1.4 Al surface accumulating ice and a water repellent surface in icing conditions [43]

In order to define the exact mechanism of ice accumulation on surfaces, the impact of droplets on such surfaces must be understood. This begins by defining a droplets' size range to test. In such context, the majority of experimental researches are done on sub-millimeter or millimeter-sized droplets. This is mainly due to the experimental feasibility of working with such large sized droplets [44-46]. Moving down to smaller microdroplets makes the impact on solid surfaces more complicated to control, visualize and study [47, 48]. Accordingly, limited experimental analyses have been done for droplets in the cloud-size range, although being responsible for plenty of ice related problems in aeronautics. This was the main motive behind focusing the current project on experimentally analyzing the impact dynamics and shedding of cloud-sized droplets. In addition, more light is shed on the difference in behavior between cloud-sized, sub-millimeter and millimeter-sized droplets upon their impact and shedding on water repellent and non-repellent surfaces.

The complexity of studying droplet impact and shedding require understanding of several issues. Among many others it needs in depth understanding of surface wettability, droplet impact dynamics and droplet shedding mechanism. This chapter is dedicated to explaining these issues

through summarizing the previously related works in order to provide a background for understanding the current accomplished results regarding droplet impact and shedding. The literature review is divided into three different parts; (i) surface properties (i.e. wettability), droplets (ii) impact dynamics, and (iii) shedding phenomena.

1.2 Surface wettability

The wettability of solid surfaces with regards to their interaction with water droplets is characterized as either hydrophilic (wetting) or hydrophobic (non-wetting). These refer to the degree of repellency of a given surface to water, which is quantitatively determined using the static contact angle, θ_S. This is the angle attained by the droplet while settling upon the solid surface. A schematic diagram of the static contact angle is illustrated in Figure 1.5. Young [49] described the static contact angle found on a perfectly smooth surface by relating the liquid-solid (γ_{ls}), the solid-vapor (γ_{sv}) and the liquid-vapor (γ_{lv}) interfacial energies, see equation 1.1.

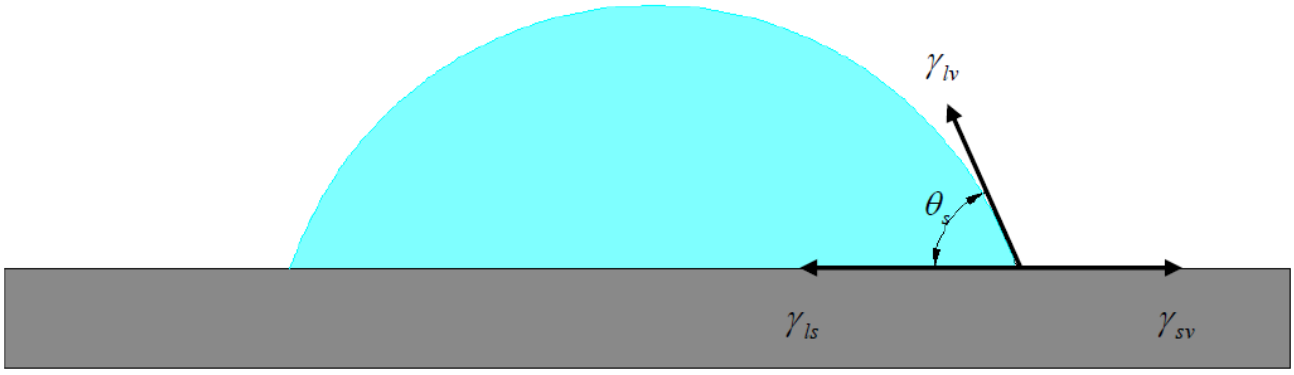

Figure 1.5 Static contact angle

$$\cos\theta_s = \frac{\gamma_{sv} - \gamma_{ls}}{\gamma_{lv}} \tag{1.1}$$

The values of θ_S divide wettability into different regimes, where each regime corresponds to a surface type. For a contact angle $\theta_S < 90°$, a hydrophilic surface is obtained, where surface wetting occurs, as illustrated in Figure 1.6 (a). In addition, contact angles between $90° < \theta_S < 150°$

define a hydrophobic non-wetting surface, Figure 1.6 (b). Lastly for θ_S > 150°, a superhydrophobic surface exists [50, 51], see Figure 1.6 (c). Superhydrophobic surfaces are therefore the most water repellent, with plenty of self-cleaning applications [24-26, 32-35, 48, 50].

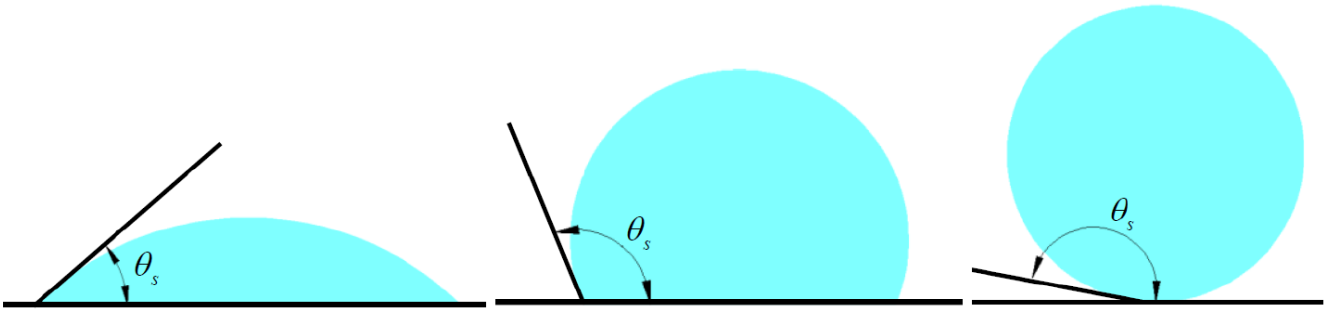

Figure 1.6 Contact angles for (a) hydrophilic, (b) hydrophobic and (c) superhydrophobic surfaces

In addition, a balance of the surface energy variation related to the displacement "*dx*" of the three phase (solid-liquid-vapor) contact line can be obtained, see Figure 1.7. This relation is described in equation 1.2 [52];

$$dE = (\gamma_{ls} - \gamma_{sv})dx + \gamma_{lv}dx\cos\theta_s \qquad (1.2)$$

where *dE* is the change of energy that is produced as a direct result of the displacement *dx* made at the interface. In general, low energy surfaces are non-wetting, while high energy surfaces are considered wetting [53, 54]. Quantitatively a surface energy range between 10 to 50 mN/m describes a non-wetting surface, while a higher surface energy between 500 to 5000 mN/m refers to a wetting one [52].

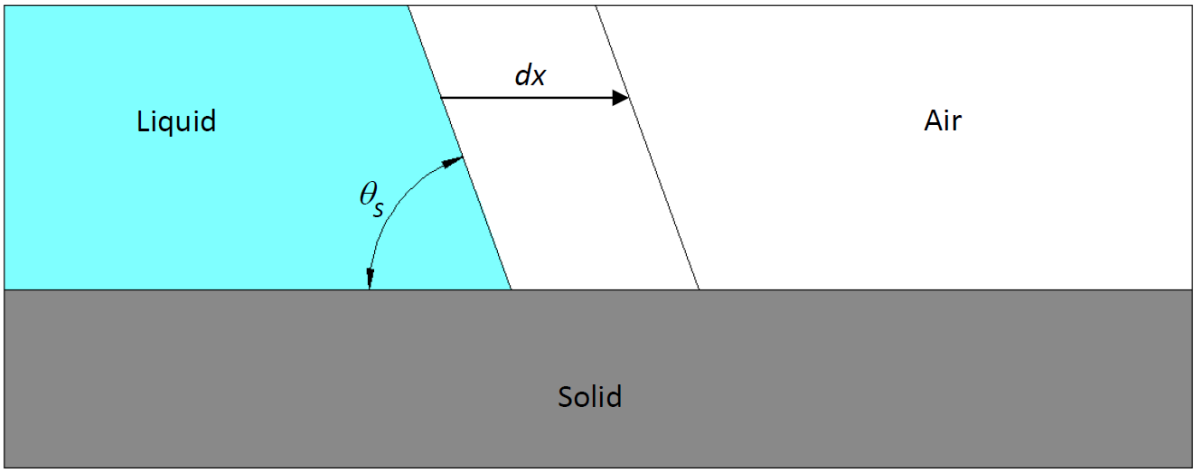

Figure 1.7 Schematic of the three phase contact line displacement "*dx*"

Furthermore, surface mobility is characterized using the contact angle hysteresis (CAH). This is the difference between the advancing, θ_A, and receding, θ_R, contact angles (i.e. $\Delta\theta = \theta_A - \theta_R$), where the smaller the CAH, the higher surface's mobility. For a given surface $\theta_R < \theta_S < \theta_A$. The superhydrophobic surfaces are characterized by having a low CAH (i.e. $\Delta\theta < 10°$) [55, 56]. The advancing and receding angles are illustrated schematically in Figures 1.8 and 1.9 using the tilting plate and volume changing methods, respectively. The tilting plate method requires inclining the plate carrying the droplet, and then measuring the bottom (i.e. advancing) and top (i.e. receding) angles right before the droplet starts to slide. The volume changing method establish the advancing and receding contact angles by increasing or decreasing the volume of the droplet, which is done by injecting a needle in the droplet. This method is used to measure the CAH of small microdroplets where it is not experimentally possible to use the tilting plate method.

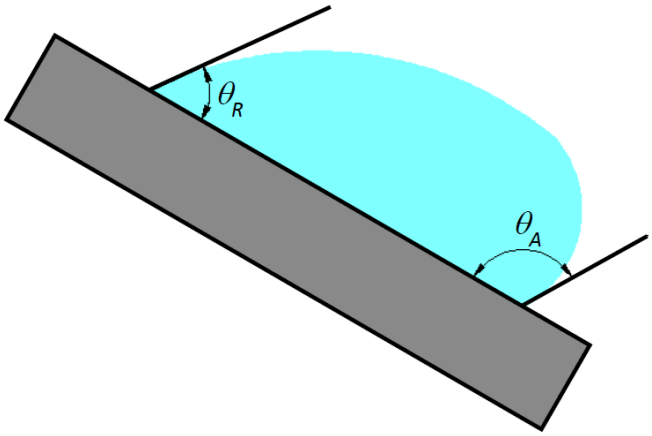

Figure 1.8 Advancing and receding contact angles using the tilting method

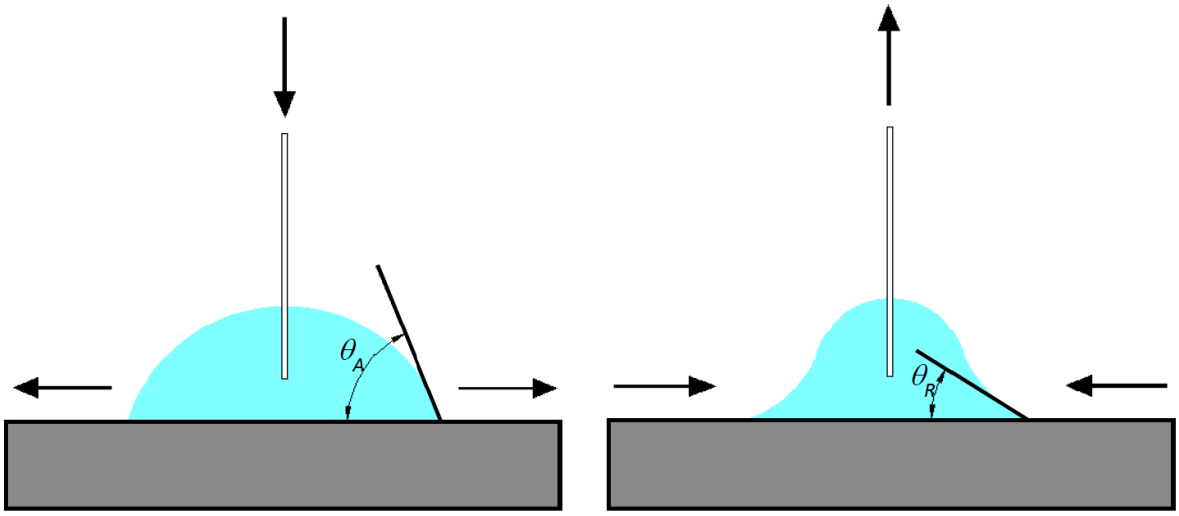

Figure 1.9 Volume changing method (a) advancing and (b) receding contact angles

Surface roughness

The SEM images of a lotus leaf showed several micro and nanoscopic architecture that are covered with wax crystalloids [57]. This demonstrates that the superhydrophobicity of the lotus leaf originates from the combination of unique characteristics of surface roughness and chemical properties. The optimized features, such as the micro and nanoscopic structures found in the lotus leaf surface topography represent the roughness. In addition, the unique properties of the epicuticular wax represents chemical properties [58-60], see Figure 1.10 (a, b, c, d). In addition, there's also the robustness of the lotus leaf (especially on its upper side that is less sensitive to mechanical damage). All grouped together yield a surface with a very high water contact angle (i.e. high water repellency) and a very low roll off angle (i.e. high mobility) [50], see Figure 1.10 (e).

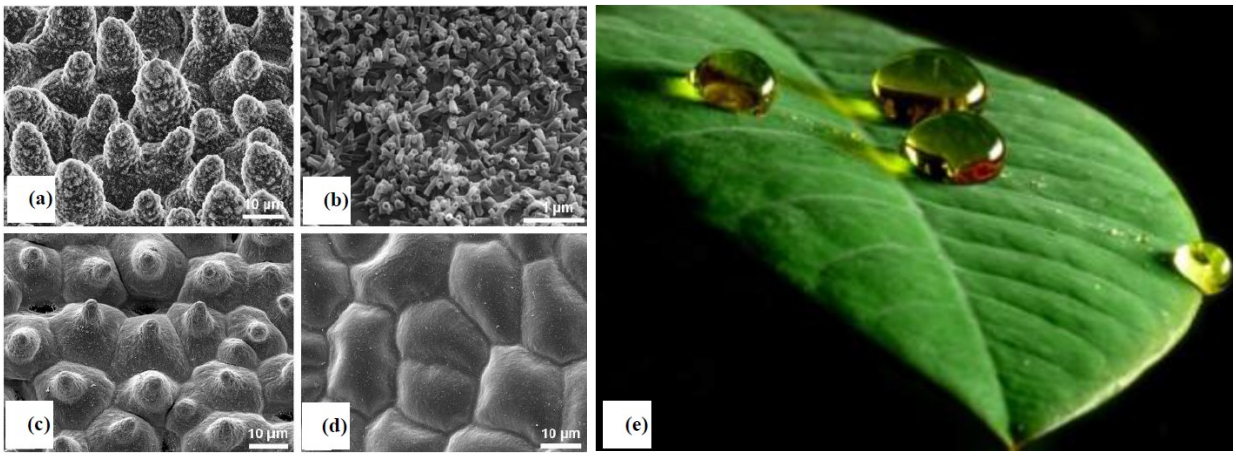

Figure 1.10 (a) SEM of upper lotus leaf side that shows nanoscopic architecture roughness consisting of wax clusters and tubules, (b) wax tubules on the upper leaf side, (c) upper leaf side after drying, where wax tubules are dissolved, (d) dried lotus leaf underside [35] and (e) droplets rolling over a lotus leaf that shows superb repellence and self-cleaning properties on its upper side [61]

It is then important to note that the micro and nano structures (roughness peaks and valleys) on a given surface can change its wetting properties. In general two models exist to describe the settling of droplets on the surface topology. First there is the Wenzel model, which describes a liquid droplet that while resting on a rough surface fills all the gapes by occupying any empty spaces that are found underneath it [62, 63], see Figure 1.11 (a). A droplet at the Wenzel state, suffers from the lack of mobility. Second the Cassie-Baxter model, shown in Figure 1.11 (b), which refers to a liquid droplet that rests on top of the surface irregularities, with gas (air) entrapped in the unfilled area found between the droplet and the surface [64]. Such a droplet has high mobility and can easily roll off the surface. Accordingly, the shape a sessile droplet forms on top of a rough substrate affects its degree of mobility.

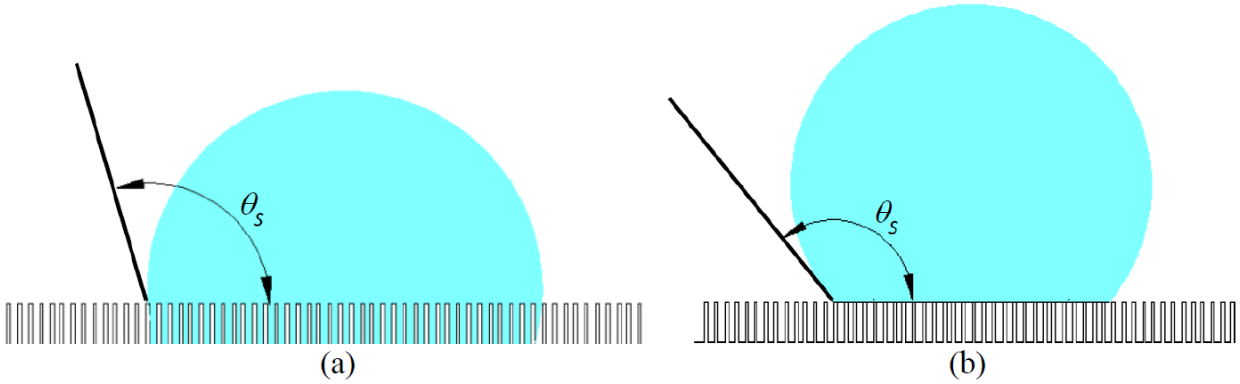

Figure 1.11 Schematic representations of the (a) Wenzel and (b) Cassie-Baxter models

The Wenzel model states that a drop on a rough surface will continue to spread until it reaches an equilibrium state that is characterized by the apparent contact angle θ^* [63], see Figure 1.12. The Wenzel relation is described in equation 1.3 [63],

$$\cos\theta^* = r\cos\theta_S \tag{1.3}$$

where "*r*" is the surface roughness parameter that is a factor of the surfaces geometrical dispute. For any rough surface, "*r*" defines the ratio between the actual to the apparent surface area, i.e. real and projected surface area of the surface [63, 65]. For a rough surface, the roughness parameter $r > 1$, and for a perfectly smooth surface $r = 1$. The Wenzel equation explains that for a hydrophilic surface with $\theta_S < 90°$ then roughness factor "*r*" will decrease the contact angle; hence the surface is more hydrophilic. On the other hand, for a hydrophobic surface, i.e. $\theta_S > 90°$, then roughness enhances hydrophobicity.

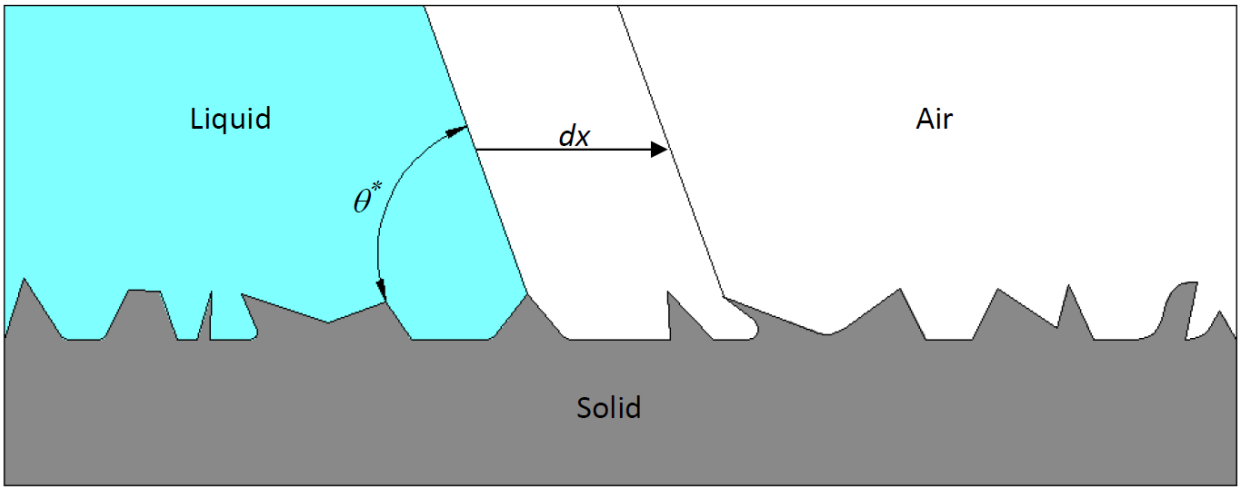

Figure 1.12 Wenzel state showing liquid droplet filling all gaps on a rough solid surface

In addition, for a composite heterogeneous substrate, the Cassie–Baxter model assumes that liquid droplet tends to minimize its energy while settling on a surface with high roughness rather than penetrating into the surfaces structure [64, 66, 67]. For a rough surface, the Cassie-Baxter model modifies the apparent contact angle as follows;

$$\cos\theta^* = r_1 f \cos\theta_S + f - 1 \tag{1.4}$$

where f represents the portion of the solid surface that is wet by the liquid, and r_1 is the roughness of the wetted area. According to the Cassie-Baxter model, air can remain trapped below the droplet, forming air pockets, which increases hydrophobicity as the droplet sits partially on air as illustrated in Figure 1.13. Due to the presence of such an air cushion, the Cassie-Baxter state provides a large contact angle and a small CAH. Consequently, a superhydrophobic surface in such a state is characterized by low adhesion resulting in high water repellency and high mobility [68, 69]. Droplets can then easily roll over the SHS by slight tilting or air flow shedding.

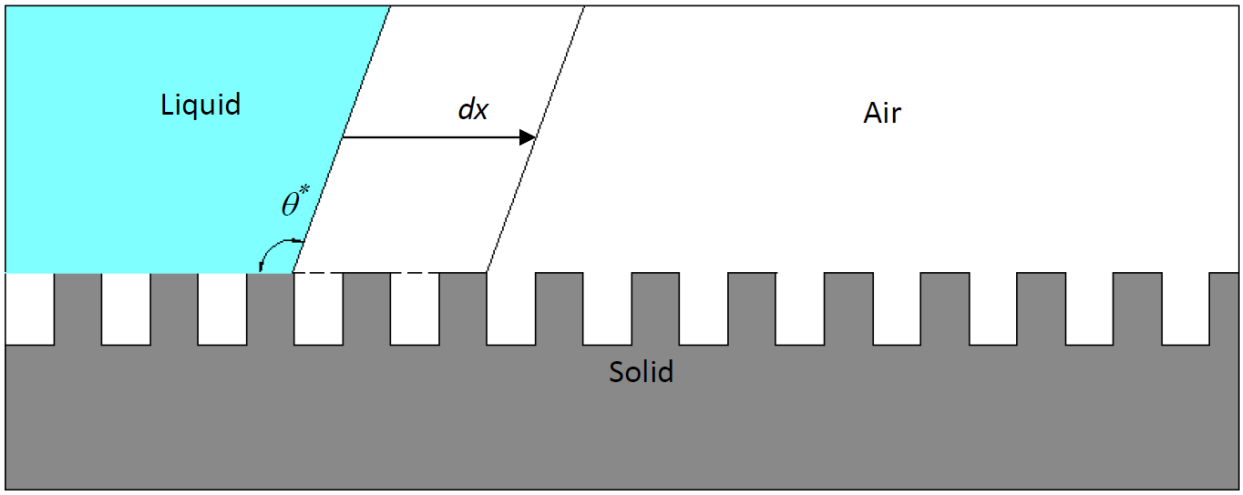

Figure 1.13 Cassie-Baxter state showing air pockets under the droplet

The effect of surface roughness on surface wettability was studied by many researchers [70-74]. Their work on wetting transition can be implemented in different industrial applications. In aerospace, the usage and maintenance of superhydrophobic surfaces can significantly reduce ice formation and accretion on airfoils [75]. This preserves the aerodynamic efficiency of the airplane, which upon ice accretion is considerably reduced by increasing drag and decreasing lift forces [76, 77]. In such context, superhydrophobic coatings have been extensively used for protecting critical aerodynamic components, especially in cold regions where ice accretion is common. Several papers [78-80] showed the growth of this concept for deicing and improving fuel and energy consumption.

1.3 Droplet impact

A significant amount of work has been done experimentally [81-86] and numerically [87, 88] to understand the details of the dynamic droplet spreading on a solid surface with different wettabilitties [44, 45, 89-91]. Droplet impact generally follows two steps. The first step occurs when the droplet loses its kinetic energy during spreading over the surface where the viscosity plays the major role; see Figure 1.14 (a) and (b). Secondly, the droplet starts to recoil due to surface tension force [92], see Figure 1.14 (c) and (d).

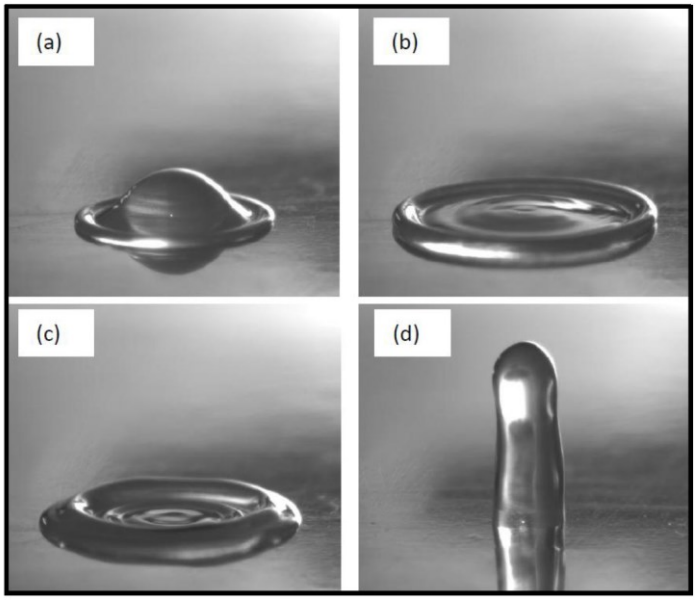

Figure 1.14 Impact of a millimeter water droplet at its (a) initial stage, (b) spreading phase, (c) recoiling phase and (d) vertical liquid jet after recoiling [93]

The detailed result of the impact process can vary according to several parameters, such as fluid viscosity and surface tension and the droplet's velocity just before impact [83-94]. A primary prediction of the impact result can be deduced through the determination of the substrate properties. For example, oscillation until coming to rest is expected for hydrophilic surfaces, while bouncing after complete recoiling is anticipated for superhydrophobic surfaces. The impact process is best studied using relevant dimensionless numbers, such as the Reynolds and Weber numbers.

Examples of the different morphologies of an impacting droplet are described in Figure 1.15. These generally include deposition, splashing and rebounding. First, deposition occurs when the droplet spreads over the substrate and settles there. Second, as the velocity of impact

increases, prompt splashing can occur where small drops detach from the border of the formed liquid lamella upon spreading. Third, corona splashing that occurs by a reduction in surface tension and detachment of the liquid lamella from the wall. Fourth, receding break up, where the lamella breaks into several fingers that are each capable to further break up due to capillary instability. Finally if the kinetic energy of the impacting droplet manages to further squeeze the liquid upward rebounding occurs. This is divided into partial and complete rebounding. Partial rebounding happens when the droplet remains partly attached to the surface and launches one or two drops at its top. On the other hand, complete rebounding takes place if the droplet detaches completely form the surface as a one whole drop [46].

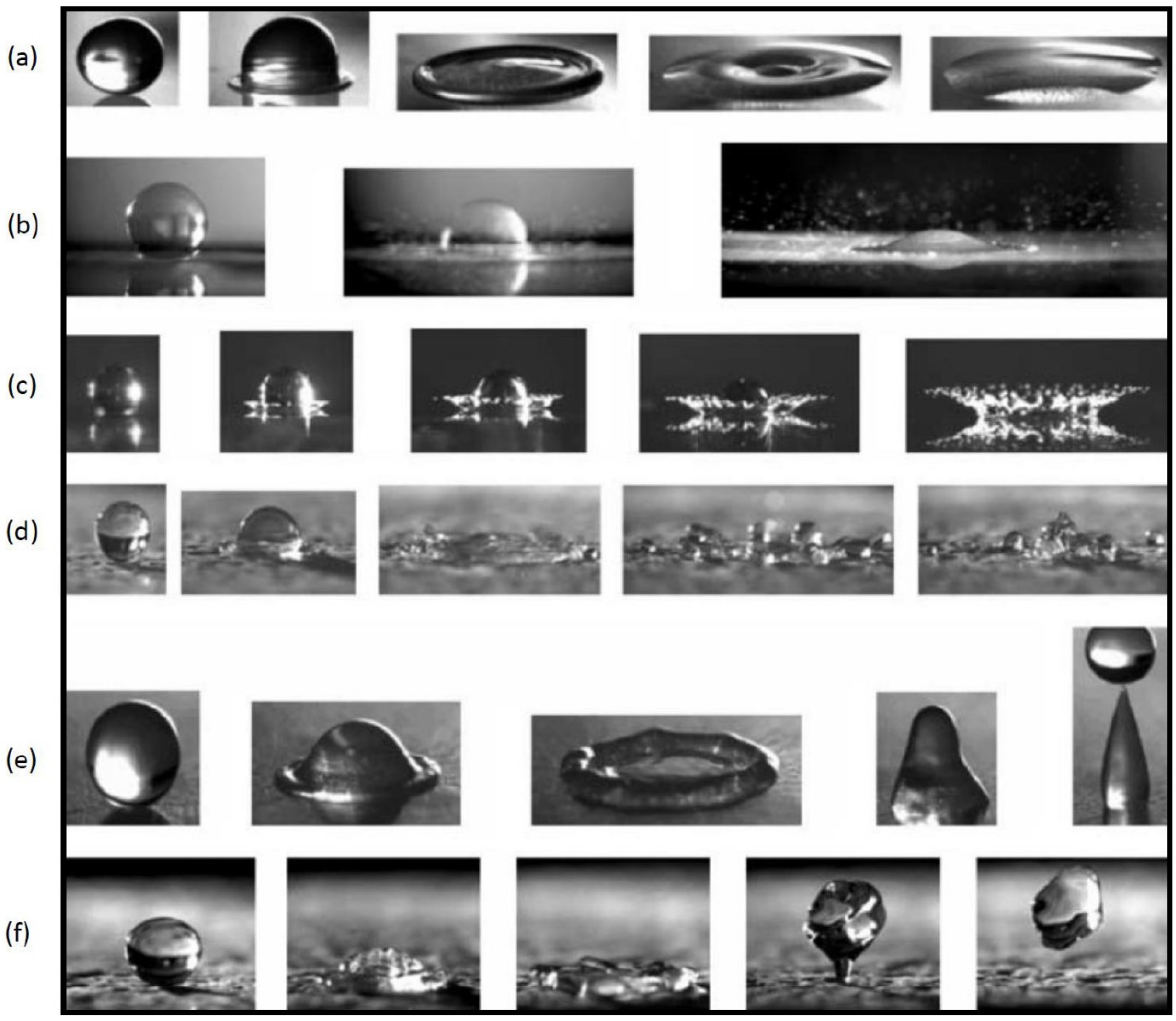

Figure 1.15 Various morphologies of droplet impact on different surfaces showing (a) deposition, (b) prompt splashing, (c) corona splashing, (d) receding break-up, (e) partial rebound and (f) complete rebound [95]

The majority of droplet impact researches have been done using millimeter or sub-millimeter droplets [89-92, 96]. This is especially true for experimental analyses due to the ease of production and repeatability of these large droplets. In addition, it is experimentally feasible for millimeter droplets to attain different impact velocities, for example by simply changing the height of the needle dropping them. Chandra and Avedisian [89] proposed a model in which the dissipated energy was assumed to equate the work done. This model suggested a pancake thickness to represent droplet boundary layer, where a linear velocity distribution across the entire thickness of the droplet was assumed. In addition, the time was considered to be simply the ratio between droplet size and its velocity.

Pasandideh-Fard *et al.* [97] proposed a model that was also based on an energy balance that was later found to predict several experimental outcomes for maximum spreading. They used the maximum contact angle θ_m, which is the droplet's contact angle at maximum spreading, just as the contact line becomes stationary. In their analysis, it was emphasized that the majority of viscous dissipation occurs in the thin boundary layer that is found above the substrate upon which the impact occurs. They also suggested that Chandra and Avedisian's model [89] overestimates the maximum spreading. To recover such an issue, Pasandideh-Fard *et al.* [97] replaced the pancake thickness with the Prandtl-Blasius boundary layer thickness. Such a thickness was obtained inside the droplet according to the stream function of a stagnation point flow. This influenced both the volume of dissipated fluid and the velocity gradient, which were then validated by the obtained numerical results. Furthermore, the dissipation time was improved by finding the dimensionless time based on the maximum spread diameter and velocity required to reach maximum spreading. Both studies [89, 97] simplified the viscous dissipation using a quasi-steady state analysis, and assuming the deformation to be approximated by a spherical cap draining into an expanding disk. Their resulting model showed the effect of the Weber number, the Reynolds number and substrate wettability on the maximum spreading diameter as described in equation 1.5;

$$\frac{D_{\max}}{D_o} = \sqrt{\frac{We + 12}{3(1-\cos\theta) + 4\left(\frac{We}{\mathrm{Re}}\right)}} \tag{1.5}$$

where the maximum value for the wettability related term, $(1-\cos\theta)$ is equal to 2. This is considered negligible at very high Weber numbers. Chibowski [98] proposed a similar model, where the interfacial energy was calculated based on both the advancing and receding contact angles. Ukiwe *et al.* [99] summarized four models for the maximum spreading diameter including the one by Pasandideh-Fard *et al.* [97], which they tried to improve by changing how the liquid-solid interfacial energy was determined. In their model, they used the equilibrium contact angle for interfacial energies calculations. This was modified by Vadillo *et al.* [100] by implementing the dynamic contact angle, which was considered more accurate for fluids with high viscosity.

Clanet *et al*. [101] extended the study of the maximum spreading diameter of millimeter-sized droplets to include superhydrophobic substrates. A similar spreading behavior to the trend shown by Pasandideh-Fard *et al.* [97] was illustrated. They proposed a parameter "*P*", which defines the transition between the two capillary and viscous regimes [101]. As impacting droplet inertia is increased, a transition from capillary to viscous dominated regime can be achieved. Quantitatively the transition parameter is determined as a function of Re and We numbers as, $P=\mathrm{We}/\mathrm{Re}^{4/5}$, where the transition between regimes occurs at $P=1$. This transition cannot be examined using single liquid millimeter-sized droplets because different viscosities and surface tensions are required to cover a considerable range of Re-We space. Accordingly, different liquids need to be implemented. The maximum spreading is controlled by surface tension when impact occurs in the capillary regime, while it is dependent on the fluid's viscosity in the viscous regime. By balancing the drop inertial deceleration with the Laplace pressure drop, a scaling of the dimensionless maximum deformation was given as $D_{max}/D_O \sim We^{1/4}$ [101, 102] which was applicable for both hydrophilic and superhydrophobic surfaces. This scaling was forceful where the surface tension dominates spreading (i.e. capillary regime) [101]. On the other hand, at a viscous dominating regime, the scaling law switches to $D_{max}/D_O \sim Re^{1/5}$ [101, 102]. Clanet *et al*. [101] further proposed an experimental energy conservation analysis to justify that upon droplet impact not all kinetic energy changes into surface energy. Instead, an internal kinetic energy appears within the droplet. Such a conclusion was made by visualizing the flow inside the droplet during impact. This was achieved by enlarging the system into a balloon that is filled with water, were vortices occurred on the sides of the droplet upon its impact, see Figure 1.16. Therefore a

simple energy conservation analysis of the impact process cannot help understanding its impact process [101].

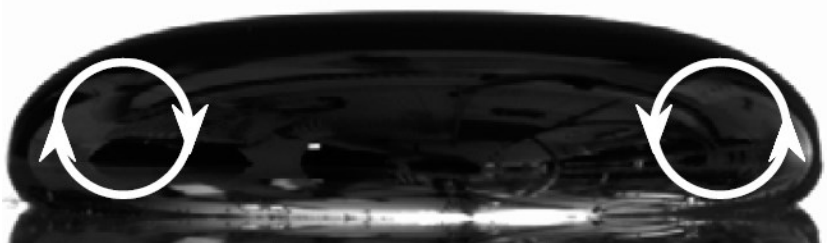

Figure 1.16 Vortices occurring inside a balloon filled with water upon its impact [101]

A theoretical study done at zero or low Re and We numbers to investigate the maximum spreading of spherical droplets was made by Li *et al.* [84]. The physical behavior of the drop surface interaction was captured through a proposed analytical model that contained two different terms to represent viscous dissipation. This is to account for the dissipation made during spreading, and the kinetic energy in the initial droplet using two different coefficients.

In the same line of research on the impact of millimeter-sized droplets on SHS, Chen *et al.* [103] examined the restitution coefficient on a lotus leaf or an artificially prepared surface with controlled roughness. This was obtained by forming a ratio between the droplets incoming and rebounding velocities. However, no explanation to the method of obtaining the detaching velocity was made. Similarly, Richard *et al.* [92] focused their work on studying full bouncing of millimeter-sized water droplets on SHS at low Weber numbers. Both studies [92,103] and many more showed that the restitution coefficient (ε), which is measured using equation 1.6, is a vital parameter to investigate while studying the impact of droplets on SHS.

$$\varepsilon = \frac{V_2}{V_1} = \sqrt{\frac{H_2}{H_1}} \tag{1.6}$$

where V_2 and V_1 are the two perpendicular velocities directly after and before droplet impact on the substrate, respectively. Moreover, H_2 is the height that a droplet reaches after bouncing (furthest distance that it reaches perpendicularly from the substrate) and H_1 is the original height of the droplet, i.e. from where it was dropped. Figure 1.17 illustrates a schematic of these parameters that are used to calculate the restitution coefficient.

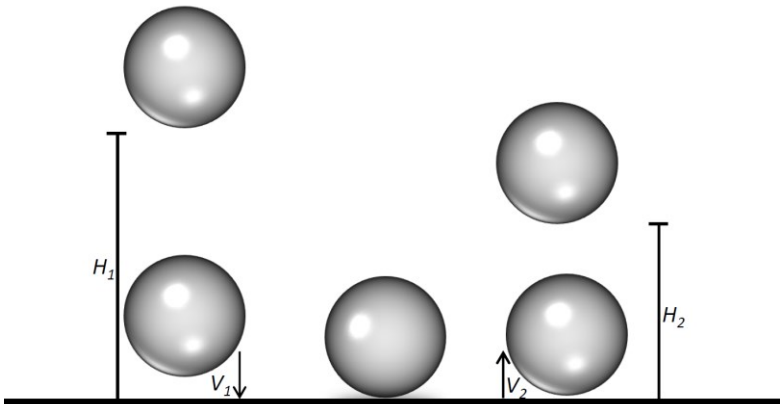

Figure 1.17 Schematic for the measurement parameters of the restitution coefficient

It is vital to note that the majority of work done has neglected the effect of substrates' surface roughness. This can be considered valid since the tested droplets were millimeter-sized and the substrates roughness was in the order of nanometers. Accordingly these models are developed and validated using millimeter-sized droplets, but such analyses might not hold for microdroplets when the droplet inertia is very low and the assumption of thin boundary layer can no longer be valid.

For micrometer-sized droplets, limited number of experimental studies has been conducted. Van Dam and Le Clerc [47] worked experimentally on visualizing the impact of microdroplets with diameters ranging between 36 and 84 μm. Their study focused on capturing the droplet interface shape and oscillation during impact on a hydrophilic glass plates. This was done using flash-videography with a controlled delay time and a substrate space displacement between droplets. In addition, Visser *et al.* [104] extended the analyses for microdroplets impact to include high velocities i.e. up to 100 m/s. They used a new high-velocity droplet generation technique that implements the ultrafast liquid jets formation method described by Tagawa *et al.* [105]. Such a method depends upon laser-induced cavitation, which creates a vapor bubble in a capillary tube due to the focus of a laser pulse with a microscope objective. From the obtained bubble, a shock wave travels to the meniscus forming a liquid jet that breaks up into tiny droplets that carry the same velocity as the jet. Depending upon the desired droplet size, a capillary tube diameter is selected. This capillary diameter affects both the diameter of the produced jet and also its tip velocity [105]. Moreover, for a selected capillary tube, the applied laser energy and the laser focus-meniscus distance were varied in order to provide the required range of velocities

aimed for testing. Implementing small sized microdroplets lowered the Weber number for which the transition, which was previously described by Clanet *et al.* [101], between capillary and viscous regimes occurs, see Figure 1.18. As a result the investigation of such transition could be achieved by using a single liquid. This is because by using elevated impact velocities a sufficient Re-We parameter space was covered. The analysis described quantitatively the maximum spreading diameter of the high speed jetted droplets upon impacting a hydrophilic microscope slide with an average surface roughness $R_a \leq 0.01$ μm.

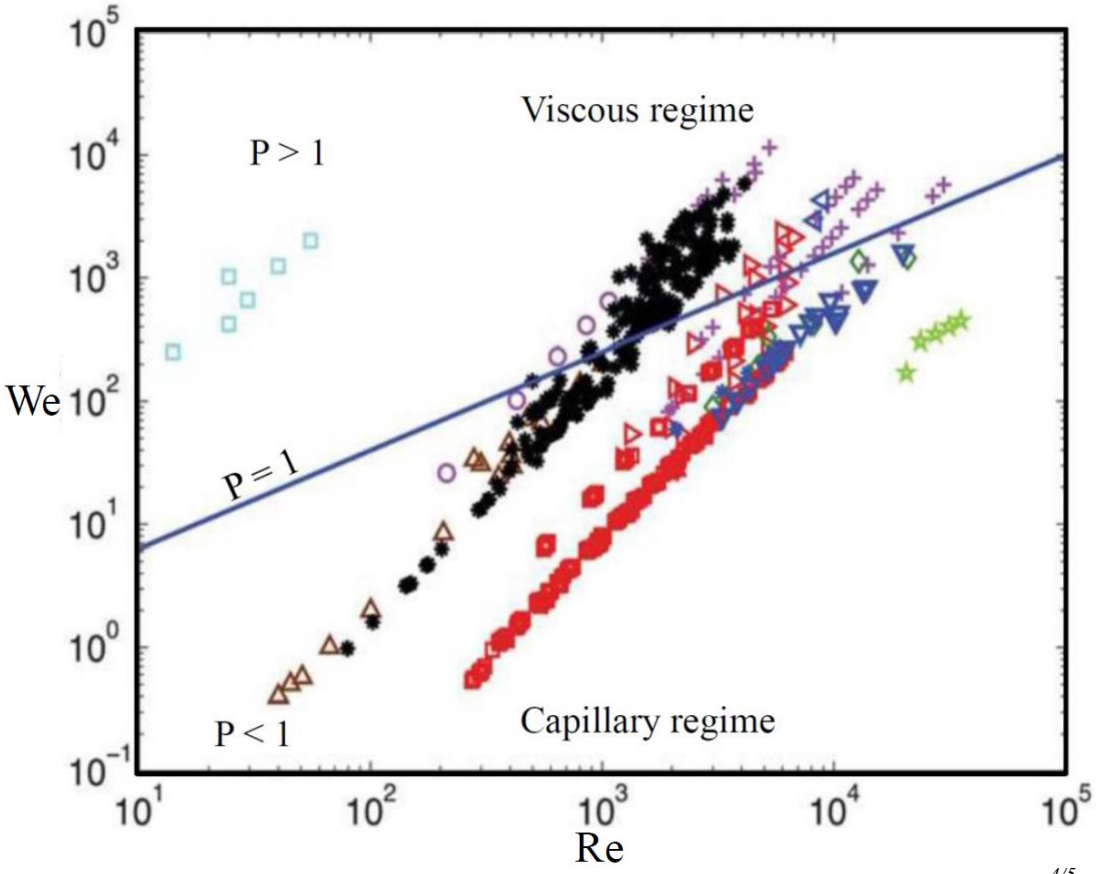

Figure 1.18 Re-We parameter space showing the impact parameter "$P=We/Re^{4/5}$" and transition between Capillary and Viscous regimes [105]

Visser *et al.* [106] then extended their work to describe similarities and differences between millimeter-sized and micrometer-sized droplets upon their impact on both hydrophilic and hydrophobic substrates. Droplet generation method included acoustic oscillations to break down a produced jet into a monodisperse line of microdroplets. Charging of the jet tip, then deflecting the charged droplet by using an electrical field, facilitated having a single reproducible droplet that was received on the impacting plate. The visualization of microdroplets included

both side and bottom views. These images were implemented to develop and validate a numerical model that is intended to study the boundary layer development and the rim size. The proposed numerical model gave a detailed description of the boundary thickness, appearance of dimples and bubble formation inside the droplet upon impact, see Figure 1.19. Bubbles were seen to form inside the impacting droplets for all velocity and size ranges used.

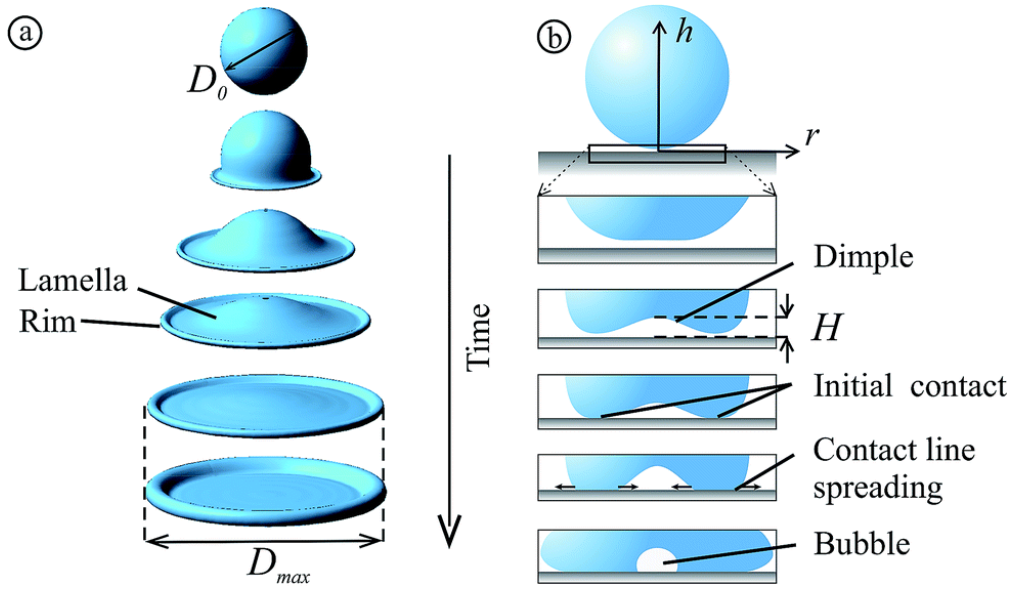

Figure 1.19 Schematic for droplet impact stages [106]

1.4 Shedding of droplets

As mentioned previously, the prevention of droplet impingement on external surfaces is an aim to protect such surfaces from the different harmful consequences of droplets coalescence especially in icing conditions. Even after preparation of a good repellent surface, droplets still tend to find several ways to deposit on it. This is especially true in the case of cloud-sized microdroplets whose size is comparable to the surface roughness of most used substrates. Nevertheless, when the first droplet manages to stick on the surface, it invites several others of different sizes to coalescence on top of it intensifying the problem. Cleaning of substrates by air flow shedding has recently been receiving more attention by researchers to remove impinged droplets and prevent coalescence over external surfaces. Shedding of a droplet refers to the movement induced on a stationary drop by shear flow. This can also be observed in nature when wind slides rain droplets along surfaces after they impact it. This air flow shedding is used practically as a protective method, to prevent the excessive accretion of ice on airfoils for

example. In addition, this flow has several other applications, such as water management in fuel cells, enhanced oil recovery and in driers and condensers. Note that if shedding is applied after the coalescence of several droplets on the surface, then a rivulet is formed. This can be defined as a narrow thin liquid stream flow on a solid surface. A rivulet usually occurs on surfaces with high wettability and exhibits different flow patterns classifying them into static (i.e. no axial velocity in its base state) and dynamic rivulets [107].

Efforts have been made regarding the shedding of a single large millimeter-sized droplet on different substrates. However, due to the difficulty of the experimental visualization of the shedding process, most investigations in the literature are mostly numerical. For simplicity, models were generally focused on simulating low Reynolds number flows in a 2-D model. This avoids elevated computational cost of doing CFD analysis for high fluid volumes at elevated Reynolds numbers. For simplicity, additional assumptions were introduced, such as fully developed flow of tested droplets in the upstream, completely circular contact line [108], linear distribution with circular contact line [109], and ignoring any shear stress found on the side walls of the tested control volumes. Mahé *et al.* [110] described the shedding of an adhered droplet on a solid substrate with pure, contaminated and rough surfaces. The study obtained a critical shear rate for the detachment of different oil droplets using flowing water. Zhang *et al.* [111] focused on shedding of droplets that are found on a fuel cell. Minor [112] explained a droplet shedding criteria while measuring the inlet droplet velocity that is away from the interface. White and Schmucker [113] studied the flow of water in order to pinpoint the critical volume required for runback at three different turbulent velocities. Their terminology defined the word incipient of motion as the runback of the tested drop for a short distance that is followed by a stop. A complex aerodynamic analysis was described but no comprehensive explanation was made on the surface wetting or adhesion properties.

Milne and Amirfazli [114] further studied the shedding of a sessile droplet using air flow inside a wind tunnel for different hydrophobicities, and a large range of droplets volumes. The work studied shedding on hydrophilic (PMMA), hydrophobic (Teflon) and superhydrophobic (Teflon that is coated with itched aluminum) surfaces. Droplets volumes between 0.5 to 100 µl (i.e. D_o = 1000 - 5800 µm) were implemented. Similar to the current study, Milne and Amirfazli [114] defined any property at the incipient of motion, as its value just before the droplet starts to slide over the surface. Measurements of advancing and receding contact angles were made at the

incipient of motion by substituting their values with θ_{max} and θ_{min}. These were considered as another droplet mobility measurement in case of shedding flow. In addition, by multiplying the droplet contact line length, L_b (i.e. wetting length), with $(\cos\theta_{\min} - \cos\theta_{\max})$ a droplet adhesion measurement is obtained. A schematic drawing of an air shear flow on a single droplet is illustrated in Figure 1.20.

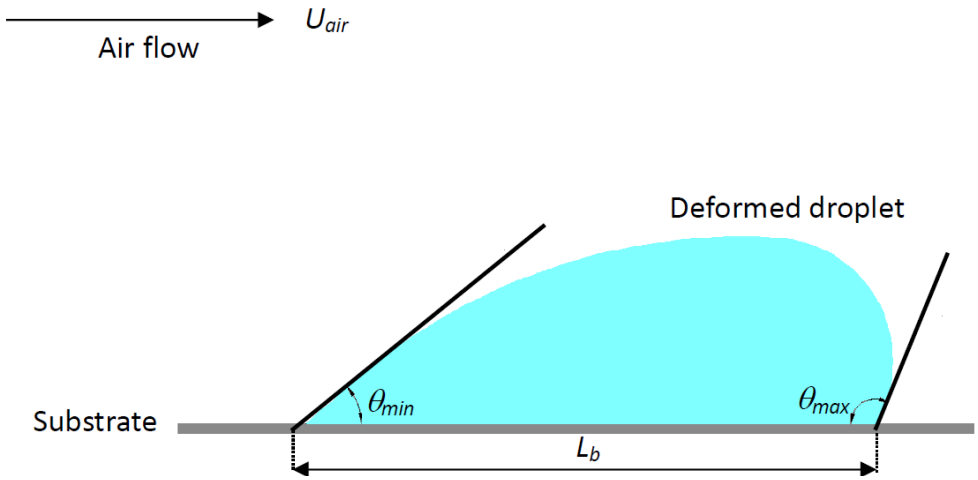

Figure 1.20 Schematic for droplet shedding

The work focused on the effect of substrates' wettability on shedding. [114]. This was based on the in depth experimental and numerical analysis preceded shortly by Antonini *et al.* [115] for the adhesion forces that lie on drops and bubbles subjected to an external force while on top of solid surfaces. A new image based adhesion force analysis (IBAFA) method, which uses multiple images to reconstruct the contact line shape and measure the contact angles, was introduced and implemented for such a purpose. This contact line is further represented using the Fourier cosine series representation that was used to correct the perspective error obtained by using multiple images [115]. Based on this detailed derivation, the shedding of droplets was said to be controlled by the balance between the adhesion force, which is found between the droplet and the substrate, and the drag force applied by the shearing air flow [114]. The adhesion force is controlled by surface tension, contact angles and the shape and length of the contact line. The drag and adhesion forces can be described by equations 1.7 and 1.8 respectively [114];

$$F_{drag} = \frac{1}{2}\rho U^2 A C_D \tag{1.7}$$

$$F_{adh} = kL_b\gamma(\cos\theta_{min} - \cos\theta_{max}) \quad (1.8)$$

where U is the air free stream velocity, A represents the area of the droplet facing air flow and C_D is the drag coefficient. In addition, k is a parameter used to account for the droplet deformation at the incipient of motion. The surface wettability (i.e. contact angles and contact line length), affects the values of both A and C_D. The variation in the droplet's contact angles (i.e. upstream, θ_{min} and downstream, θ_{max}) deforms it during shedding. As a result, the droplet's wetting length (i.e. L_b) is altered. The experiments involved increasing the shedding velocity gradually from 0 up to 30 m/s. Droplet height ranged between 0.9 to 2.5 times the height of the boundary layer, where the droplet was partially exposed to the boundary layer and partially to the free stream velocity. The critical air velocity was seen to increase as the volume of the droplet decreased. Results show that the superhydrophobic surface gave the lowest critical air velocity for runback. This is because the frontal area "A" of the deformed drop increased drag and "L_b" decreased adhesion of water droplets on the SHS. It was then concluded that the wetting properties have the major influence on drop shedding by air flow.

Important issues in literature

Considering all of the above, we can deduce that few attempts were made to experimentally study the impact dynamics of small microdroplets (i.e. diameter range between 40 -100 μm). In addition, limited experimental studies were made on the impact of cloud-sized droplets on superhydrophobic surfaces (i.e. only experiments on hydrophilic and recently hydrophobic surfaces were encountered in the literature). Moreover, droplet shedding has not received the same attention as droplet impact on solid substrates. In such context, limited experimental studies were performed for the shedding of a single cloud-sized droplet on substrates of different wettabilitties (i.e. only large millimeter-sized droplets or rivulets). In addition, the effect of substrate surface roughness on droplet impact dynamics and shedding were either minimized or neglected. Accordingly there is an obvious lack in the literature regarding the experimental analysis of cloud-sized droplets impact dynamics and shedding especially on superhydrophobic surfaces.

1.5 Objectives

The primary aim of the current study is to investigate and analyze the behavior of cloud-sized droplets (less than 100 μm) with regards to impact and shedding on substrates of different wettabilitties. Focus is made on the effect of surface roughness on the obtained results, especially for the superhydrophobic substrate where its average surface roughness is comparable to the size of the cloud-sized droplets. Finally, the behavior of those cloud-sized droplets is to be compared to sub-millimeter and millimeter droplets. The objectives of this work include:

1. Building a dedicated state of the art test rig that enables the study of cloud-sized droplets impact and shedding, under a controlled environment, in a repeatable and reliable manner.

Droplets impact dynamics

2. Analyzing the maximum spreading (i.e. contact diameter) and contact time of the impacting droplets on the different substrates.
3. Investigating the droplets oscillation on the hydrophilic substrate.
4. Studying the bouncing of droplets on the superhydrophobic surface through finding the restitution coefficient.
5. Comparing the results obtained for the small cloud-sized (less than 100 μm) droplets and larger sub-millimeter and millimeter droplets.

Droplets shedding

6. Investigating the shedding of a single sessile microdroplet on the two different substrates using airflow velocities up to 150 m/s.
7. Quantifying the incipient of motion velocity needed for each droplet size (i.e. diameters between 10 - 200 μm).
8. Evaluating and comparing the results obtained for the micro and sub-millimeter droplets with those obtained previously for millimeter-sized droplets.
9. Examining the effect of lowering down the temperature of substrates to sub-zero temperatures (i.e. –7 °C) on the incipient velocity required for shedding of microdroplets.

1.6 Thesis organization

The thesis work is organized as follows;

- Chapter 1 gives an introduction to droplets basic terminologies, substrate wettability, droplet impact dynamic and shedding processes. In addition it provides a critical literature review regarding previous research work on droplets impact dynamics and shedding. This includes illustration of the deficiencies found regarding microdroplets analyses in order to guarantee the novelty of the current project.
- Chapter 2 describes the methodology used to experimentally study the impact and shedding behavior of microdroplets.
- Chapter 3 shows the experimental results obtained for the impact of microdroplets on different substrates while pinpointing the effect of surface roughness, especially for superhydrophobic surfaces.
- Chapter 4 explains the shedding results for the microdroplets on the hydrophilic and superhydrophobic substrates at room and sub-zero temperatures.
- Chapter 5 summarizes the current work and explains the obtained conclusions. In addition it illustrates the future work suggestions for prospective researchers.

Chapter 2

Methodology and Experimental Setup

This chapter underlines the methodology implemented in the current study, where the images of the droplets are captured through high speed photography. The sections to follow will discuss the general experimental procedures, droplet generation, implemented substrates, visualization technique and image processing methods. It also explains the dedicated experimental apparatus used for droplet impact and shedding experiments at different temperatures, the problems encountered and error estimation.

2.1 General experimental procedures

All the experiments are performed by using backlighting. This mechanism works by placing a source of light on one side, the droplet generator in the middle and a high speed camera on the opposite side, see Figure 2.1. The light deflections generated by the droplets are then captured as still images or videos at different frames per second. Such a method is preferred to front lightning, where light is reflected from the object and then enters the camera. This is because during backlighting experiments, the produced light enters the camera lens directly allowing for brighter images. In contrast, the front lighting technique requires a brighter light for the same camera exposure time.

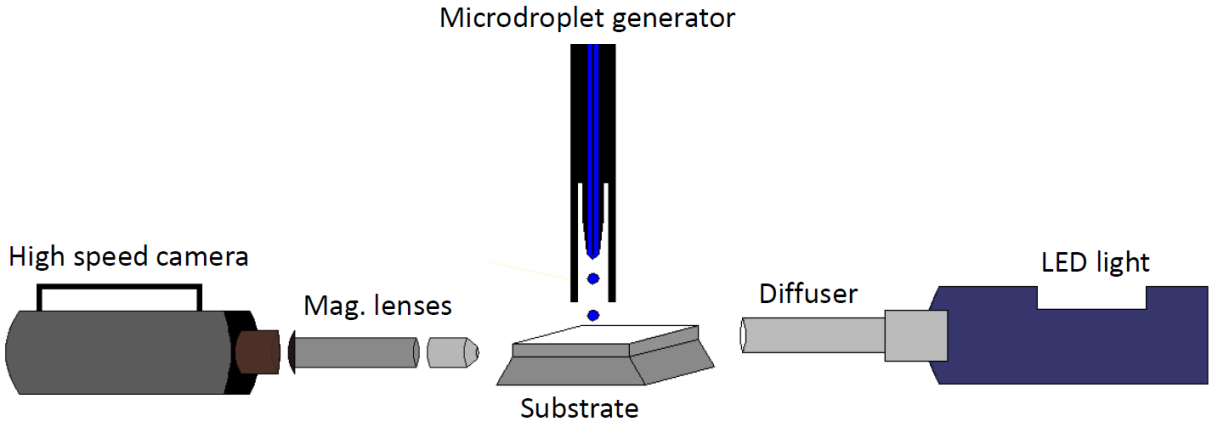

Figure 2.1 Schematic drawing of general experimental setup

One of the main issues controlling the quality of obtained images is the lighting. The experimental illumination is done using an LED light (KL2500, SCHOTT North America, Inc.) source [116]. This is currently the highest intensity for a continuous LED light source. It also carries the advantage of having a fibre optic bundle that is able to carry the produced light away from the actual light engine. This is vital for the current study as it gives the flexibility of directing the light at the area of interest even with very limited available space. It also allows the majority of generated heat to be dissipated at the LED engine itself. Hence, no interference with the experiments, through changing the substrate surface temperature, is allowed. Figure 2.2 describes the general backlighting setup of the high speed camera, micro-dispensing device and LED light source.

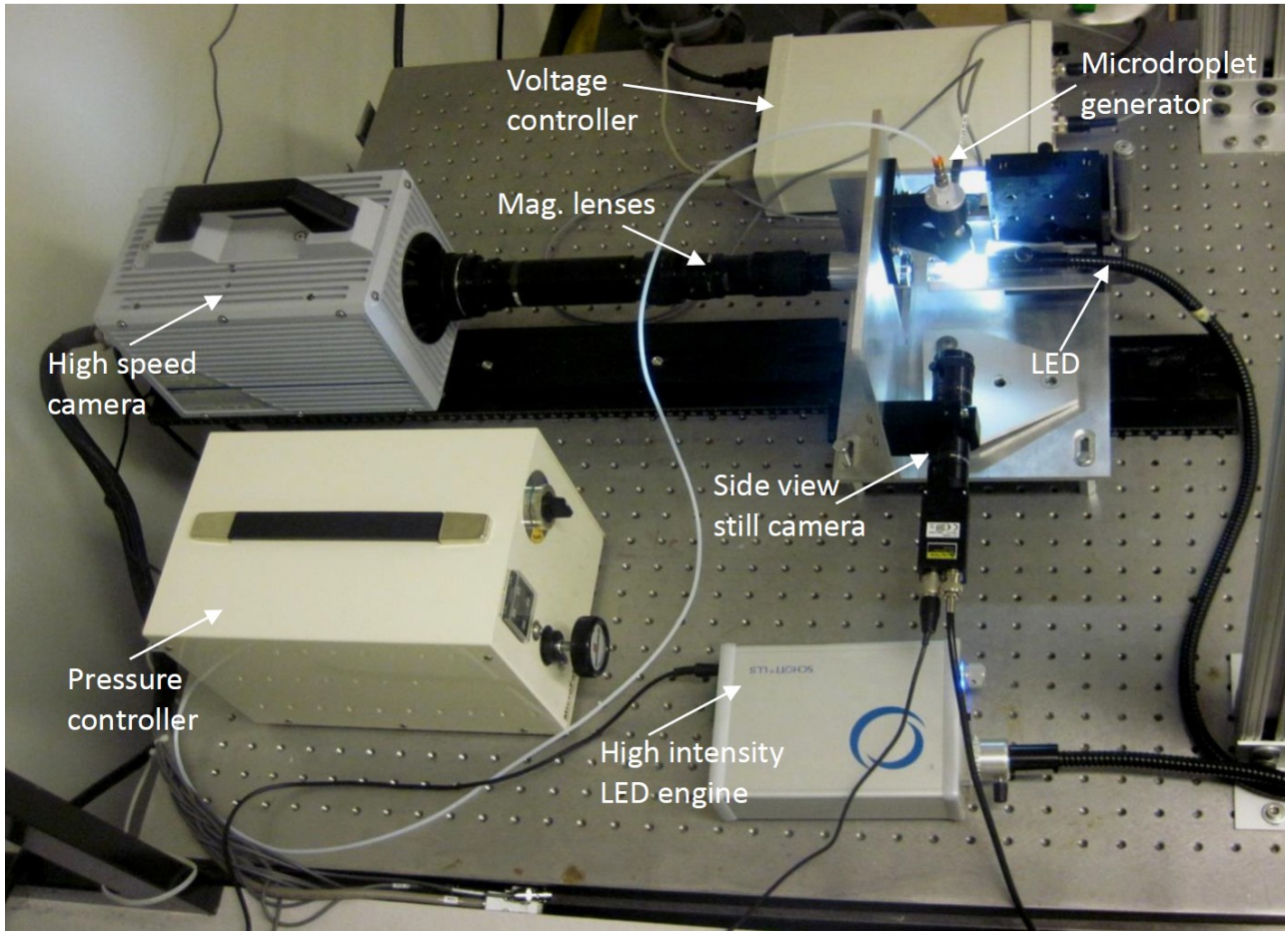

Figure 2.2 High speed imaging setup added to the micro-dispensing device

2.2 Droplet generation

In order to work experimentally with droplets, they must be produced in a controlled and repeatable way that is synchronized with the implemented camera to capture the needed pictures at the right time. As mentioned earlier, working with cloud-sized (i.e. less than 100 μm) droplets is complex. As a result, the experimental setup needed to be modified for several times before reaching the ultimate configuration. In addition, special arrangements were made according to the different parameters under test. The tested cloud-sized droplets are generated using a Micro-Dispensing system, which is the basic inkjet dispensing system (MicroFab Technologies, Inc. Plano, Texas, USA), shown schematically in Figure 2.3.

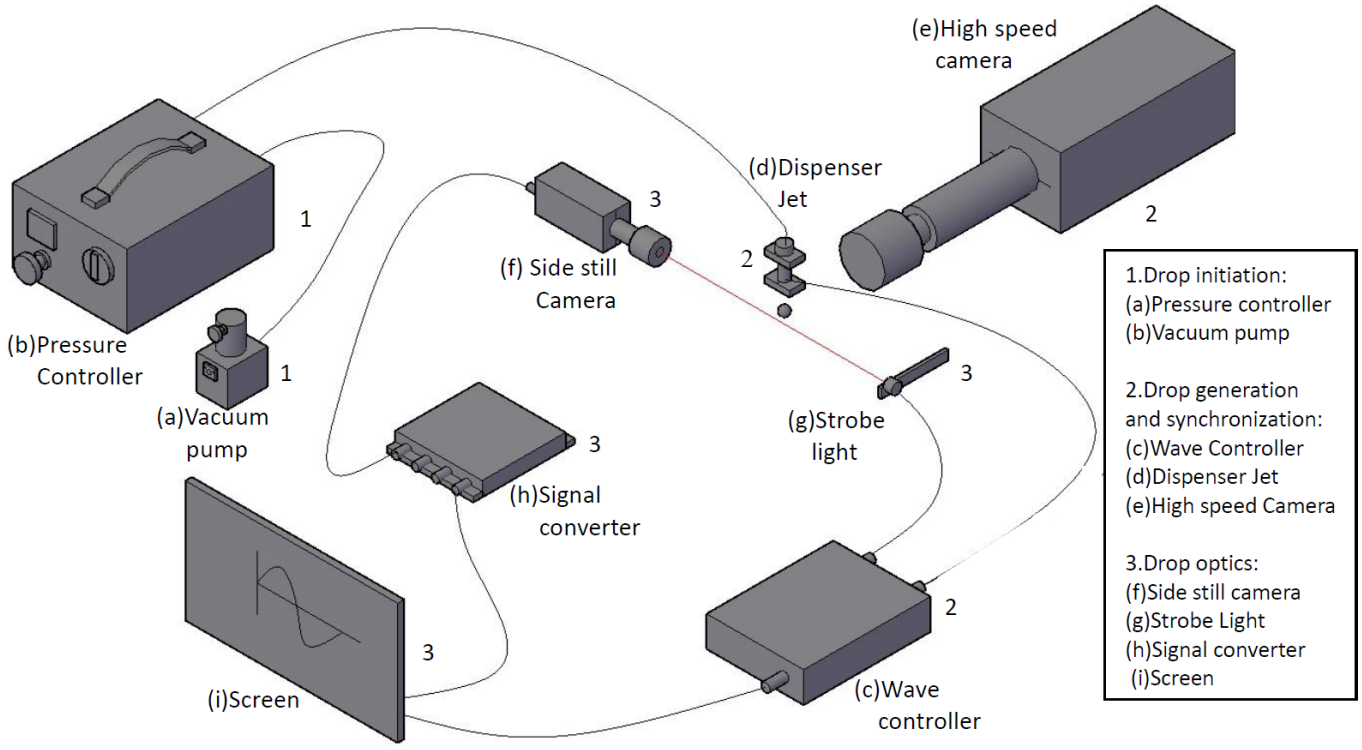

Figure 2.3 Schematic of the droplet generation and synchronization system

The device working mechanism is explained in details in the manufactures manual [117], but summarized here for the reader's convenience. It is composed of three different systems. First, drop initiation, which is composed of the vacuum pump and the pressure controller. These are linked to the dispenser to supply needed pressure difference for drop generation. The vacuum pump, item (a) in Figure 2.3, supplies the pressure difference needed to operate the controller.

The pressure controller, item (b) in Figure 2.3, includes a three state pneumatic circuit, pressure fill/purge, vacuum purge and operating pressure control. Such controller is used to control the static pressure needed for a drop on demand operation and also to damp back pressure from the dispenser jet.

Second the drop on demand generation and synchronization, which is represented as system "2" in Figure 2.3. This is composed of the wave controller, marked as (c), which is the controlling mind of the whole device that is used to provide the complex drive wave forms to the Micro-Dispensing different appliances and synchronize the high speed camera operation. The signals produced by the controller are sent to (d) the dispenser jet, (g) the strobe light, (i) the computer screen and (e) the high speed camera. The wave controller's main function is to drive the output waves to the dispenser jet and at the same time deliver the control signals to the high speed camera in order to synchronize their working times with the correct delays. The dispenser jet receiving the voltage wave operates at room temperature. It is composed of a bottom glass reservoir, which contains the fluid under test (i.e. to be dispensed) and a fitting that connect it to the dispensing device orifice. Such an orifice is changed according to the needed droplets diameters. The given wave signal to the dispenser jet determines the difference between a successful experiment (where a controlled number of accurately sized droplets are dispensed), as shown in Figure 2.4 (a) or a failure (where dripping of unknown number of droplets occur), as illustrated in Figure 2.4 (b). In addition, through the accurate control of the voltage output signals, frequencies and delay times, different droplets output diameters and velocities are produced.

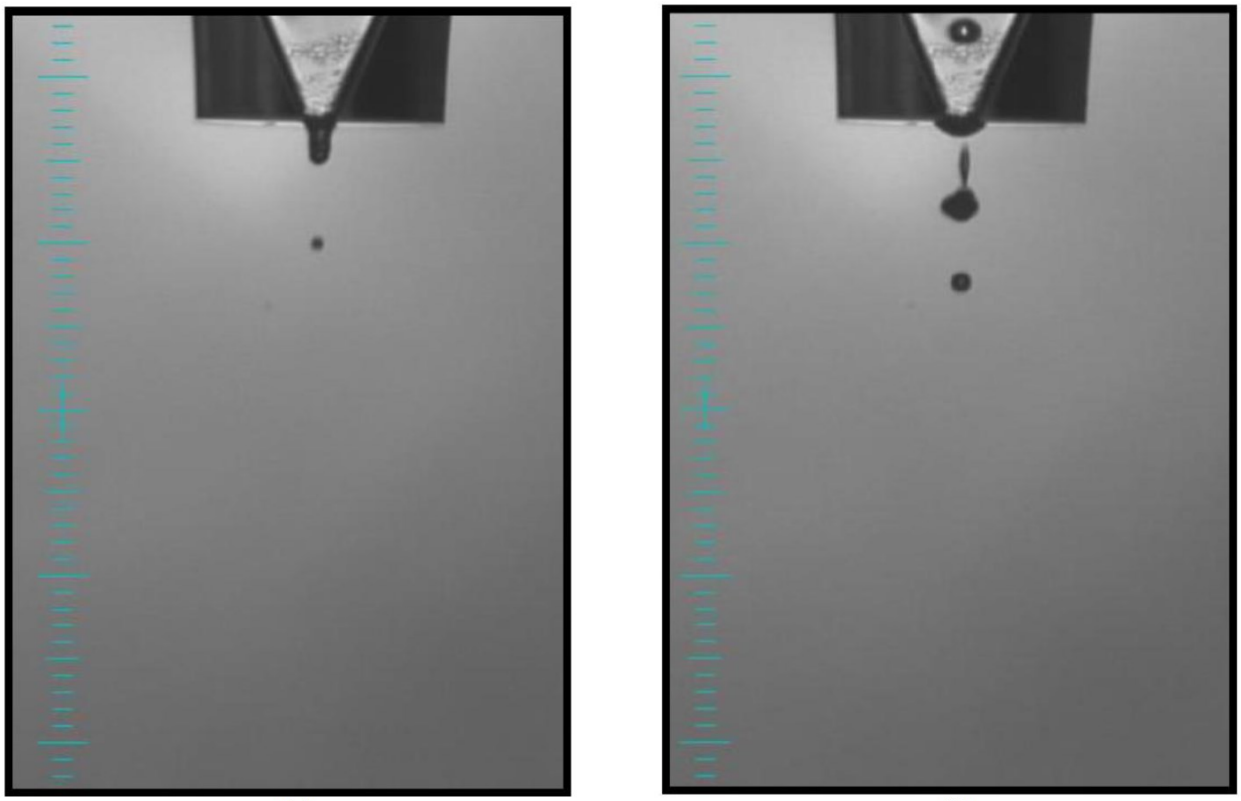

(a) (b)

Figure 2.4 Still camera footage for a 20 μm droplet showing (a) successful single droplet dispensing and (b) unsuccessful dripping

Finally, the last system inside the droplet Micro-Dispensing mechanism is the drop optics that is marked as “3” in Figure 2.3. This is divided into two main parts. First the side low resolution camera, “f”. Such a camera encloses the power supply, lens, fine focus and a mounting block. It is capable of working at a variety of distances such as 50 mm, 90 mm or 150 mm. The camera specifications include a 2.1-21 μm/pixel maximum and minimum zoom, respectively. It is used for the purpose of calibration and verification of successful dispensing as illustrated in Figure 2.4 (a). This is done using the red light beam, illustrated as “g” in Figure 2.3, which obtains its signal from the wave controller and is accurately directed to the center of the camera lens while being in line with the dispensed droplets. The second part of the optics system is the signal converter board, described as “h” in Figure 2.3, which is responsible for obtaining the images that are captured by the still camera and displays them on the computer screen "i".

2.3 Visualization and imaging

A high speed camera (SA1.1 Photron, California USA) is implemented to record droplets' images in the current study. The different camera setups and parameters implemented for the current analysis will be explained in the current section, however for any additional information please refer to the camera's manual [118]. In general, the two parameters to adjust for capturing the best images, using a high speed camera, are the frame rate (i.e. frames per second "fps") and the exposure time. First, the frame rate refers to the frequency of recording images, while the exposure time (also called the shutter speed) is the period of time during which the camera's chip records light. Recording images series and movies at high frame rates increases their display smoothness and allows the capturing of different processes in a detailed manner. This is limited by the camera data transfer rate, where at elevated speeds only sections of the camera chip images can be saved quickly enough. This is accompanied by decreasing the shutter speed, which improves the images quality by reducing blur and haziness, at the expense of brightness. Accordingly a compromise needs to be made in order to select the required frame rate and shutter speed. The experimental visualization is considered successful, if the captured images show the required event in a smooth, clear and bright manner.

For the large size microdroplets, $D_o > 200$ μm, a range of 5400-10800 fps were sufficient to render good quality images with a resolution of 1024 x 1024 and 832 x 608 pixels, respectively. On the other hand, in order to picture cloud-sized droplets ($D_o < 100$ μm) an average of 125000-500000 fps with a corresponding resolution of 256 x 128 pixels and 256 x 16 pixels, respectively were required. In addition, higher frames per second with additional magnification were utilized whenever needed. For example, in order to capture a specific dynamic scenario of a small cloud-sized droplet ($D_o < 50$ μm). The camera capturing was done automatically after synchronizing the signal given to the dispenser jet from wave controller and giving a controlled delay to image capturing trigger of the high speed camera. This allowed viewing the entire impact scenario of the microdroplets in a single camera sequence. In contrast to the majority of reviewed experimental work that required the usage of flash-photography mechanism (i.e. taking different images at different delays in order to obtain a complete sequence of events for a certain process). As a result, the microdroplet had its processes captured upon their impact on one specific location, without the need to continuously displace the substrate in order to obtain a sequence, increasing the results accuracy.

Lenses and illumination

As the microdroplets get smaller (i.e. less than 100 μm), it becomes experimentally unfeasible to capture the exact details of their impact and shedding using the magnification lenses that are used for millimetre-sized droplets. Accordingly a Navitar 12x Zoom external magnification lens (Navitar, New York USA), is used throughout the experiments [119]. All the related performance details and assembly are mentioned in the referenced manual, but are briefly summarized for the reader's convenience in Table 2.1. Furthermore, an additional magnification (Mitutoyo, Tokyo, Japan) objective lens was added to the high speed camera 12x Zoom configuration, giving a 10x to 40x times the magnification. Moreover, the needed illumination of a given lens is related to the aperture. Generally, two scales of illumination measurement exist. First the F-number (F#), (i.e. the focal ratio) which is the ratio between the focal length of the lens to its diameter of the lens [120]. Normally, a large F# lens needs more light for illumination. Second the Numerical Aperture (N.A), which is used as a standard for microscopy to relate the angle that light makes with the viewing axis [121]. Both scales are related together using equation 2.1. The depth of field, (i.e. the range of distance appearing sharp in an image) decreases as the aperture increases. Such field is related to the aperture using equation 2.2. For the current experiments, a fully open aperture was the most desirable option for the profile of the droplets in order to maximize the light that would reach the camera chip. This sacrificed the depth of field, which was not a priority in the current experiments since only the information of one plane is needed.

$$\mathrm{F\#} = \frac{1}{2N.A.} \tag{2.1}$$

$$\text{Depth of field} = \frac{0.0005}{N.A.^2} \tag{2.2}$$

Criteria	Description	Ultra 12x Zoom/ (2x-5x-10x)
Working Distance	Distance required from lens tip to viewed object in order to be in focus	37 mm, 34 mm, 33 mm
Magnification	Ratio between size of object on the camera chip to its actual size	2x -10x - 40x
Aperture	The ratio between focal length and minimum tube diameter (i.e. relates both field depth and the amount of light allowed in)	Scale vary between 2x (0.038 - 0.202 N.A.#), 5x (0.14 N.A.#), 10x (0.28 N.A.#) [122]

Table 2.1 Specifications of optical lenses performance

The different measured droplet dynamic and shedding parameters required the continuous switch between measuring lenses in order to obtain best quality images for a specified parameter. For example, for a 20 μm droplet, the measuring of different impact parameters such as maximum spreading diameter, contact diameter and contact time required a viewing window size of 256 x 16 pixels with an average frame rate of 500000 fps. On the other hand, for parameters such as the restitution coefficient and shedding velocities, wider viewing windows are needed. In such a case, a compromise of lower frames rate of approximately 30000-75000 fps are chosen with corresponding resolutions of 512 x 352 and 512 x 128 pixels, respectively. Therefore switching between 2x, 5x and 10x magnification lenses was required to accurately measure different parameters, see Figure 2.5.

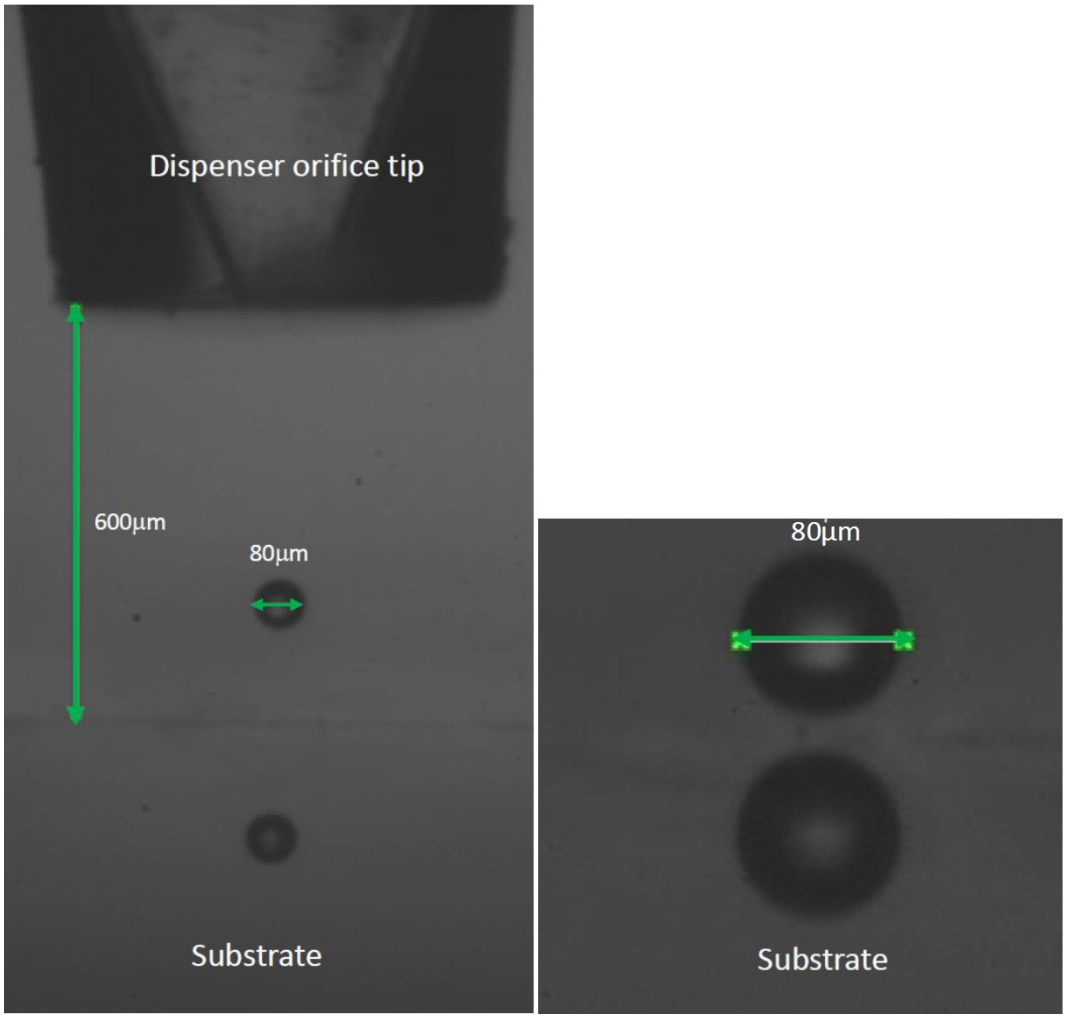

Figure 2.5 Impact of an 80 µm droplet showing (a) a view of the whole domain and (b) a zoom on the droplet directly before impact

2.4 Image processing

The obtained images must be quantified into different values and parameters that can help in identifying the droplets behavior. For such a reason the high speed camera raw images are imported into MATLAB for image processing. This helps to automate the measuring of the hundreds of thousands of images recorded by the high speed camera. This was seen to be the best way to accurately put the data in an organized fashion for interpretation by finding quantitative values of different parameters such as droplet size, impinging velocity, contact angle, spreading diameter, contact diameter and maximum height. This is repeated for 30 successive experiments for each droplet size and the obtained results are then averaged for increased accuracy. The edges' profiles of the impacting droplets are identified by implementing the MATLAB edge detection

tool [123]. The detected air-water interface is obtained by tracing the real images after being converted into binary. The functions implemented include brightness adjustment, conversion to binary and boundary tracking. An example of the obtained results is illustrated in Figure 2.6. The developed script also includes the removal of the background image, which was done by comparing the actual image to a background image recorded after the removal of the merged droplets. Based on the comparison, a new image which ideally only shows the droplet is created. The light intensity of each individual pixel of the recorded image is compared to the intensity of the background image. If the light intensities are sufficiently close to each other, that pixel is assumed to be part of the background and the corresponding pixel in the new image is assigned a numerical value equivalent to white (typically 256). If not, then the new image is assigned the pixel value of the recorded image. The newly created image is then converted to a binary image and the boundaries traced and stored as arrays. These arrays are then used to measure the size of the geometry of the droplet(s). In order to determine the actual size of the droplets, sizing a pixel (i.e. calibration) is required. The image is calibrated by recording the size of the dispenser jet orifices.

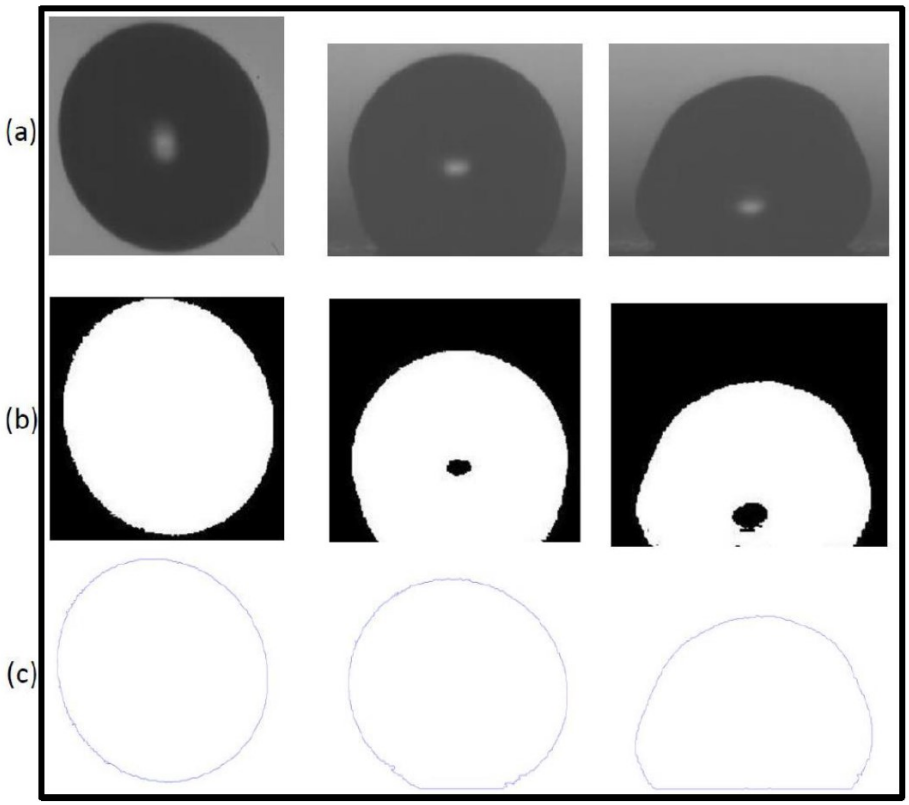

Figure 2.6 Example of the impingement of the 200 μm droplet (a) raw images, (b) binary images and (c) edge traced images, at two stages, before and during impact

Results verification of different parameters was made by implementing different methods to obtain each parameter and then values are compared together. For example, droplets velocities before and after impact are calculated using two different methods. The main idea behind both techniques is to track a certain chosen reference point on the droplet, after which analysis for several frames is used in order to calculate the required velocities. The first method is applied by following the center point of the droplet in its picture 2-D side view. On the other hand, the second is conducted by following the average of the droplet top and bottom velocities. The two methods are calculated by using the Photron FASTCAM viewer (PFV) and the Logger Pro software [124]. A maximum difference of ± 0.05 m/s in velocity calculations was found by comparing the obtained values, for both methods, from the two software. Furthermore, the DropSnake 2.1 software [125, 126] was implemented to confirm the results obtained from MATLAB for the different kinds of droplet contact angles. The quantified parameters for the current study include the initial diameter (D_o), the contact diameter (D), the maximum spreading diameter (D_{max}), and droplet height upon impact *(h)*. Where, D_{max} is measured at the instance where the droplet's deformation on a surface is maximum, (i.e. just before it starts to retract) and *h* is measured from the substrate's surface until the top edge of the droplet, see Figure 2.7.

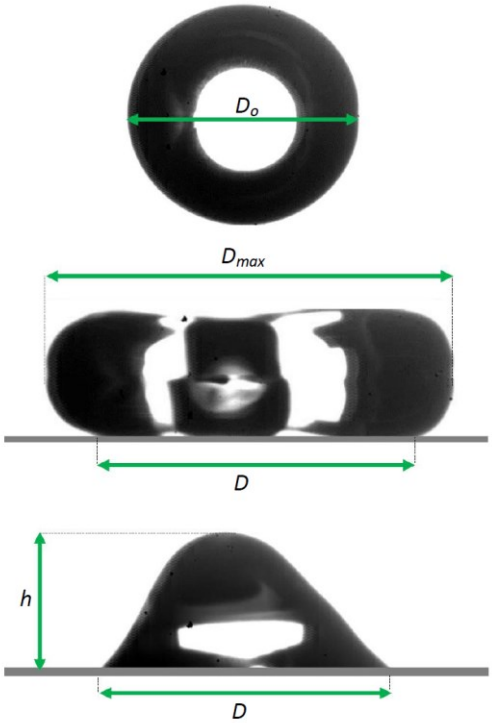

Figure 2.7 Parameters chosen for the experimental analysis

The obtained parameters are used to calculate different dimensionless numbers and terms used throughout the current analysis. These terms are summarized in Table 2.2. The two fundamental dimensionless numbers used are the Reynolds ($Re=\rho V_1 D_o/\mu$) and the Weber ($We=\rho V_1^2 D_o/\gamma$) numbers, which measure the droplet inertia to viscosity and inertia to surface tension, respectively. The experiments are performed using distilled water, where the density ρ=998 kg/m^3, the dynamic viscosity μ = 10^{-3} Pa.s, and the surface tension γ = 728 x 10^{-3} N/m^2. In addition to the maximum spreading coefficient that is calculated as the ratio between the maximum diameter attained by the droplet upon impact and the droplet initial diameter. Such a coefficient is used to illustrate the ability of droplets to spread over the different substrates. Moreover, the roughness effect on the droplets is analyzed by using the relative roughness which relates the average surface roughness of the substrate to the droplet initial diameter. Finally, the ratio between the droplet's recoiling velocity (V_2) to its impact velocity (V_1) is obtained in order to quantify the restitution coefficient ε that was explained earlier in Chapter 1, section 1.3.

Dimensionless term	Equation
Reynolds Number	$Re = \frac{\rho V_1 D_o}{\mu}$
Weber Number	$We = \frac{\rho V_1^2 D_o}{\gamma}$
Max. Spreading Coefficient	$\frac{D_{max}}{D_o}$
Relative roughness	$\frac{R_a}{D_o}$
Restitution Coefficient	$\varepsilon = \frac{V_2}{V_1}$

Table 2.2 Dimensionless numbers and coefficients

2.5 Surface coating substrates

Various substrates are prepared with different surface properties giving a range of wettabilitties that cover both hydrophilic and superhydrophobic surfaces. For additional laser micrograph images of the prepared substrates please refer to Appendix A. The hydrophilic smooth aluminum and superhydrophobic rough WX2100 substrates are used to demonstrate the distinct behavior of the different droplets sizes' upon impact and shedding. The aluminum surface used is 5052 type with a #8 mirror finish. Laser micrograph of the polished aluminum shows an average surface roughness of $R_a = 0.06 \pm 0.01$ μm, see Figure 2.8.

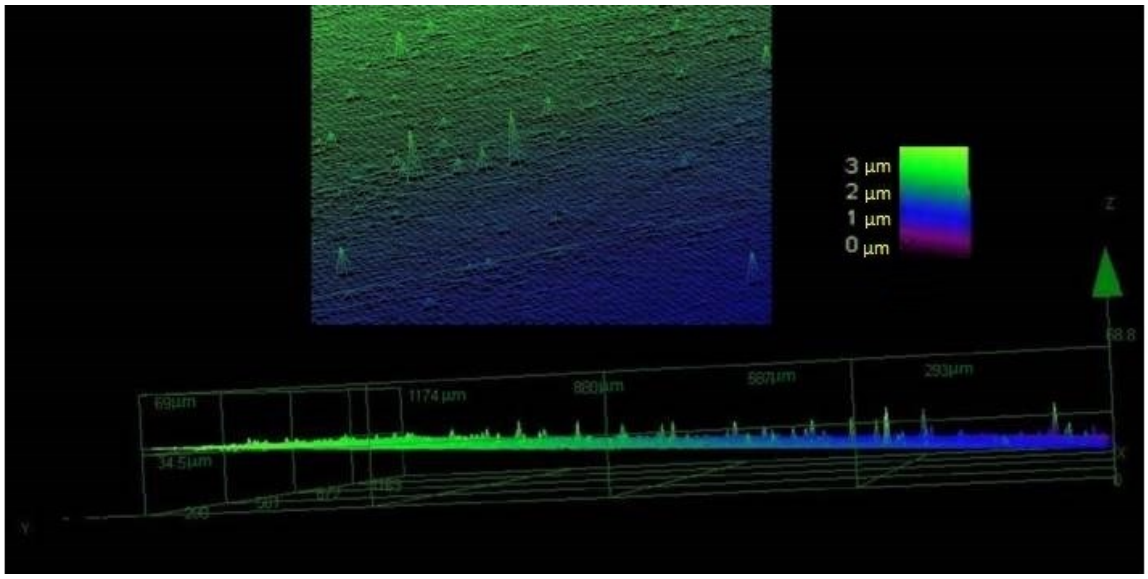

Figure 2.8 Laser micrograph image of the hydrophilic surface

The superhydrophobic surface was prepared using commercially available WX2100 spray coating (Cytonix Inc. Maryland, USA), yielding a rough surface. Every time the spray was applied over a polished aluminum sample and left for 24 hours to dry before performing any experiments. The coating working mechanism takes place by inducing a micro-scale roughness on the substrate upon spraying and drying. This results in a superhydrophobic surface with a static contact angle of $\theta_S \geq 160 \pm 3°$ and a contact angle hysteresis $\Delta\theta = 8°$. Qualitatively, Figure 2.9 shows that the droplet should behave in a Cassie state, since the ratio between spacing to feature size is much less than one [127-129]. However, this is valid for millimeter-sized droplets.

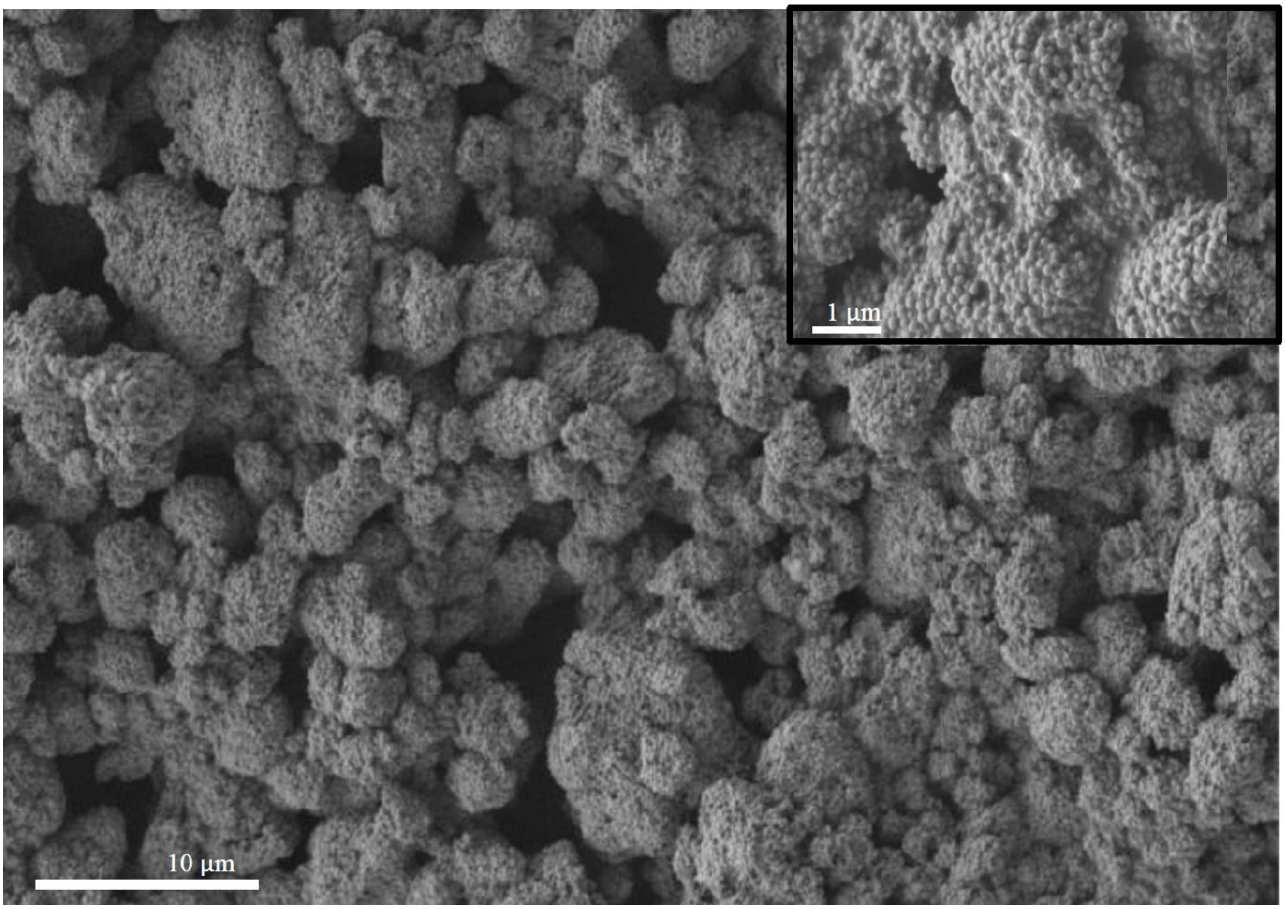

Figure 2.9 SEM of the superhydrophobic surface [129]

The substrates' topologies are of vital importance for this study since the cloud-sized droplets are in the same order of magnitude as the substrates' surface roughness, especially in the case of the SHS. Accordingly, such surface roughness plays a major role in changing the obtained results for the different microdroplets. In order to further characterize the utilized surfaces' morphology, laser micrograph scans were made for each substrate. The confocal laser micrography of the designed SHS illustrate a average surface roughness R_a =1.6 ± 0.2 µm, see Figure 2.10.

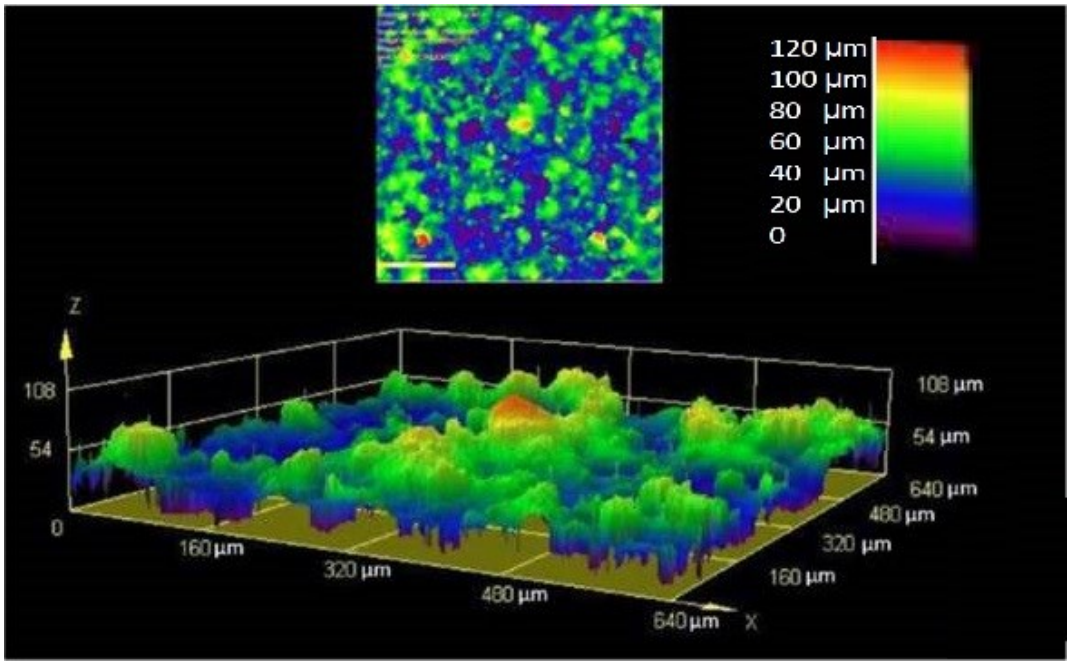

Figure 2.10 Laser micrograph image of the superhydrophobic surface

As mentioned in Chapter 1, the substrates properties are obtained by finding the droplet's static, receding and advancing contact angles. This is done after quantifying the droplets images imported from the high speed camera into the different image processing algorithms, i.e. MATLAB image processing tool box and DropSnake 2.1 software [125, 126]. An example of the static contact angle obtained using MATLAB is illustrated in Figure 2.11.

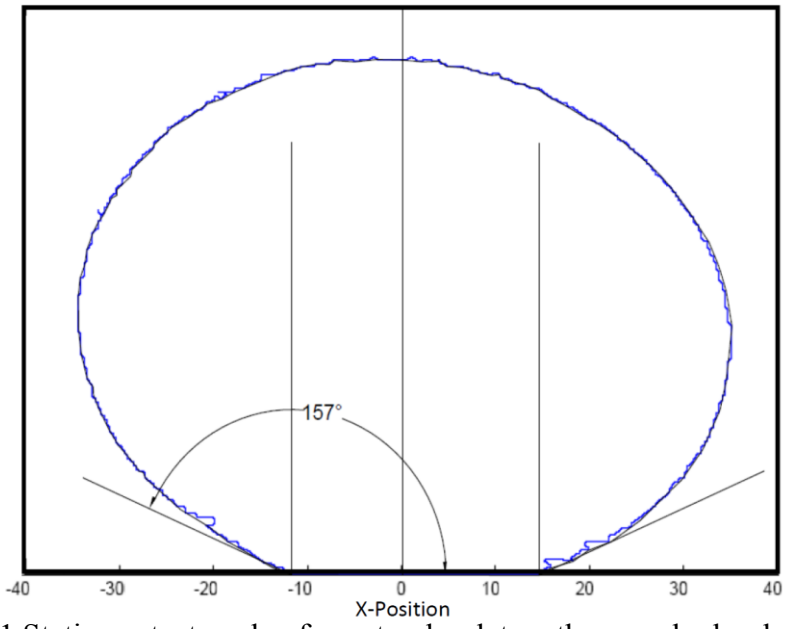

Figure 2.11 Static contact angle of a water droplet on the superhydrophobic surface

The volume changing method is implemented to find the advancing and receding contact angles, (i.e. CAH). An example for a 20 μm droplet advancing and receding angles are shown in Figure 2.12 (a) and (b), respectively.

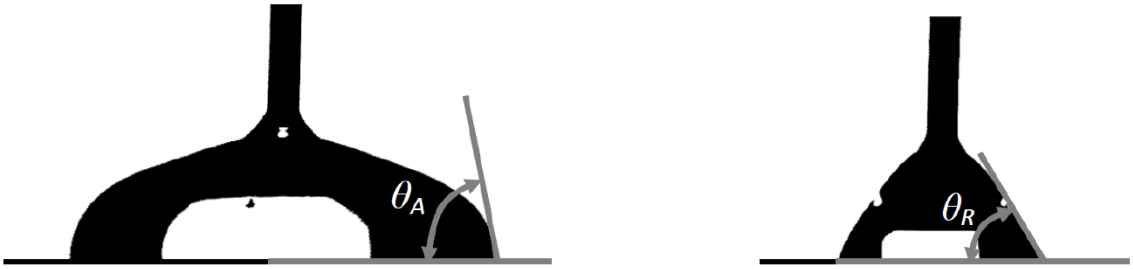

Figure 2.12 Real images of a 20 μm droplet (a) advancing and (b) receding contact angles

The used substrates characteristics, (i.e. wettabilitties) are summarized in Table 2.3 that shows static, advancing and receding contact angles.

Material	Average roughness (R_a)	Static	Advancing	Receding	CAH
Aluminum	0.06 ± 0.01 μm	75° ± 3°	92° ± 3°	52° ± 3°	40° ± 3°
WX2100	1.6 ± 0.2 μm	160° ± 3°	165° ± 3°	157° ± 3°	8° ± 3°

Table 2.3 Properties of utilized substrates for impact and shedding experiments

2.6 Microdroplets experimental setup

The previously described aspects of droplet dispensing, visualization and image processing, and the different prepared substrates are all implemented to study microdroplets impact dynamics and shedding incipient velocities.

Impact setup

The novelty of the designed impact experiments is the ability to obtain the entire impact scenario of a cloud-sized droplet using a single droplet and the same location of impact on the tested substrate. However, this was difficult to achieve without proper design adjustments and special settings. This is due to the fact that the small size of the tested droplets made the designed experimental test rig sensitive to external environmental conditions such as vibration, air drifts,

humidity and temperature changes. Experimentally it gets harder to direct such microdroplets towards a specific impact point. An example of the original deviation made by the microdroplets from its vertically dispensing path through time is illustrated in the snap shots shown in Figure 2.13 (a) through (d) for the dispensing of an 80 μm droplets jet for a time period of 75 s.

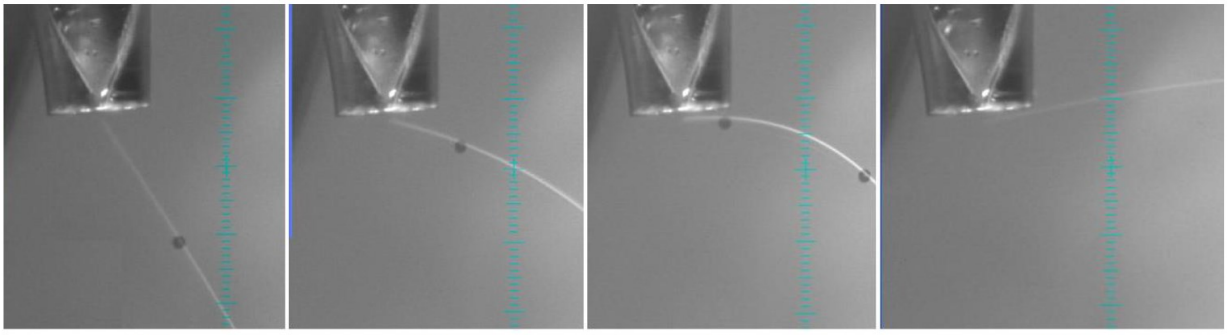

(a) (b) (c) (d)

Figure 2.13 Snap shots of an 80 μm jet after dispensing with (a) 1 s, (b) 35 s, (c) 50 s and (d) 75 s

These deviations resulted mainly from the external sources of vibration and air drifts. First, to overcome the vibration problem the whole system was mounted on a Newport vibration damping table (Newport Corporation, California, USA). Furthermore, a dedicated mount, with rails to provide horizontal translation, is designed to concretely fix the whole system to the table. The vibration levels were then damped enough to be considered negligible with no vertical or horizontal movements. Second, a completely sealed compartment was designed, manufactured from plexiglass sheets and used to contain and isolate the dispensed droplets in order to overcome air drifts. Moreover, the dispensing distance was kept below 20 mm through using a microcontroller that adjusted the dispenser-substrate distance. This was vital since the droplets were seen to drift at larger distances. Accordingly, the microdroplets are not expected to gain any velocity or inertial effects due to the dispensing distance. The dispenser-surface distance, upon droplet dispensing is obtained using the 2x magnification lens. Afterwards a higher magnification is implemented (up to 40x) in order to get the exact impacting behavior of the tested droplet.

In addition, the humidity and temperature of the surrounding air was controlled to prevent the droplets from evaporating as soon as they are dispensed. For example at 40 % humidity and room temperature (20 - 22 °C) an 80 μm droplet stayed around 2.5 s on the substrate surface before it started to evaporate. The chosen humidity and temperature sensor, Sensirion SHT11,

could measure online data with ± 3 % relative humidity and ± 0.5 °C values. This sensor was connected to a CPU cooling unit through a small BeagleBone processor in order to fix the testing surrounding temperature to the desired value. Moreover, a sponge was put inside the compartment and wetted according to the need to increase the humidity. This was important for compartment saturation only while fixing the focus and zooming at the primary testing stages. After which the humidity and surrounding temperatures could then be dropped down to any desired values. Since the actual time for the entire impact experiments is in the order of micro-seconds. Furthermore, a Peltier Plate was used to keep the substrate temperature at room temperature during the entire impact experiments. This is because the aim was to identify the parameters affecting the droplets impact behavior with no interference of substrate temperature. A detailed description of the Peltier Plate implementation and control are given in the solidification setup.

Shedding setup

In order to test the shedding of microdroplets on different substrates, additional parts are added to the previous mechanism that was used for impact tests. To begin with a slit nozzle was designed and implemented in the chamber that has the dispenser head and substrate. The nozzle is designed to have a slit output in order to cover the whole substrate width. Appendix B illustrates the detailed nozzle design. The image illustrated for the nozzle in Figure 2.15 shows how the surface is being horizontally flushed with the slit nozzle outlet. This is done by using a spring regulated pivot that pushes the flat substrate to the side of the support and continuously holds it in place. As a result, any turbulence occurring from the high speed air hitting the front side of the flat plate and causing circulations around the droplets is avoided. The figure also shows the air hose which carries high pressurized air into the nozzle through a pneumatic control valve. In addition, the used (2x, 5x or 10x) objective lens is put on the opposite side of the high intensity LED tip, leaving the dispenser jet and the generated droplet exactly in the middle.

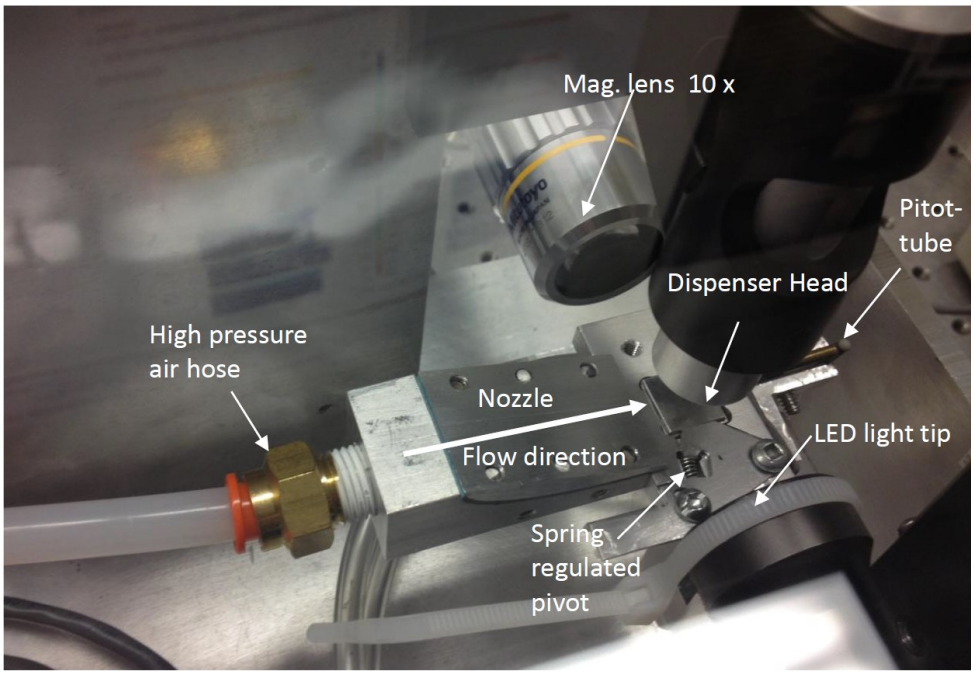

Figure 2.14 Image of enclosed chamber showing slit nozzle

In principle, the dispenser and nozzle are synchronized with a specified time delay in order to give the microdroplet few milliseconds to dispense and settle on the substrate before being shed. A BeagleBone is used to synchronize their performance. The chosen BeagleBone had the configuration of 512 MB RAM, 1 GHz processor clock, and 2 GB of embedded non-volatile memory system (eMMC) flash memory.

Furthermore, a stationary pitot-tube, illustrated in Figure 2.14, is placed on the opposite side of the nozzle, in order to measure the shearing air free stream velocity. Conceptually, the pitot-tube diameter must be much smaller in size in comparison to the anticipated boundary layer thickness. However, this should be done with care, because when the pitot-tube size is reduced, its pressure variation response rate is also reduced. This makes it difficult for the pitot-tube to obtain a true reading. In addition, although the chosen pitot-tube carry the smallest tip found (i.e. 2000 μm), it is still considered relatively large in comparison to the microdroplets sizes' and the corresponding small (thin) attained boundary layers (i.e. approximately 400 - 600 μm) for different flow velocities over the flat substrate.

As a result, an air flow meter is implemented with the high pressure valves system used to measure the mass flow rate at the nozzle output for each shedding experiment. Then the average velocity at the outlet of the nozzle is calculated using the continuity equation. The obtained flow

meter results are continuously compared to the pitot tubes output values to increase the accuracy and verify the obtained results. The maximum difference between the obtained values from both devices was 8 %. The pitot-tube results are then used as a reference to verify the validity of the output results of each experiment. After which, the equivalent velocity on the droplet, u, inside the boundary layer close to the surface of the substrate, is obtained. This is done as a collaborative work with Concordia CFD research team by using numerical simulation conducted using the OpenFOAM 2.1.1 software; see Appendix C for the boundary layer numerical simulation details.

In addition, if the compartment is kept completely sealed during the shedding experiments, then pressure build up occurs inside as the high pressure shearing air is allowed in through the nozzle. Even if this air is allowed to run for a short period of time just to shear the droplet, then back pressure from the shedding air will disturb the experiment and affect its results. Accordingly a back door that is installed at the complete opposite side of the nozzle is implemented and synchronized to open exactly 2 ms before the air shedding starts, (i.e. 2 ms before throttle valve opens to allow air in the nozzle). The delay time of the door can be changed as per the required operation. For example, for substrate cleaning purposes, shedding of air can last for almost 2 ± 0.5 minutes while the door remains completely open. The door functionality is synchronized with the shedding experiments, as shown in Figure 2.15, through a dedicated motor that attains its signals through the BeagleBone processor.

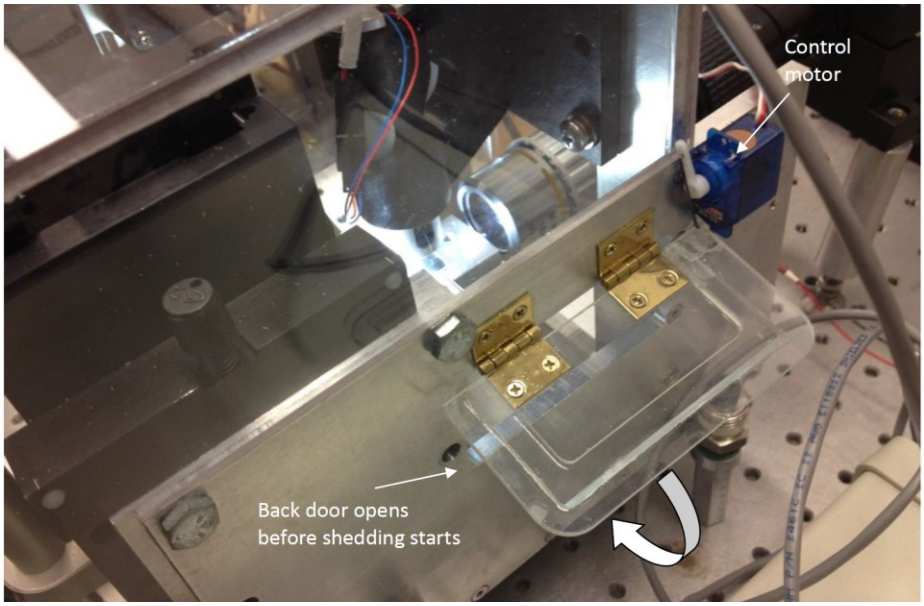

Figure 2.15 Backdoor opened just before shedding using a control-motor

The complete shedding test rig is illustrated in Figure 2.16, where all the previously mentioned devices are mounted together. The general experiments were performed at room temperature, 20 - 22 ± 0.5 °C and 15 - 25 ± 3 % humidity, which was controlled using humidity and temperature sensors located inside the compartment. These sensors, the back door control motor and the pneumatic valves obtained their power from the chosen CPU power supply and were controlled using the BeagleBone, see Figure 2.16.

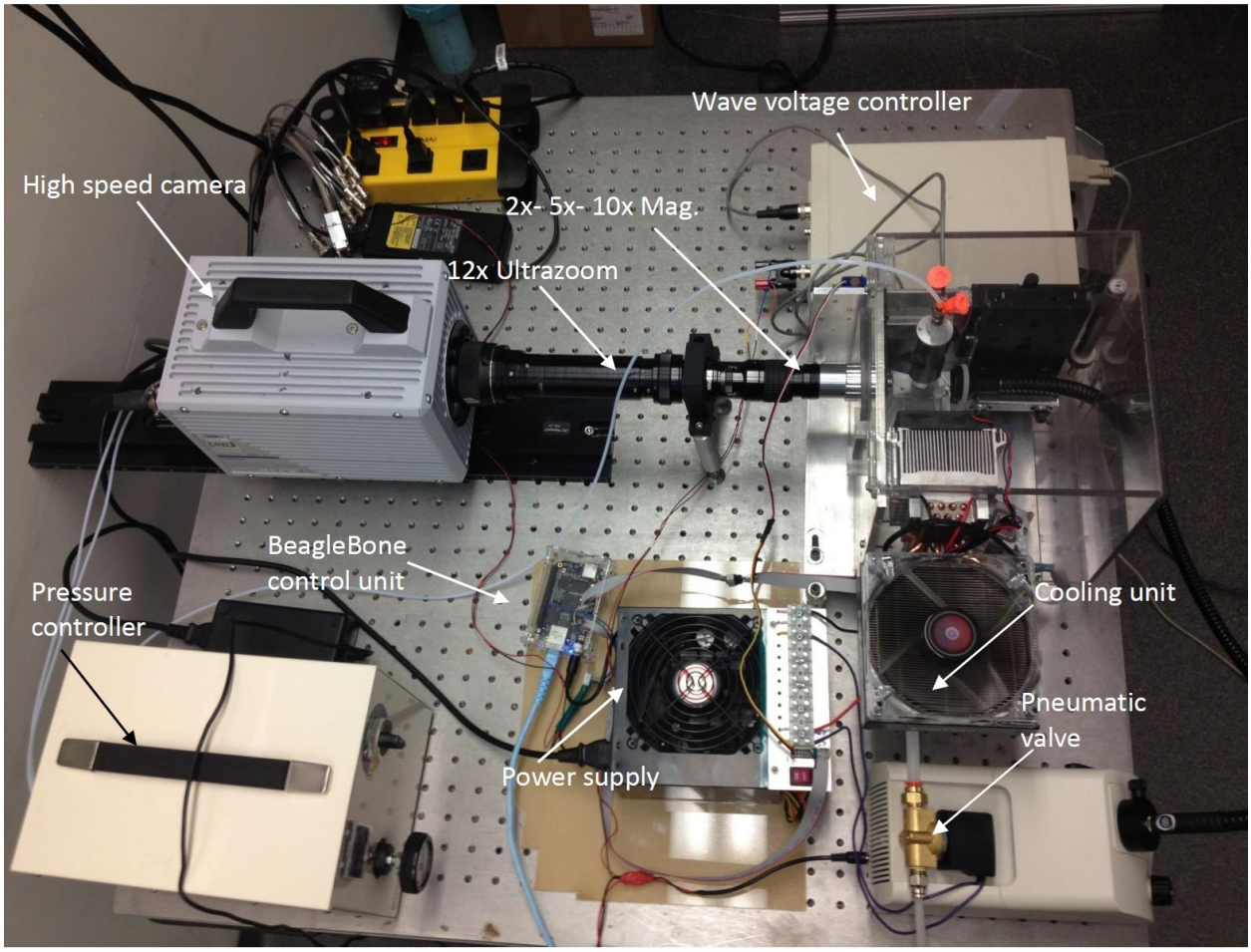

Figure 2.16 A top view of the complete system used for droplets shedding

The shedding routine occurs in several steps that are automated and synchronized in order to achieve a successful experiment. Primarily, the droplet is dispensed in continuous mode starting with a high frequency of 150 down to 1 HZ. This is done in order to achieve the best focus and zooming while the high intensity LED light is switched on. After the droplet is guaranteed to be in correct field of vision, the LED light is switched off and the cooler, if needed,

is started in order to bring down the temperature. The humidity and temperature sensors give continuous measurements of the air parameters. When the surrounding air temperature and humidity are within the required range (i.e. room temperature between 20 - 22 °C and humidity is for example between 15 - 25 %), the experiment routine begins. This routine starts first by the LED light being switched on; the camera starts to capture two seconds after LED is switched on and continues for 1.5 s. A single droplet is generated to impact the tested substrate. The back door starts to open 2 ms prior to valve opening and shedding air nozzle starting. The shedding air stays on for approximately 7 - 8 s to completely shear off the dispensed microdroplet and completely clean the tested surfaces. This cleaning can continue for 2 ± 0.5 minutes, if needed. Door is then closed and step 1 (i.e. focusing and zooming) is repeated all over again. The operating steps are all summarized in the flow chart shown in Figure 2.17.

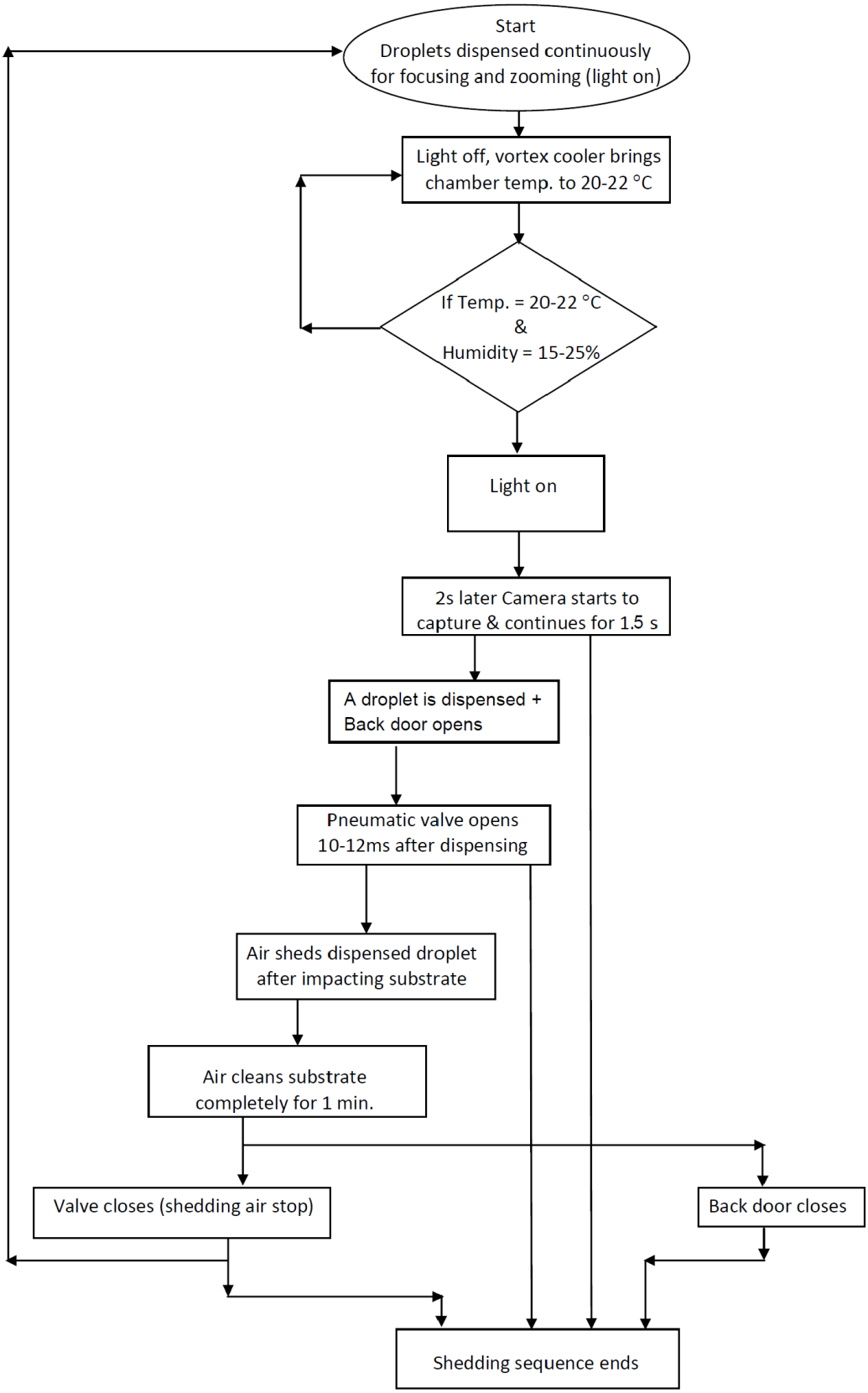

Figure 2.17 Flow chart of processes used in the microdroplets shedding tests

As previously mentioned, the shedding experiments are conducted to obtain the incipient of motion velocities for the different droplet sizes, where the delay between the dispensing of the droplet and its shedding is considered the main parameter to fix. The experiment is termed successful if the droplet settles on the substrate, then air flow starts shedding it before it evaporates; see Figure 2.18 (a). If the delay time is too long, then the droplet evaporates before being shed. On the other hand if air flow starts from the nozzle too early i.e. before the droplet manages to reach the substrate then it will be blown away aimlessly, as shown in the snap shots in Figure 2.18 (b).

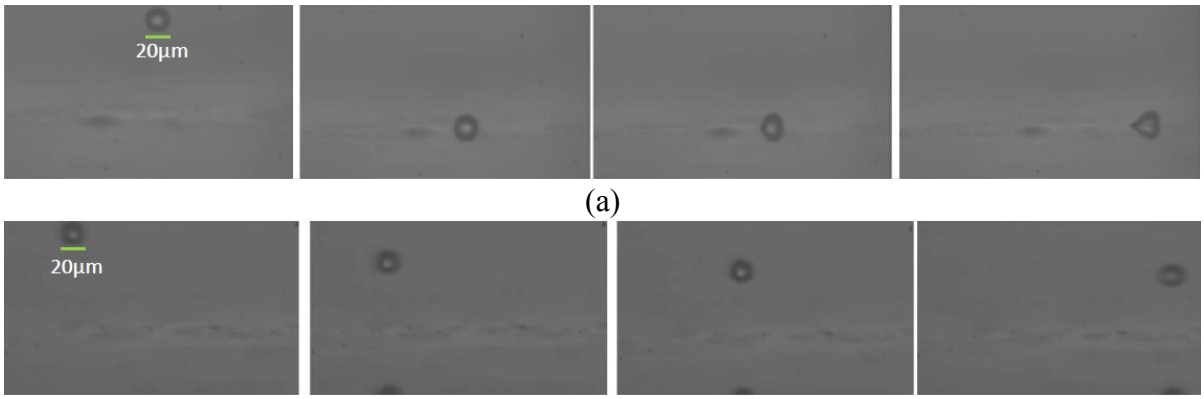

(a)

(b)

Figure 2.18 Shedding of a 20 µm droplet with a delay of (a) 11 ms and (b) 9 ms

As a result the above described shedding routine must be accurately synchronized and timed, where for each droplet size and dispensing velocity, a specific dispensing-shedding delay time must be fixed. Accordingly the entire shedding operation is automated by the BeagleBone with a C++ program. The experiment starts at a specified air temperature and humidity, then at these values a message is given to the user to dispense the microdroplet, and as the dispensing process occurs all the starting times of the remaining procedures, (i.e. light, backdoor opening, air shedding, etc.), are determined accordingly. The delay times and operating process are summarized for time overlapping in Figure 2.19.

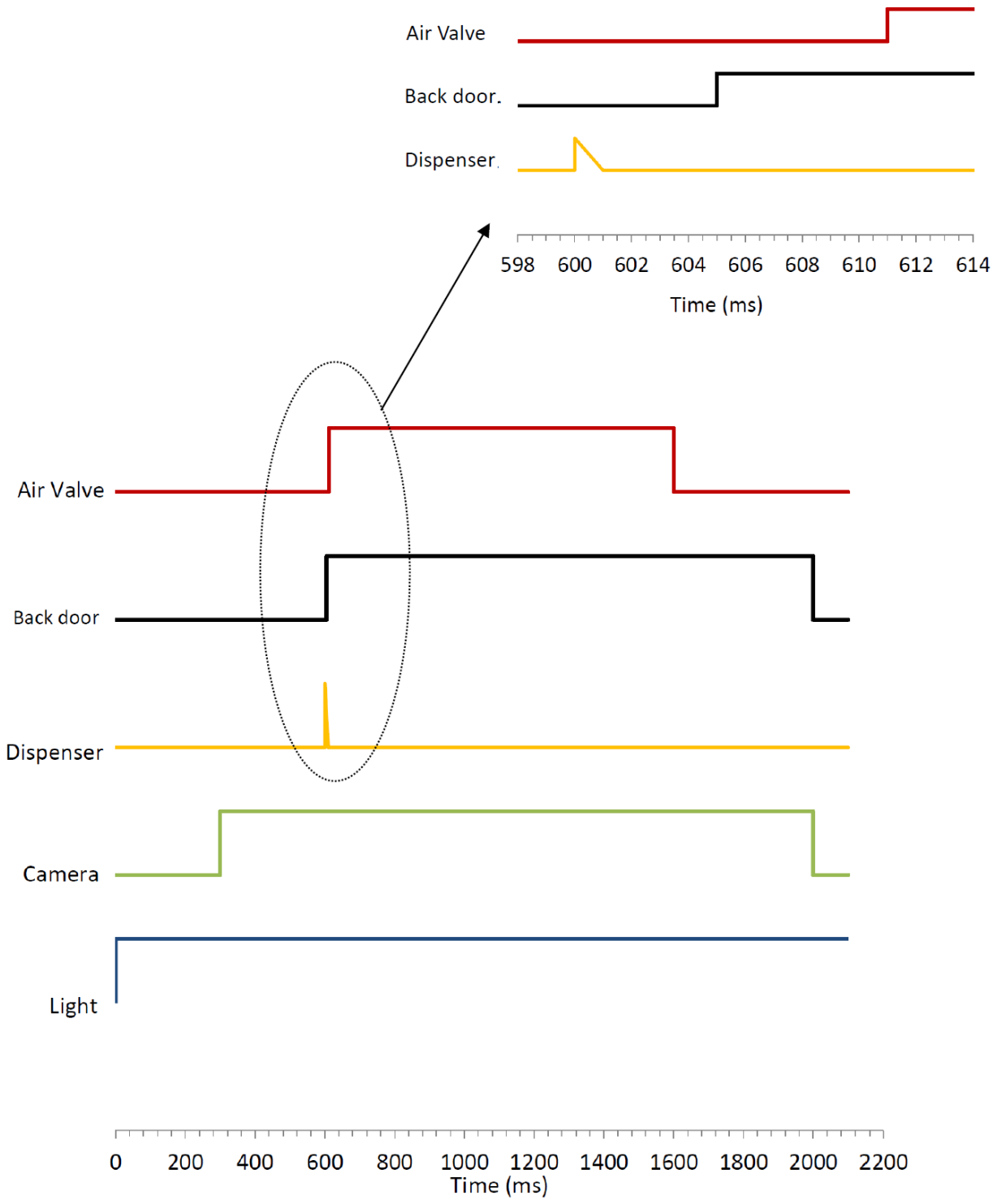

Figure 2.19 Air shedding time diagram used to synchronize all different peripherals

Solidification setup

The previously explained design is further extended in order to test microdroplets solidification. An auxiliary Peltier Plate is added to control the substrate temperature. The choice of the Peltier Plate was made due to its quick response, which compensates for its low thermal efficiency. The used peltier is added under the tested substrate from its upper top side that is smeared with a heat exchanging film and fixed to the bottom side of the tested substrate. At the bottom side of the peltier, two tubes (in and out) are fixed for cooling it down. Rainx fluid that can go down to – 45 °C is used for cooling by circulation. The fluid is primarily cooled down to – 18 °C and then allowed to circulate using a water pump. The temperature of the cupper part is seen to drop down to – 35 °C after 12-14 minutes of circulation. The heat transfer enhancer film placed in between the cupper plate and the tested substrate allows for the rapid and efficient transfer of such coldness to the surface of the substrate. As a result the substrate temperature drops down to a minimum of – 25 ± 2 °C.

In addition, the temperature of the substrate is continuously controlled. This is achieved by continuously measuring its value using an MLX90614 contactless infrared sensor (Melexis NV, Sint Krispijnstraat, Belgium), which is put directly above the substrate. In addition, an active control loop is created for the Peltier Plate operation using the BeagleBone, with the substrate temperature as the input value. This automated the temperature control of the substrate and kept it within desired values. The value of the substrate temperature is then used as an additional control measure to allow for droplet dispensing to occur only when the substrate desired temperature is reached (in addition to previous control factors of the surrounding air temperature and humidity). Furthermore, the whole chamber temperature was controlled to be less than – 20 °C, in order to allow for the dispensed droplets not to be affected by a higher surrounding temperature and also to imitate a solidification environment in cold flying conditions. This is accomplished by replacing the CPU cooler unit with a vortex cooler, see Figure 2.20, that is designed to produce air flow output at – 25 °C at its tip after high pressurized air (at 100 psi) is allowed to flow for 30 minutes through an additional pneumatic valve. The vortex design is illustrated in Appendix D. Finally, the compartment is completely isolated using heat sealant foam. Figure 2.20, demonstrates the entire final design that is implemented for droplets impact and shedding at different substrates' temperatures. It also enabled the solidification of dispensed microdroplets.

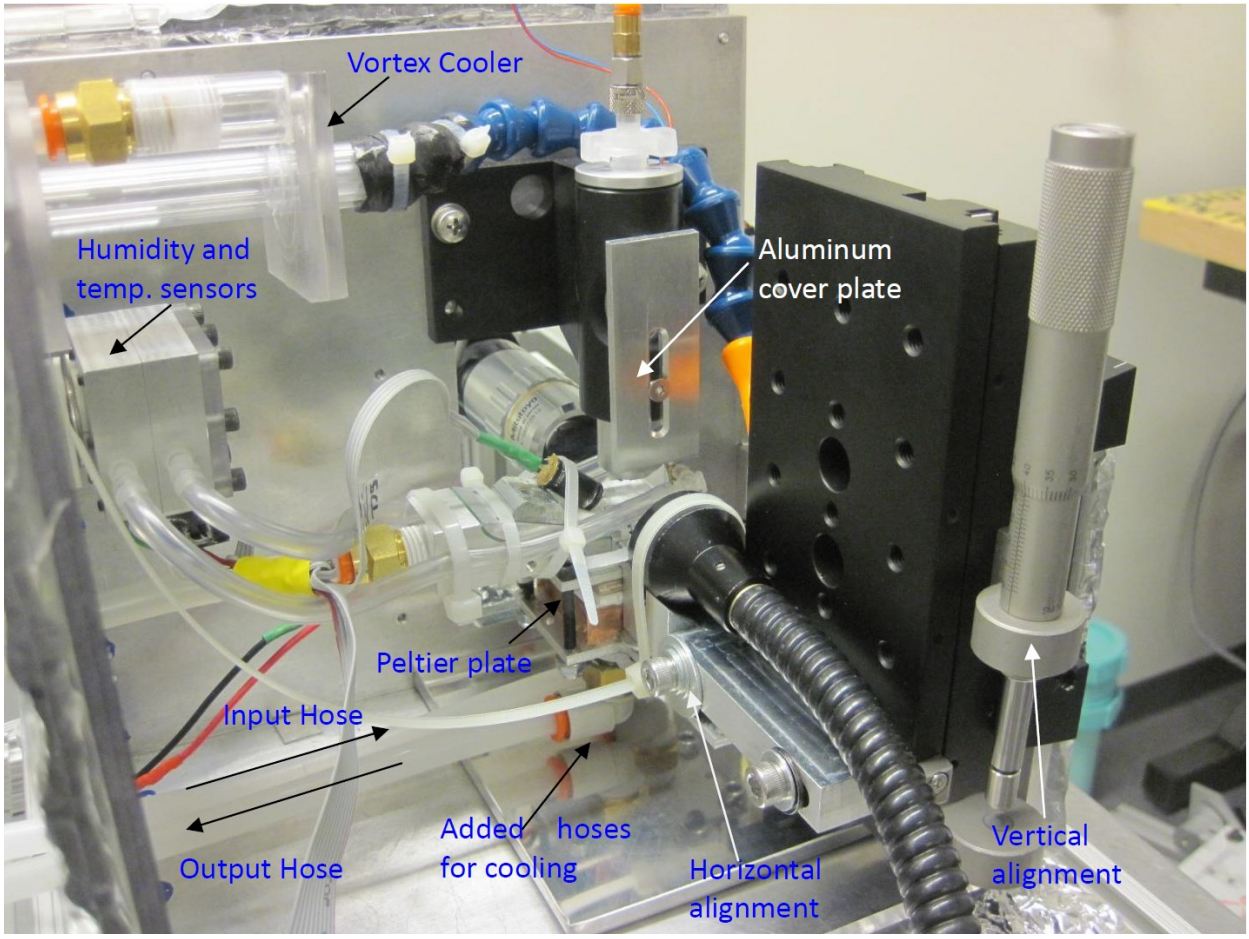

Figure 2.20 Added auxiliaries for impact, shedding and solidification of droplets

2.7 Error approximation

The measured experimental quantities are based on time and distances. The temporal error is based on the frame rate that is described as the number of frames/second. Therefore the temporal error can roughly be equal to (1/no. of frames). For example for a 5400 frames, then the temporal resolution is equal to (1/5400) = 0.2 ms. Additional effects that are related to faulty timing of the camera internal circuitry are assumed to be negligible. Furthermore, the size of pixel is calibrated using the dispensers tip. In order to measure the droplet diameter, the average of the height and width is taken in each of the 10 frames prior to impact, and then those ten values are in turn averaged. This tactic was used to minimize measurement error associated with droplet oscillations, especially for large droplets $D_o \geq 200$ μm since smaller droplets are less prone to oscillations.

In general, the humidity and temperature are controlled since they can have a substantial influence when environmental conditions deviate significantly from standard room temperature conditions. This is seen in the works of Yin *et al.* [130] and Mockenhaupt *et al.* [131]. However, these works show that in the current range of chosen relative humidity and at room temperature, the wettability of superhydrophobic surfaces does not show a substantial change.

Substrates inhomogeneity

In general the inhomogeneity of the substrates can be a source of error. This is only true if the results obtained for the different impact and shedding parameters are drastically altered upon changing the droplets location on the substrate. Thirty experiments were done on each substrate where droplets are deposited on ten different locations. The SHS is cleaned before each experiment using air flow from the nozzle. After 30 experiments the SHS is replaced due to droplets pinning, which affects the obtained results especially for the restitution coefficient, see Figure 2.21.

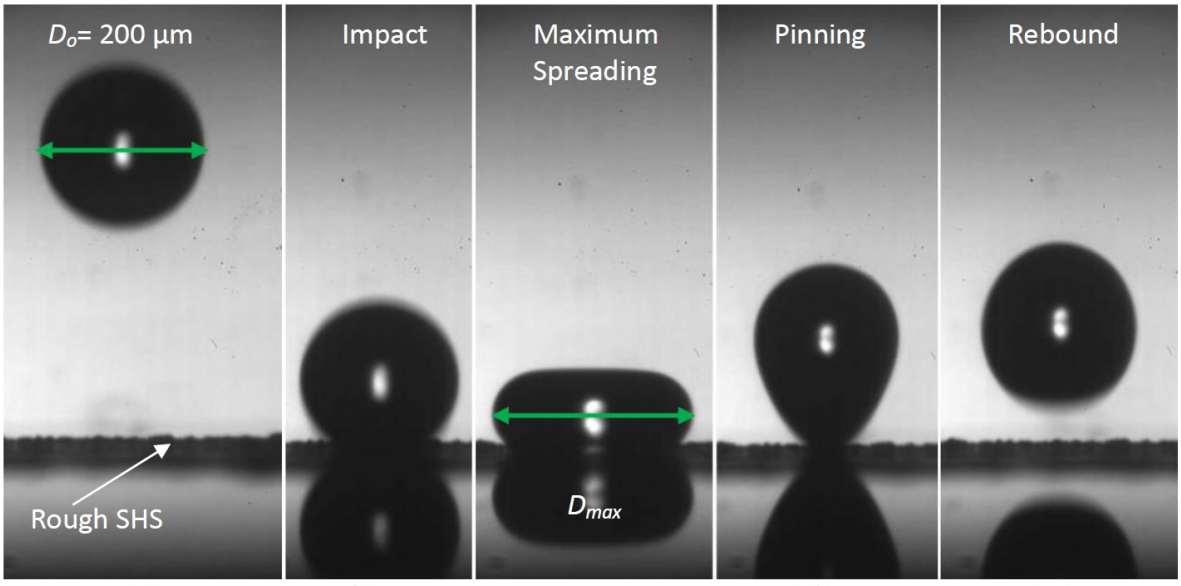

Figure 2.21 Snap shots of the rebounding on SHS showing droplet (a) initial diameter, (b) at the first impact on the SHS, (c) maximum spreading, (d) pinning, and (e) rebounding

In addition, for results verifications, experiments for the same microdroplet diameter were performed on four identically prepared superhydrophobic substrates. The obtained results were averaged and compared for increased validation and accuracy. The same methodology was

followed for the hydrophilic polished aluminum substrates, which were cleaned using ethanol between experiments and completely replaced after 30 experiments, similar to the SHS. Table 2.4 illustrates an example of the different average measured parameters for a 20 µm droplet. The errors in mean values are presented as a percentage difference in the attained results on the hydrophilic and superhydrophobic substrates. Moreover, the maximum and minimum results' deviation are also added to the table in a symmetrical pattern. The SHS showed the highest variation in results due to its high surface roughness (i.e. peaks and valleys in topology). However, even with such high roughness (i.e. R_a=1.6 µm), there was a maximum of 5% variation in results. Accordingly implemented substrates where considered to be homogenous with an acceptable range of error.

Parameter	No. of experiments (on one sub.) x No. of Sub.	Results of a 20 µm droplet	Percentage Error
Contact time (µs)			
SHS	30 x 4=120	9 ± 0.22 µs	5%
Al (settling)	30 x 4 =120	30 ± 0.3 µs	2%
Max. spreading(µm)			
SHS	30 x 4=120	25 ± 0.5 µm	4%
Al	30 x 4=120	26.8 ± 0.4 µm	3%
Restitution coefficient			
SHS	30 x 4=120	0.32 ± 0.008	5%
Maximum height (µm)			
Al	30 x 4=120	16.8 ± 0.2 µm	2.4%
Incipient velocity (m/s)			
SHS	10 x 4=40	115 ± 2 m/s	3.5%
Al	30 x 4=120	85 ± 0.5 m/s	1.2%

Table 2.4 Percentage error of measured impact parameters on Al hydrophilic and superhydrophobic substrates

Binary conversion errors

The binary images conversion is done by setting a threshold reference, where all the light intensities above that threshold are turned into white (i.e. 1) and all those below that threshold to black (i.e. 0). However, errors do exist in such an approximation for grey scale, where an approximate of such associated error which can be achieved by comparing the 50% threshold to a 90% and a 10% threshold. Figure 2.22 illustrates such comparison by showing a raw image, Figure 2.22 (a), and compares the effect of the different thresholds for binary conversion in Figure 2.22 (b) and (c). The gray zone described in Figure 2.22 (c) shows the region that is considered to be a droplet if a threshold between 10% and 90% is used. This region has an approximate maximum size of five pixels, which could be considered as an uncertainty associated with converting an image to binary.

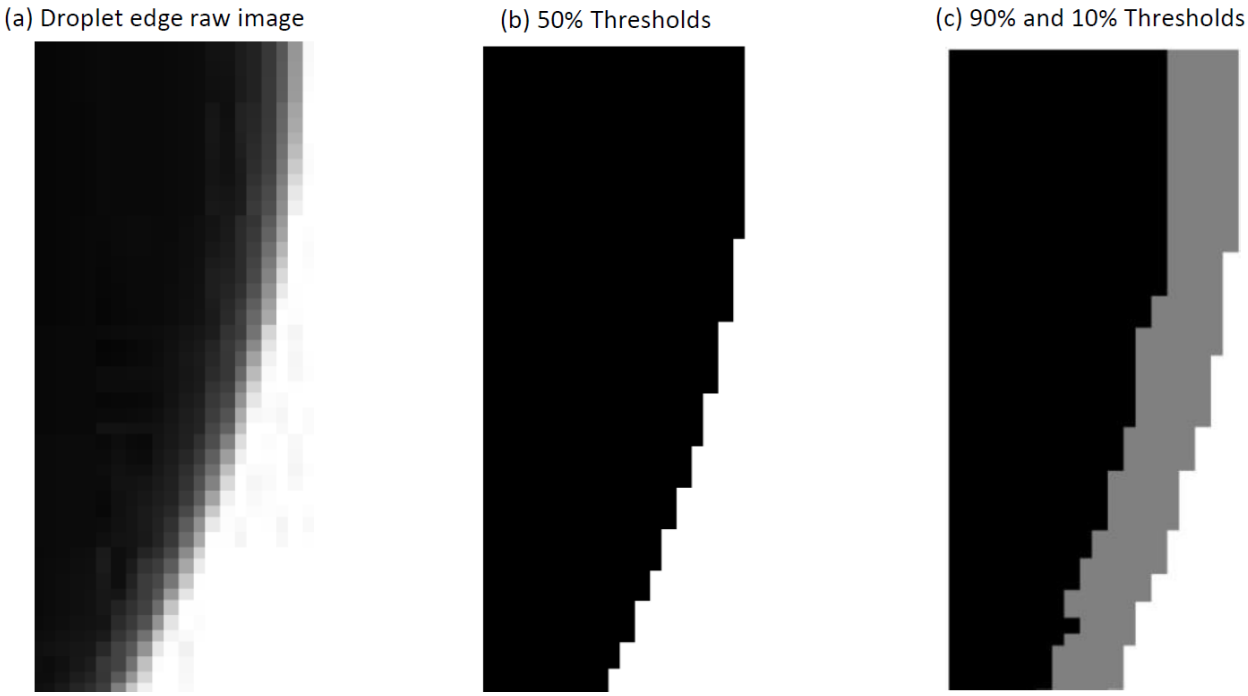

Figure 2.22 Binary conversion details

Chapter 3

Impact Dynamics

This chapter will discuss the impact of droplets on the hydrophilic and superhydrophobic surfaces. Those two substrates are selected as they show distinct behaviors through different impact parameters such as the droplet maximum spreading, contact diameter, contact time, oscillations on the hydrophilic substrate and recoiling on the superhydrophobic surface.

Different droplets sizes (i.e. diameters) have been used in the current analysis to cover a wide range, up to 5000 μm. However, in the current Chapter, only results between 10 – 2500 μm are illustrated to pinpoint the difference between the results obtained for the different droplets sizes. For the purpose of the presentation of the obtained results, the droplets are divided into two different categories. The first one describes the large sub-millimeter and millimeter-sized droplets with diameters between 150 to 2500 μm, which is represented by a 200 μm droplet. The second denotes the cloud-sized droplets, with diameters less than 100 μm that is represented by a 20 μm droplet. The experiments were conducted for a range of impact velocities between 0.2 to 2.5 m/s, with a 0.1 m/s increment. This was done for the entire presented droplets size range, (i.e. between 10 to 2500 μm). A test matrix of all droplets sizes (D_o) and impact velocities (V_1) is provided in Figure 3.1. Tables in Appendix E describe in details all these values with their corresponding Reynolds and Weber numbers. The large first category of droplets showed minor oscillations and rotations before impact. Accordingly, for increased accuracy, the initial diameter of the droplet in such a range was determined by taking the average of droplets height and width 10 frames prior to impact, and then averaged. On the other hand, the second small category of cloud-sized droplets showed almost no oscillations nor rotations before impact.

Regarding the impact outcome explained earlier in Chapter 1 section 1.3, only deposition on hydrophilic substrate and complete rebounding on SHS are encountered. No splashing is perceived due to the small droplets size and low velocity used in the current study. This was visualized experimentally and also checked using the critical dimensionless numbers for splashing described previously by different researchers. For example the splashing critical value $K = We.\ Oh^{-2/5}$ [46], where Oh represents the Ohnesorge number (i.e. $Oh = We^{1/2}\ .\ Re$).

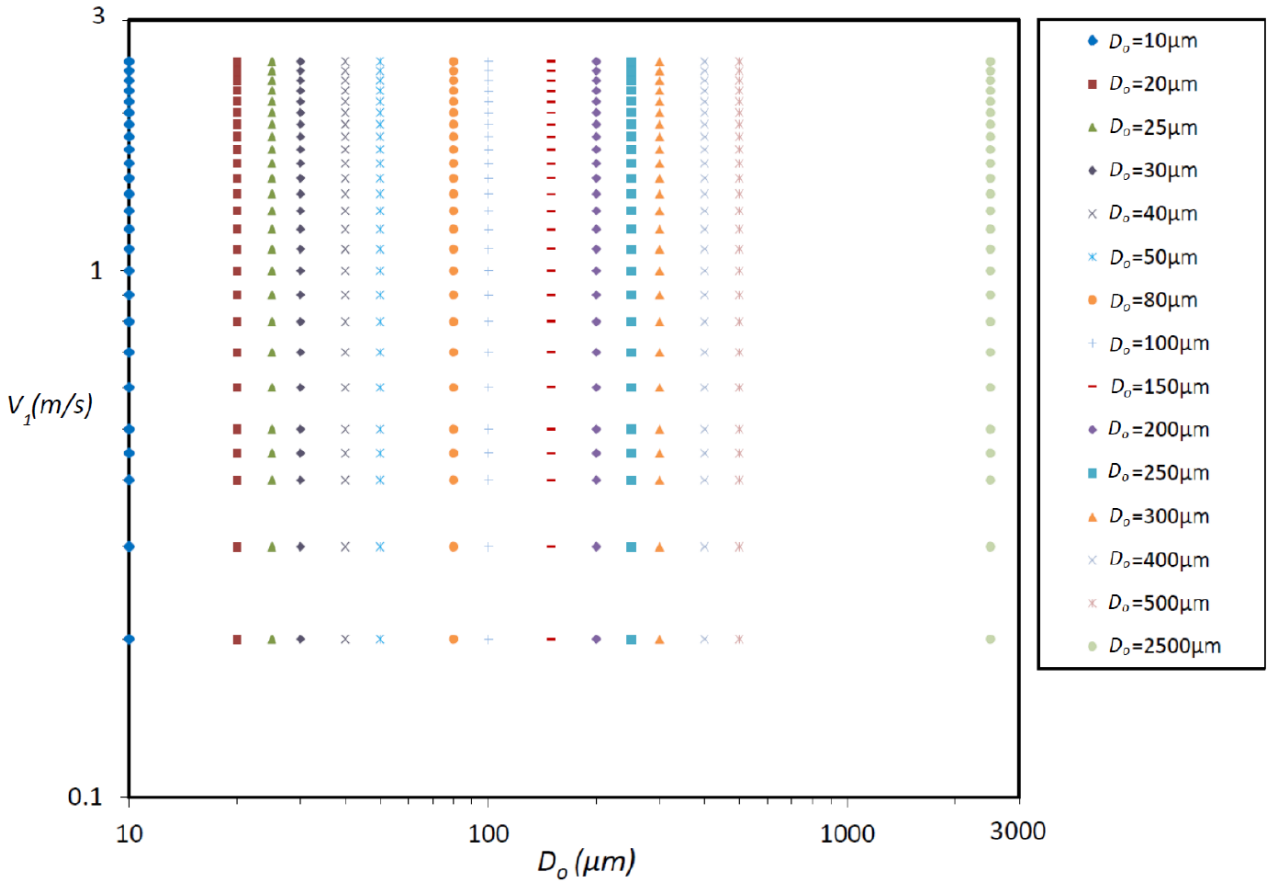

Figure 3.1 Test matrix for the various droplet sizes (D_o) and impact velocities (V_1)

For the chosen droplets sizes and impact velocities, the entire experiments were performed in the capillary regime. In such a regime the viscous effects are minimized and surface tension dominates droplets deformation and spreading. No transition between regimes, (i.e. capillary to viscous) is encountered due to the small droplet size and low impact velocities. This is demonstrated in Figure 3.2, where all the obtained experimental results lie below the solid line described by Clanet *et al.* in [101] for parameter space $P = 1$, which separates the two regimes, where $P = \mathrm{We/Re}^{4/5}$.

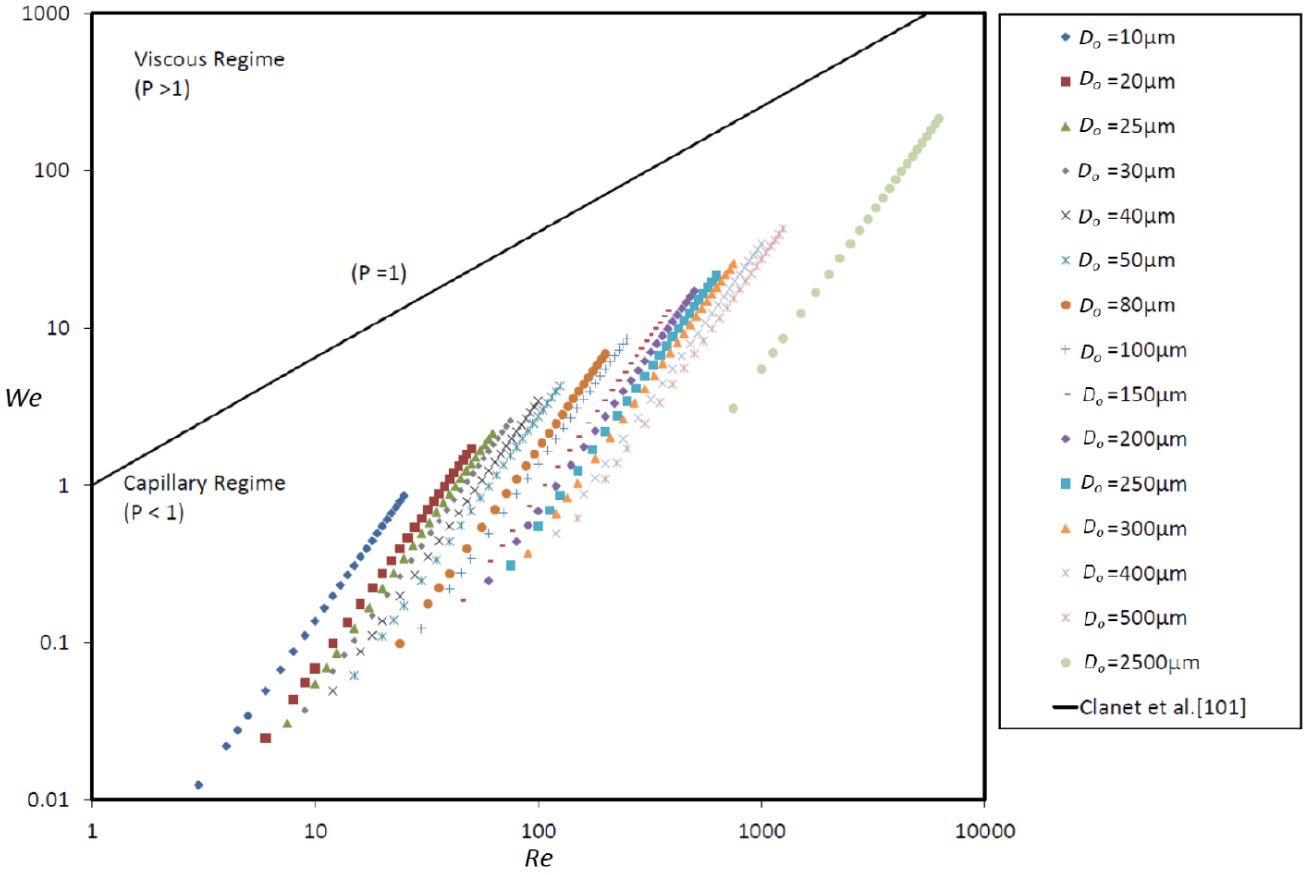

Figure 3.2 Map of different impact flow regimes

3.1 Effect of droplet size on the outcome of impact

In this section, the droplet Weber number is kept constant at 0.7 in order to examine the behavior of the two previously described categories of droplets on hydrophilic and superhydrophobic substrates. As mentioned earlier, large droplets are represented by a 200 µm droplet and small cloud-sized droplets are represented by a 20 µm droplet. In order to achieve the same We = 0.7, the 200 µm attains an impact velocity of V_1= 0.5 m/s while the 20 µm has an impact velocity of V_1= 1.6 m/s.

All the technical details of the experimental setup were explained in details earlier in Chapter 2. In order to visualize and record the impact dynamics of the 200 and 20 µm droplets, the high speed camera parameters (fps and shutter speed) are chosen to give the ultimate images quality. Figure 3.3 and 3.4 illustrate snap shots of the impact process on the SHS for the 200 and 20 µm droplets, respectively. Additional impact images of the 20 µm droplet are illustrated in Appendix F.

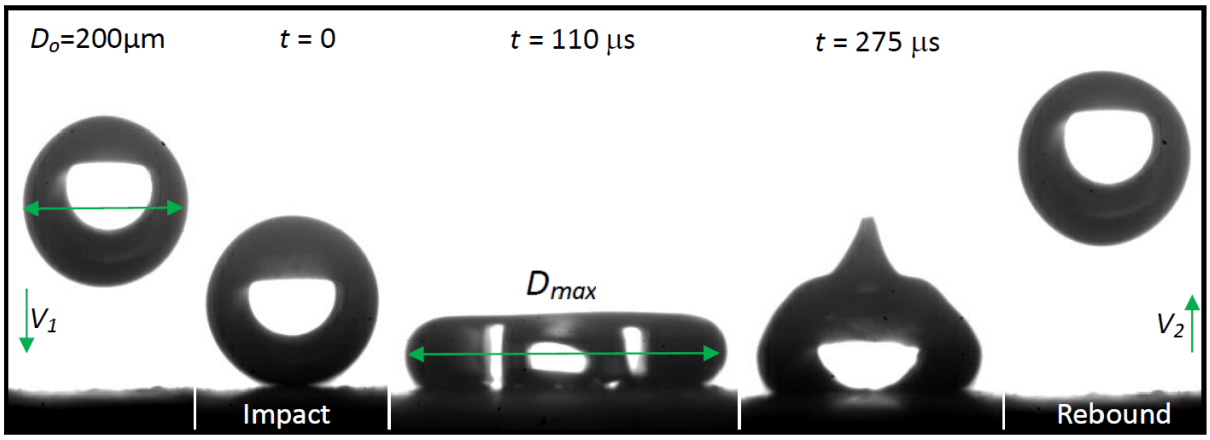

Figure 3.3 Sequential images of a single 200 µm droplet impact on the SHS

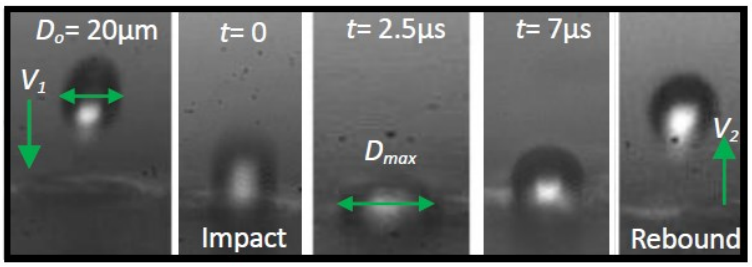

Figure 3.4 Sequential images of a single 20 µm droplet impact on the SHS

The large difference between the parameters needed for the two droplets sizes was due to the need of a higher spatial and temporal resolution in case of the 20 µm droplet. These were required in order to capture the complete impact scenario by using a single 20 µm droplet that impacts on one specific location. This was in contrast to flash-videography and substrate displacement that was implemented for previous studies. Those performed the impact for several droplets at different delay times then put all together in order to understand the whole impact process. This presented a source of error regarding droplets repeatability and surface homogeneity, due to the continuous change in droplets locations that affected the obtained results. All of which are avoided in the current study.

The comparisons between the two categories of droplets are summarized in the sections to follow. First the results of contact diameter and droplet height against time on hydrophilic and superhydrophobic surfaces for both 200 and 20 µm droplets at the same Weber number are

demonstrated. In addition, droplets spreading are examined on both substrates. Finally recoiling (i.e. bouncing) is investigated for the entire range of droplets on the superhydrophobic surface.

Impact on hydrophilic surface

Droplets impingement and oscillations on the hydrophilic surface are obtained. This is achieved by finding the droplets contact diameter and height, respectively. The contact diameter against time is first analyzed. The 200 μm droplet impacting the hydrophilic surface resulted in a maximum diameter of D_{max} = 275 μm after 102 μs, see Figure 3.5. It was then reduced to D=188.5 μm, after 442 μs during complete retraction. Finally it increased to an average value of D=212.5 μm, to remain at this diameter for the remaining full testing time of 1200 μs.

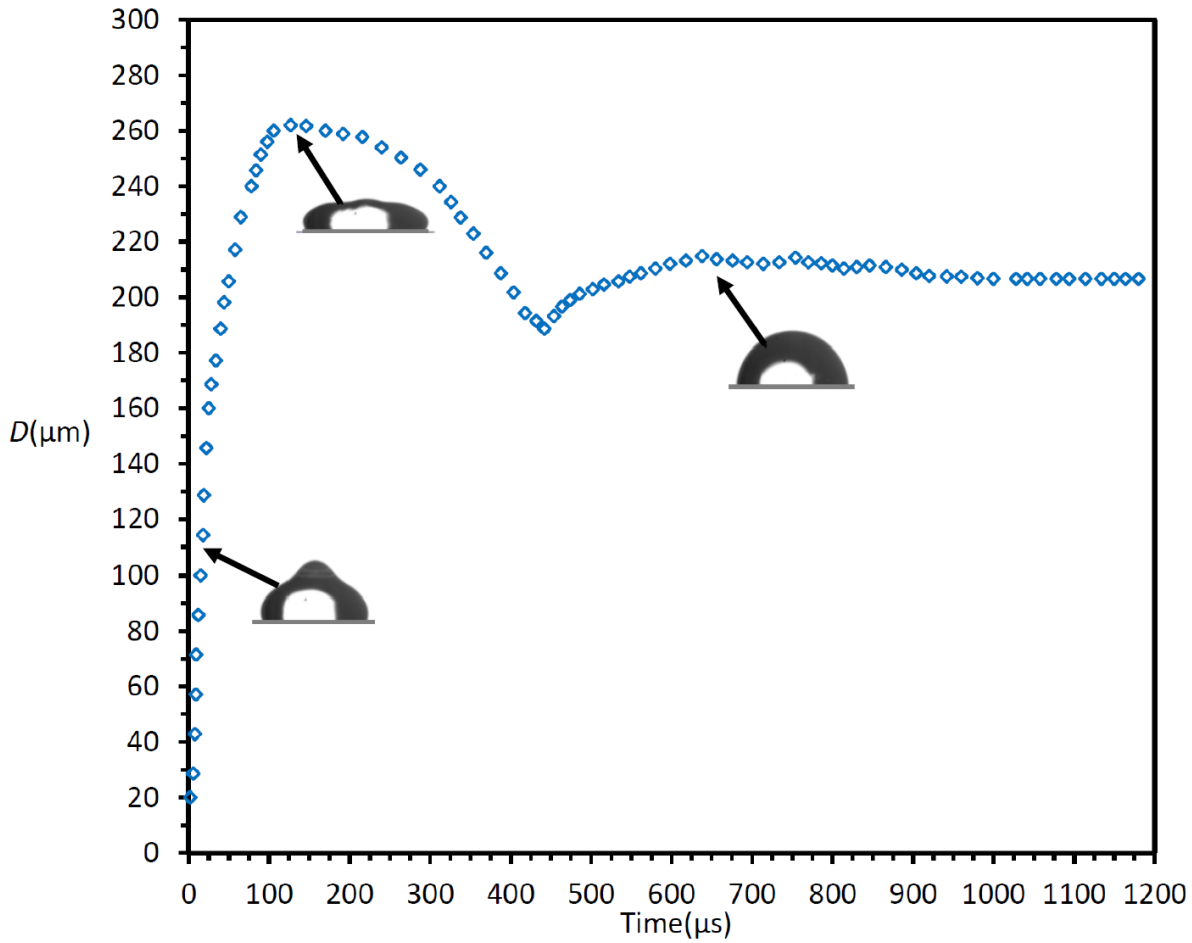

Figure 3.5 Contact diameter of a 200 μm droplet during impact on the hydrophilic Al substrate

On the other hand, the 20 µm with an impact velocity V_1 = 1.6 m/s and the same Weber number *We* = 0.7, reached a maximum diameter of D_{max} = 26.8 µm after 9 µs, as illustrated in Figure 3.6. A minimum value of *D* = 24 µm was obtained at *t* = 11 µs, due to retraction. After which the 20 µm settles on the surface with a contact diameter of *D* = 25 µm. Comparison of the two figures demonstrates lower retraction behavior for the 20 µm droplet. This is mainly due to the dominant effect of the droplet pinning attributed to the 20 µm droplet compared to that of the 200 µm droplet with a volume ratio of 10^{-3}.

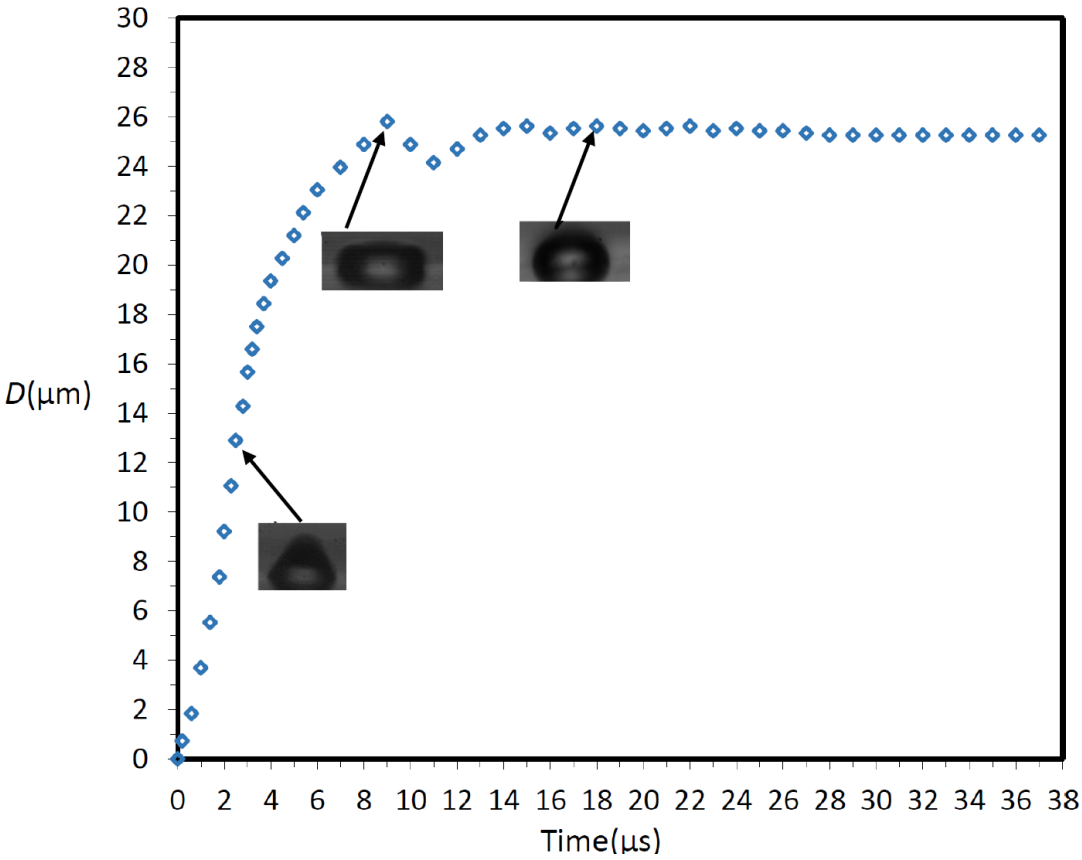

Figure 3.6 Contact diameter of a 20 µm droplet during impact on the hydrophilic Al substrate

Secondly the droplets height against time is obtained during impact in order to illustrate their oscillations on the hydrophilic substrate. The height (*h*) of the 200 µm droplet on the hydrophilic substrate is illustrated in Figure 3.7. After 102 μs the height reaches a minimum value of h_{min} = 57 µm, which correspond to the maximum droplet diameter. Recoiling of the droplet allows a maximum height of h_{max}=143 µm to be attained by the droplet after impacting

the substrate, *at t* =185 μs. The energy conversion between inertia and surface energy, combined with the damping effect by the viscosity, lead to the pseudo-periodic evolution of the droplet height. The droplet oscillation continues to change the height until finally settling with an average value of h = 90 μm after around 1120 μs.

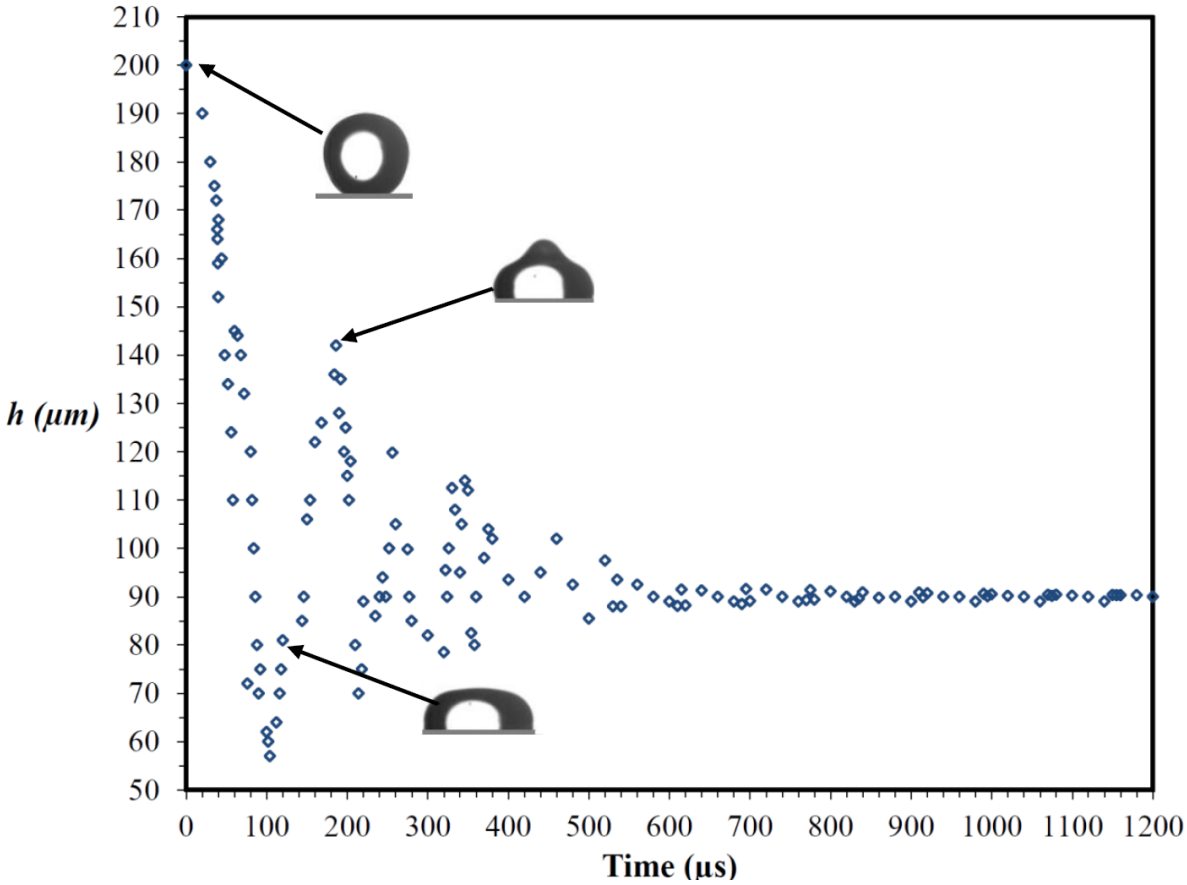

Figure 3.7 Height of a 200 μm droplet during impact on the hydrophilic Al substrate

Similar results for a 20 μm droplet are presented in Figure 3.8 where the droplet reached a minimum height of h_{min} = 9.5 μm after 9 μs from the beginning of impact, at which the maximum diameter of the droplet occurs. The retraction phase allowed the droplet to reach a maximum height of 16.8 μm after 13.5 μs and then final height for settling was 12.8 μm. The 20 μm droplet had much less oscillations when compared to the 200 μm droplet due to its higher surface-to-volume ratio.

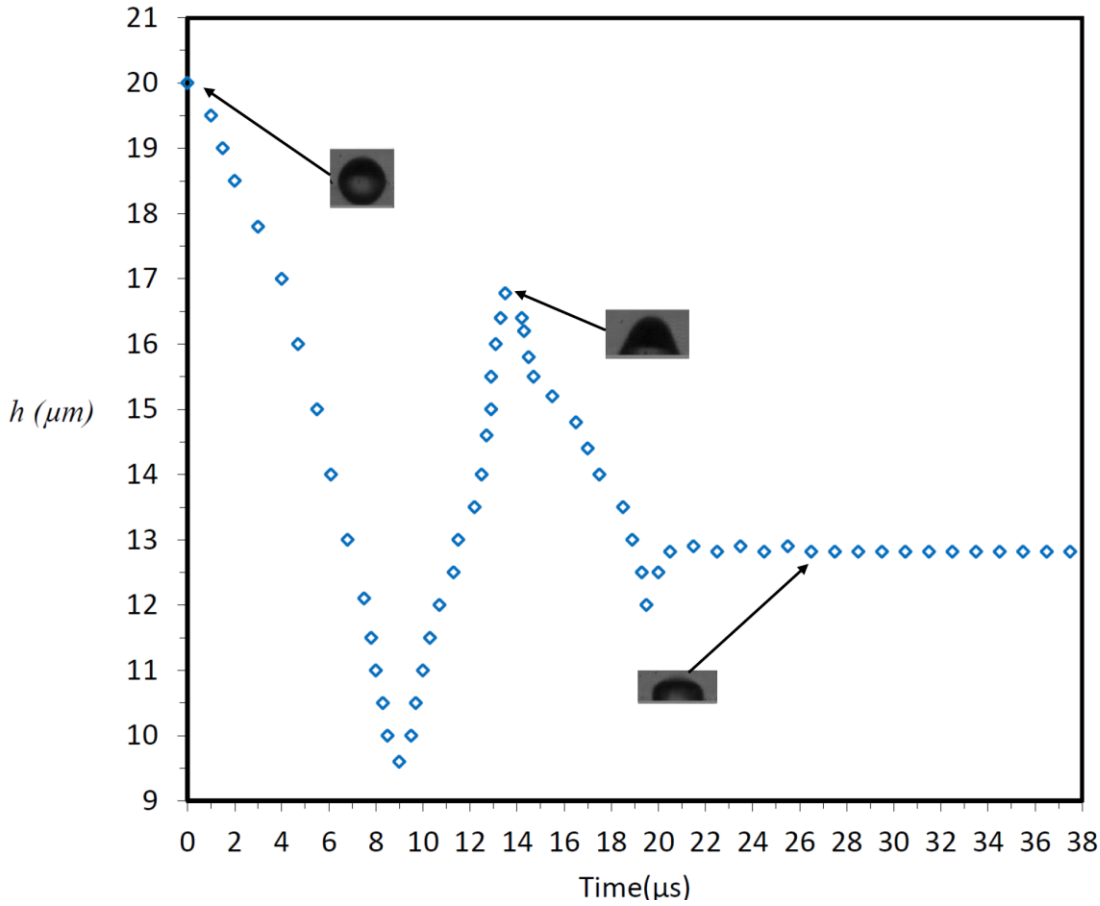

Figure 3.8 Height of a 20 μm droplet during impact on the hydrophilic Al substrate

Impact on superhydrophobic surface

The contact diameter against time is examined for both droplets sizes during their impact on the superhydrophobic surface. The results are depicted in Figure 3.9 and Figure 3.10 for 200 and 20 μm diameter droplets, respectively. As expected, both droplets spread, recoil and bounce off the SHS.

First, the 200 μm droplet reaches a maximum diameter of D_{max} = 266 μm after 110 μs, see Figure 3.9. The droplet takes an average of 450 μs to completely impact, deform and bounce off the SHS. Its shape did not deform completely to form a recoiling jet shape during its recoiling phase. However, a small peak is formed on the top central portion of the drop during recoiling, as illustrated in Figure 3.9. This behavior is due to the low Weber number attained by the droplet upon impact. In addition, a negligible difference is obtained upon comparing the droplet impact velocity, V_1, to its rebounding velocity, V_2. Accordingly it bounces for several times before finally settling on the SHS.

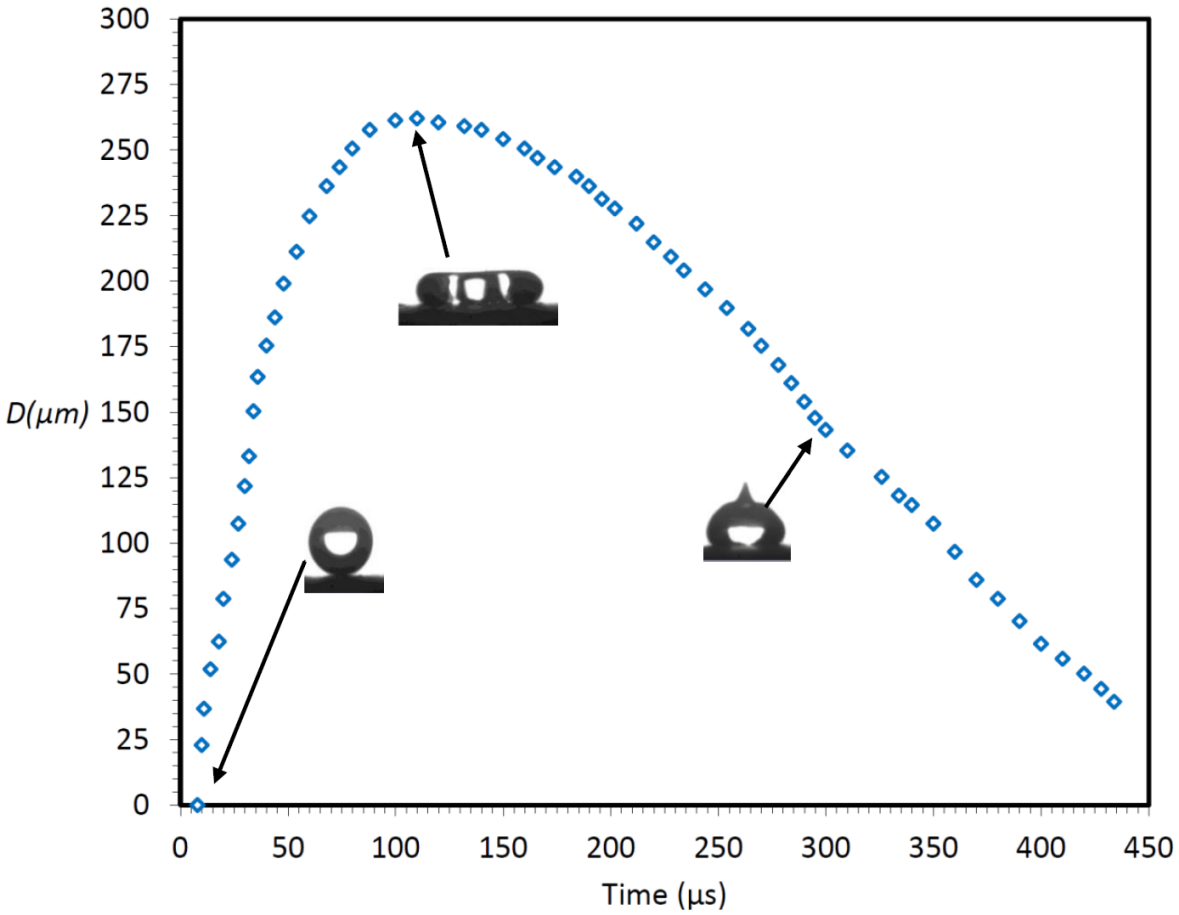

Figure 3.9 Contact diameter of a 200 μm droplet during impact on SHS

Furthermore, the impact of the 20 μm diameter droplets results in a D_{max} = 25 μm at t = 2.7 μs as illustrated in Figure 3.10. It takes approximately 9 μs for the droplet to fully impact and bounce off the SHS. No peaks are formed during the recoiling phase of the droplet, where the droplet attains its original shape with minimum deformation. Furthermore, a much larger reduction in the rebounding velocity is encountered when compared to the 200 μm droplets. This is attributed to the much larger surface-to-volume ratio that is in contact with the substrate in case of the 20 μm droplets. As a result the droplet bounces only once or in some cases twice before settling on the SHS.

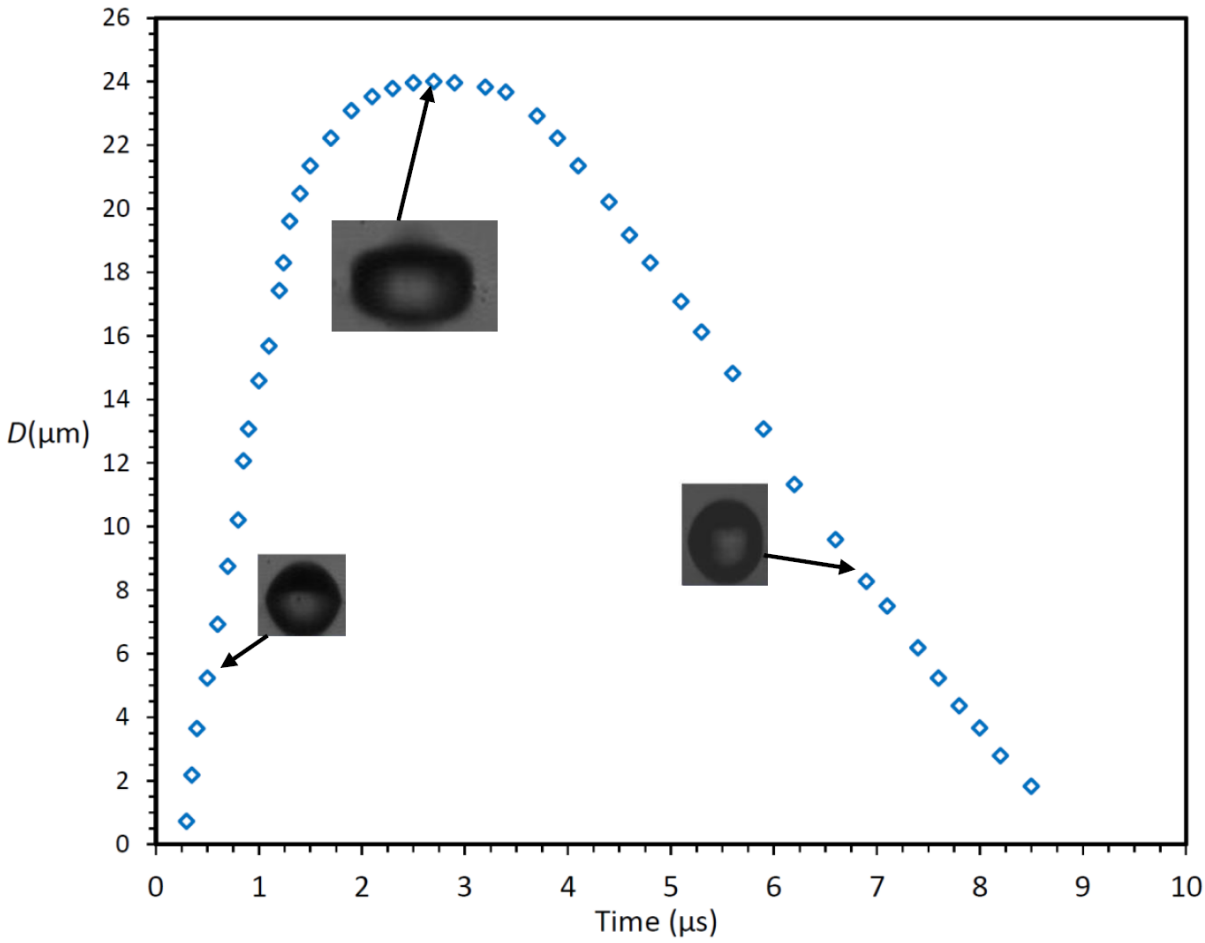

Figure 3.10 Contact diameter of a 20 μm droplet during impact on SHS

3.2 Droplet spreading

The effect of changing the Weber number on the maximum spreading on both aluminum and superhydrophobic substrates is obtained for the entire range of droplet sizes and impact velocities. In general, the maximum spreading diameter on the SHS is lower than that on the hydrophilic substrate for both categories of droplets. This is attributed to the surface roughness effect that increases the viscous dissipation during the primary phase of impact. Accordingly such a reduction in droplets' spreading is elaborate for the cloud-sized droplets, where the droplets size is comparable to the substrates' average surface roughness value, especially in the case of the SHS.

For the hydrophilic substrate, the normalized maximum spreading diameter (D_{max}/D_o) reaches an average value of approximately 1.36 for the entire droplet sizes from 10 to 500 μm, see Figure 3.11. Such an approximate plateau continues for larger droplets that are 2500 μm in

diameter. These results resemble the results obtained by Van Dam and Le Clerc [47] for droplets of the same range of sizes on a hydrophilic glass plate. On the other hand, for the normalized maximum spreading diameter on the SHS, the value of D_{max}/D_o varies from 1.23 for the 10 µm droplets to 1.37 for the 500 µm droplets. It then increases to 1.39 for the 2500 µm diameter droplet. Plots of the model given by Pasandideh-Fard *et al.* [97] are added on Figure 3.11 with input angles chosen as ($\theta = 180°$) to represent a perfect SHS and ($\theta = 160°$) that corresponds to the SHS used in the current study. The two plots show the same trend and saturate at such a low Weber number. It also shows that such model fails to simulate the performance of cloud-sized droplets. This is because the assumption of a small boundary layer thickness is not valid at such very low inertia. The air layer entrapped under the droplet could be a factor to consider, however the roughness scale in comparison to the droplet size is considered the main reason for the variation observed for (D_{max}/D_o) on the superhydrophobic substrate.

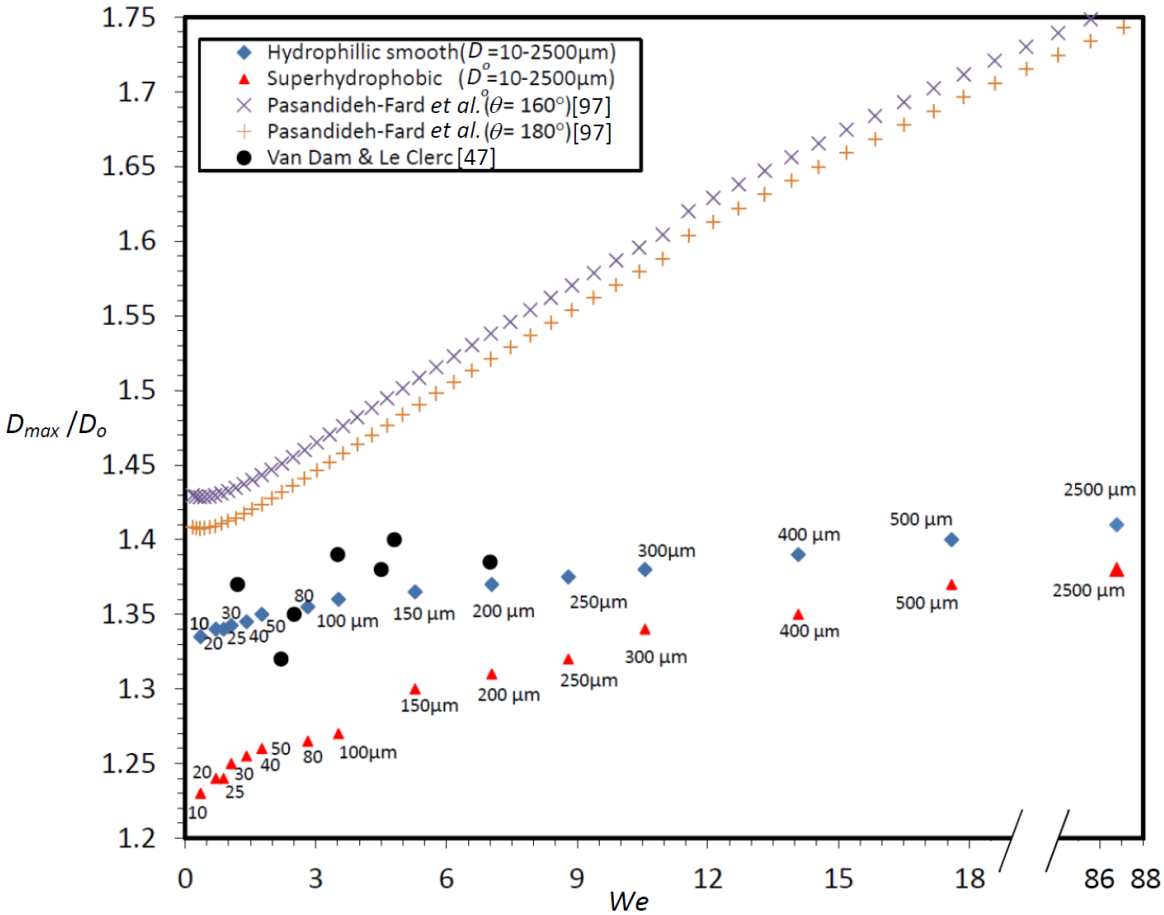

Figure 3.11 Normalized maximum spreading diameter against Weber number on smooth hydrophilic aluminum and superhydrophobic substrates

Due to the importance of surface roughness in the current study, its effect on the maximum spreading is quantified in Figure 3.12 by plotting (D_{max}/D_o) against the droplets relative roughness (R_a/D_o). A decreasing trend for the maximum spreading factor is shown as the size of the microdroplets decreases from 2500 to 10 µm droplets. This was due to the inability of small droplets to completely spread during impact as a result of the surface roughness, which was scalable to the droplet size. The obtained trend explains the normalized maximum spreading figure illustrated in Figure 3.11 and emphasizes that such behavior is mainly due to the substrates surface roughness. This is especially true when using large droplets sizes, where the normalized maximum spreading overlaps for both substrates. Consequently, this confirms that the wettability difference is not the main reason for the deformation difference (i.e. change between D_{max}/D_o values for both substrates). Instead the relative roughness is the main difference, which becomes irrelevant as the droplet size increases (i.e. beyond 3500 µm).

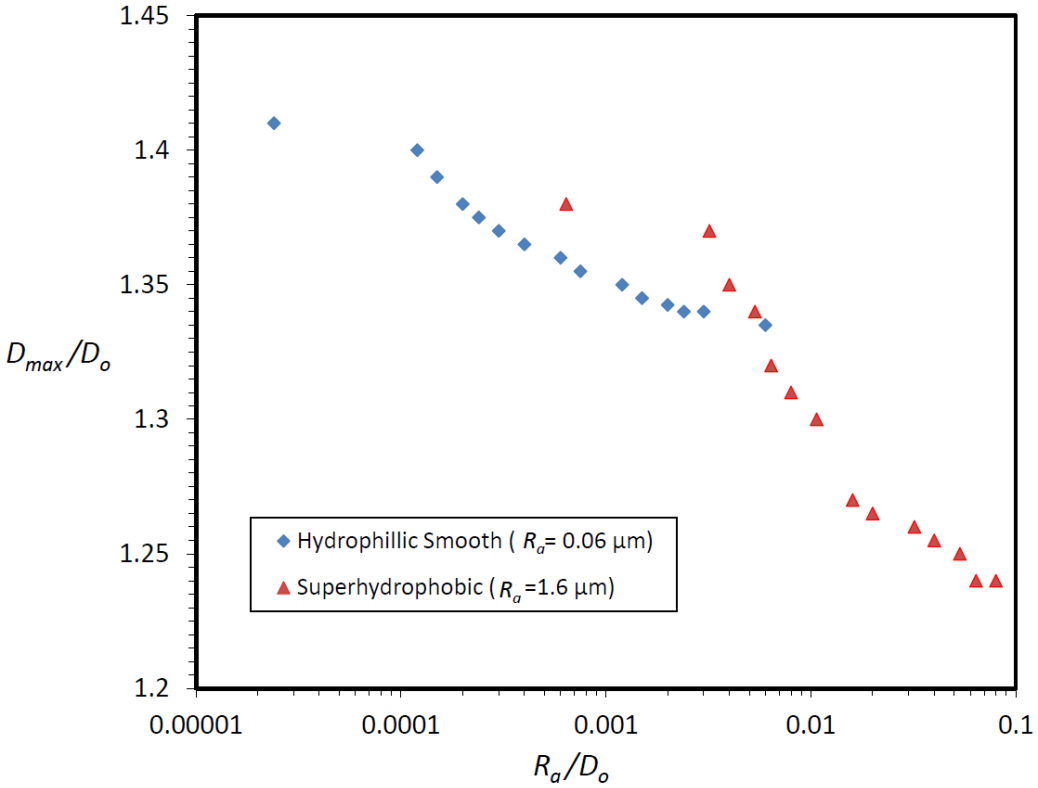

Figure 3.12 Dependence of the normalized maximum spreading diameter on the relative roughness

3.3 Droplet bouncing

The bouncing phenomenon only occurs upon the impact of a droplet on superhydrophobic surfaces. One of the primary parameters when studying bouncing droplets is the contact time.

The contact time is defined as the total time a droplet remains in contact with the substrate during the impact process before rebounding. The contact time generally shows almost no dependency on the droplets' velocity of impact, see Appendix G, but is mostly controlled by the droplets' diameters as illustrated in Figure 3.13. This is similar to the results obtained by Richard *et al.* [132] by balancing inertia effect ($\rho D_0/t_c^2$) with capillarity one (γ/D_0^2), which yields the contact time $t_c \sim (\rho D_0^3/\gamma)^{1/2}$. It can be noticed that their contact time can be estimated by a linear fit that holds well for droplets diameters larger than 150 µm. On the other hand, for droplets smaller than 100 µm the trend deviates from the extrapolation of such linear relation as shown in Figure 3.13. This can again be explained by considering the effect of surface roughness, which becomes comparable to the droplet size. Accordingly, the contact time for such small droplets is relatively increased due to the higher surface contact-to-volume ratio. This increased contact time is responsible for the damping of velocity occurring at the cloud-sized scale upon their impact with the SHS. Such reduction is absent for the large droplets, (i.e. diameters larger than 150 µm). This was illustrated in the comparison made between the 20 and 200 µm droplets impact on the SHS in section 3.1.

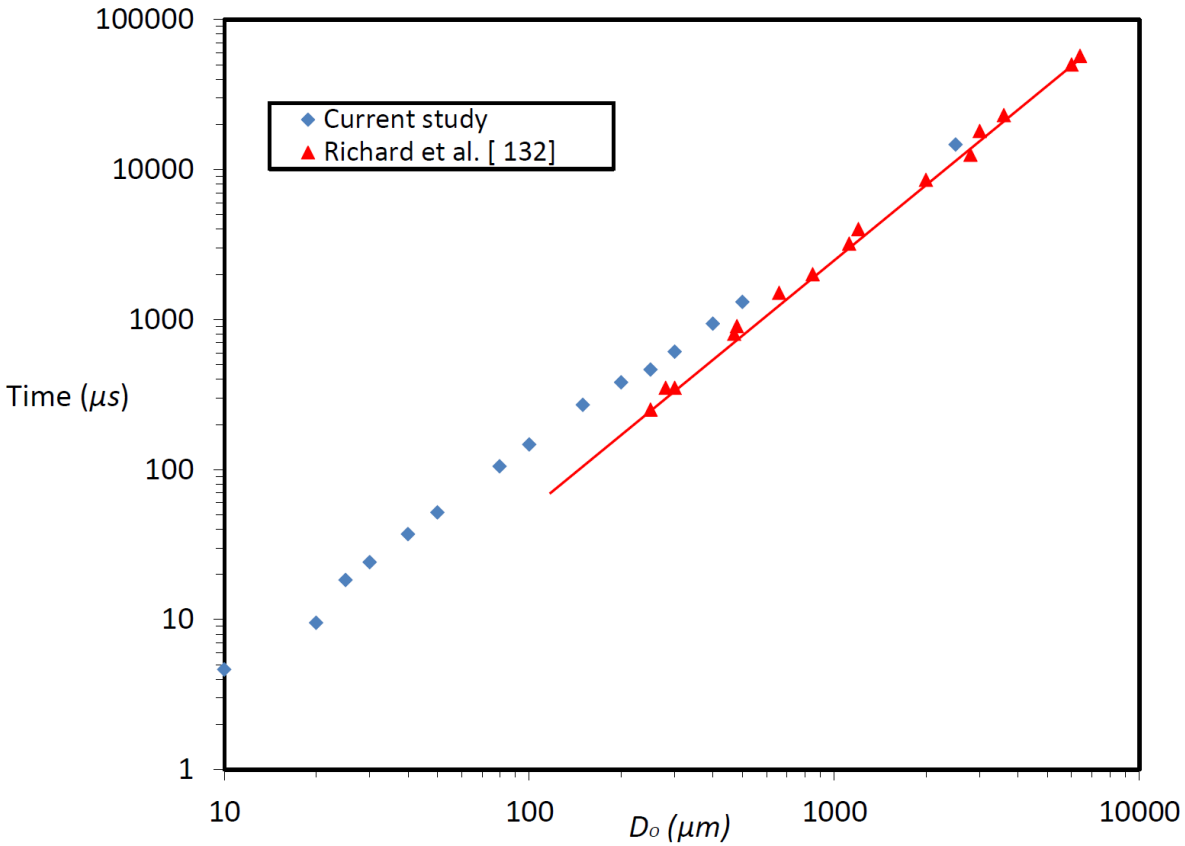

Figure 3.13 Effect of droplet initial diameter on contact time

To further understand and better quantify the effect of surface roughness on the bouncing of different sized droplets, the restitution coefficient is obtained. In such context, Figure 3.14 shows the effect of changing the *We* number by varying the droplet size, for the same impacting velocity V_1=1.6 m/s on the restitution coefficient. As it can be deduced, there is a sharp decrease in the restitution coefficient for cloud-sized droplets compared to submillimeter and millimeter-sized droplets. The restitution coefficient for large sized droplets (i.e. larger than 100 µm) is around 0.9 (± 0.2). However, for smaller droplets the restitution coefficient ranged between 0.28 - 0.65. The main reason behind this decrease is the limited recoil of the small cloud-sized droplets. This limitation comes from the inability of those droplets to completely spread on the superhydrophobic surface during the primary phase of impact. In addition, the pinning of the cloud-sized droplets on the superhydrophobic surface again lowers their recoil. Both of which are a direct result of the SHS roughness that lies in the same order of magnitude as the cloud-sized droplets. Furthermore, the previously described increase in the contact time of these microdroplets increases their energy dissipation during impact. As a result a lower restitution coefficient value for such droplets is obtained.

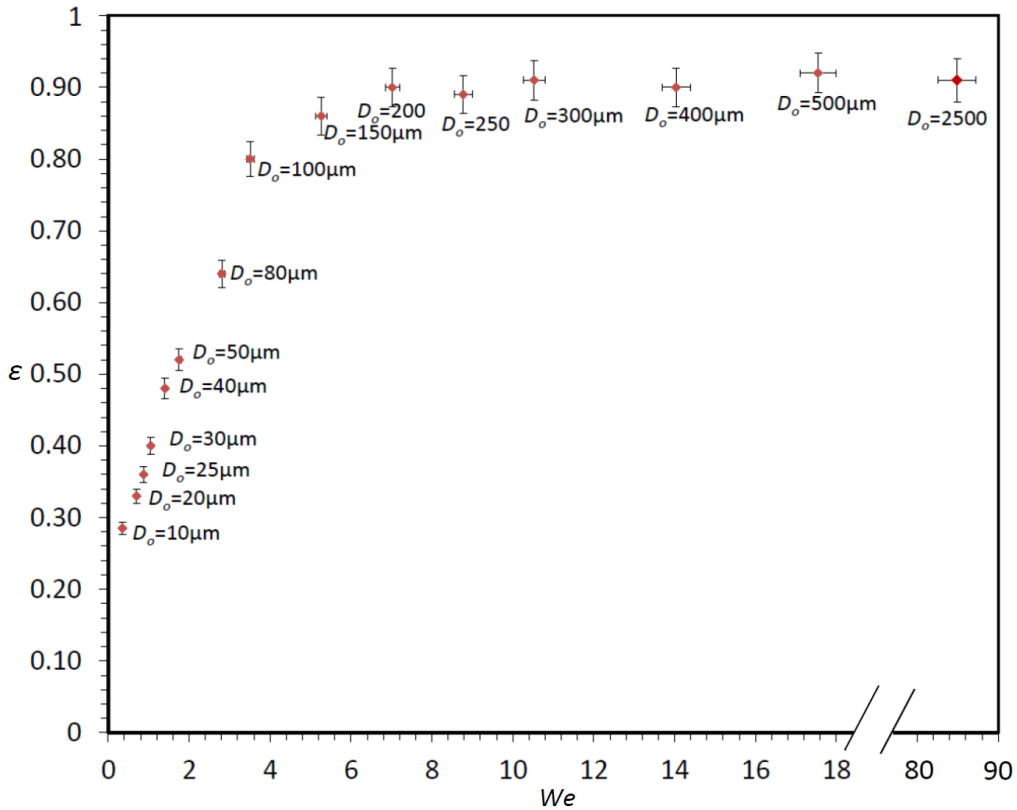

Figure 3.14 Effect of changing the Weber number (i.e. droplet size) on the restitution coefficient at V_1 = 1.6 m/s

Similar to the droplet spreading, further analysis of the restitution coefficient can be made by plotting it against the relative roughness. The effect of such a parameter on the restitution coefficient is described in Figure 3.15. This implies that the smaller the cloud-sized droplets, the more they are affected by the surface topology and roughness. Accordingly this verifies that surface roughness can be the main reason for the reduction in the restitution coefficient (i.e. the decrease in the rebounding velocity, V_2) of the cloud-sized droplets and their general behavior upon impacting the rough SHS. This could be further confirmed by using a SHS with ordered roughness. It can also be validated if a SHS can be chemically obtained with no surface roughness (i.e. completely smooth) in order to be used as a control surface to evaluate the results of the restitution coefficient.

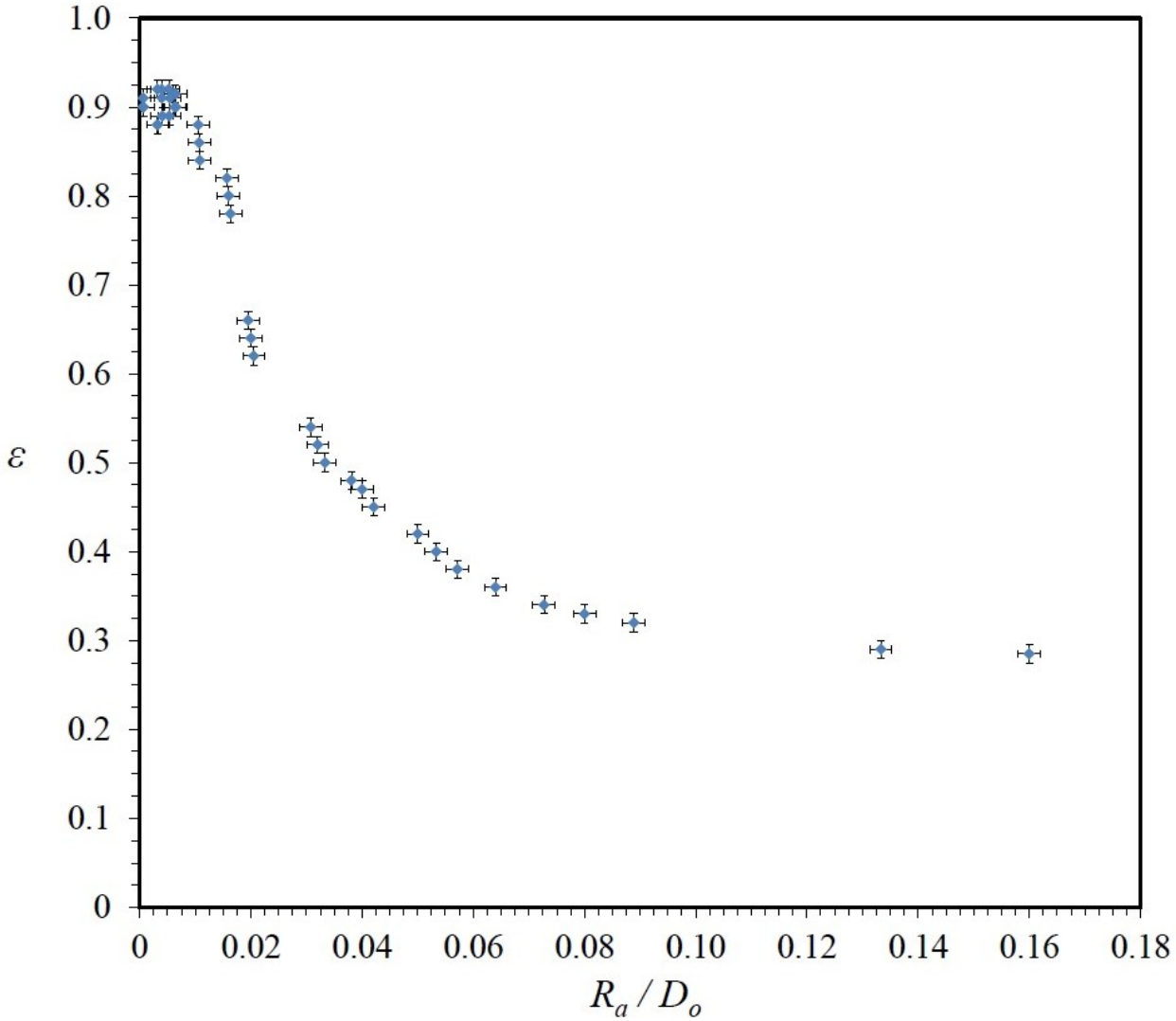

Figure 3.15 Effect of relative roughness on the restitution coefficient

Chapter 4

Shedding of Microdroplets

This section describes the shedding of cloud-sized (less than 100 μm) and sub-millimeter (100 - 200 μm) droplets on substrates of different wettabilitties (i.e. hydrophilic and superhydrophobic surfaces). The experiments were done for a wide range of shedding free stream velocities, U_∞ (m/s), up to 150m/s, to resemble flight conditions. Figure 4.1 illustrates the range of tested droplets with their corresponding air free stream velocities.

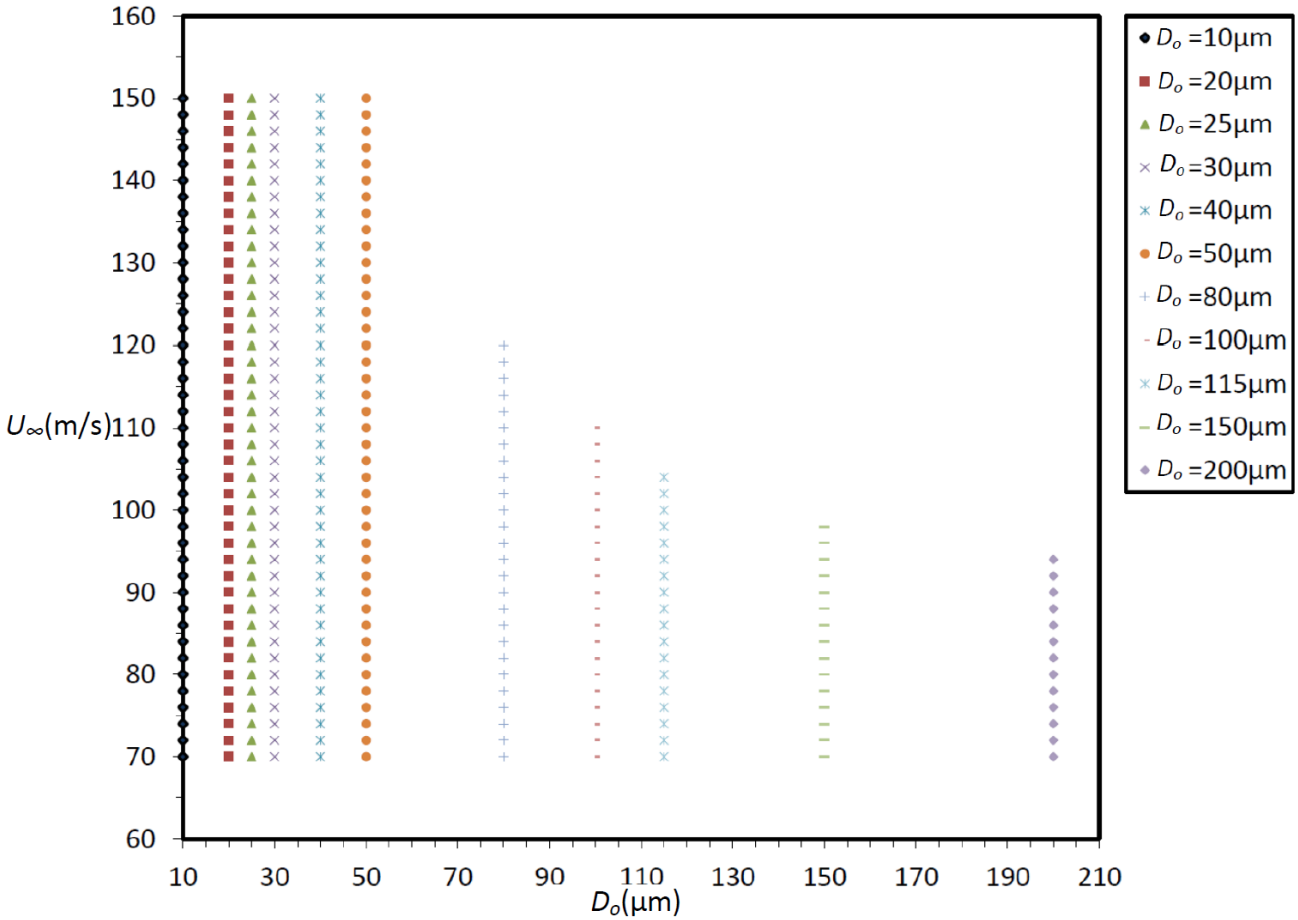

Figure 4.1 Test matrix for various droplet sizes (D_o) and air free stream velocities (U_∞)

Due to the complexity of working with a single cloud-sized droplet, it was not experimentally feasible to give the dispensed droplet an initial impact velocity. The droplets in the range described in Figure 4.1 are each dispensed with negligible velocity of impact (i.e. no vertical air velocity is applied on the droplets such as the one found in real flight condition). After the droplet settles on the tested substrate it is shed with the illustrated velocities (i.e. from 0 – 150 m/s). As described in Chapter 2, section 2.6, the shedding of microdroplets is achieved by using air flow that is produced from a slit nozzle. This air flow is assured to be in the steady state by measuring the droplet settling time and comparing it to the delay time needed to reach steady state by the pneumatic control valve. The steady state was also guaranteed by using a bypass valve, where air flow is continuously generated and allowed to flow in the nozzle just at the right time for shedding.

The conducted experiments are designed and executed in order to find the critical incipient velocity for each droplet size on the tested substrate. This velocity defines the free stream velocity needed to shed the sessile droplet. The tiny size of the sessile droplet makes it lie very close to the substrate surface, buried deeply inside the boundary layer. As a result, the microdroplet encounters a much smaller velocity, $u(y)$ than the free stream velocity, U_∞ that is produced from the nozzle output. This requires higher free stream velocities for shedding than larger droplets (i.e. millimeter-sized), which are mainly subjected to the free stream velocity. This is because the majority of their frontal areas are found outside the boundary layer. A schematic diagram of the experimental setup for the shedding experiments is illustrated in Figure 4.2. The nozzle bottom surface is flushed with the substrate to avoid any flow disturbances. In addition, for the maximum free stream velocity used, (150 m/s) the Reynolds number at the location of the droplet, (i.e. 15 mm downstream from the nozzle output) is approximately 1.5×10^5. This is much smaller than the Reynolds number required for the turbulent transition on a flat plate. Consequently, the droplets are exposed to a laminar boundary layer for the entire range of shedding velocities.

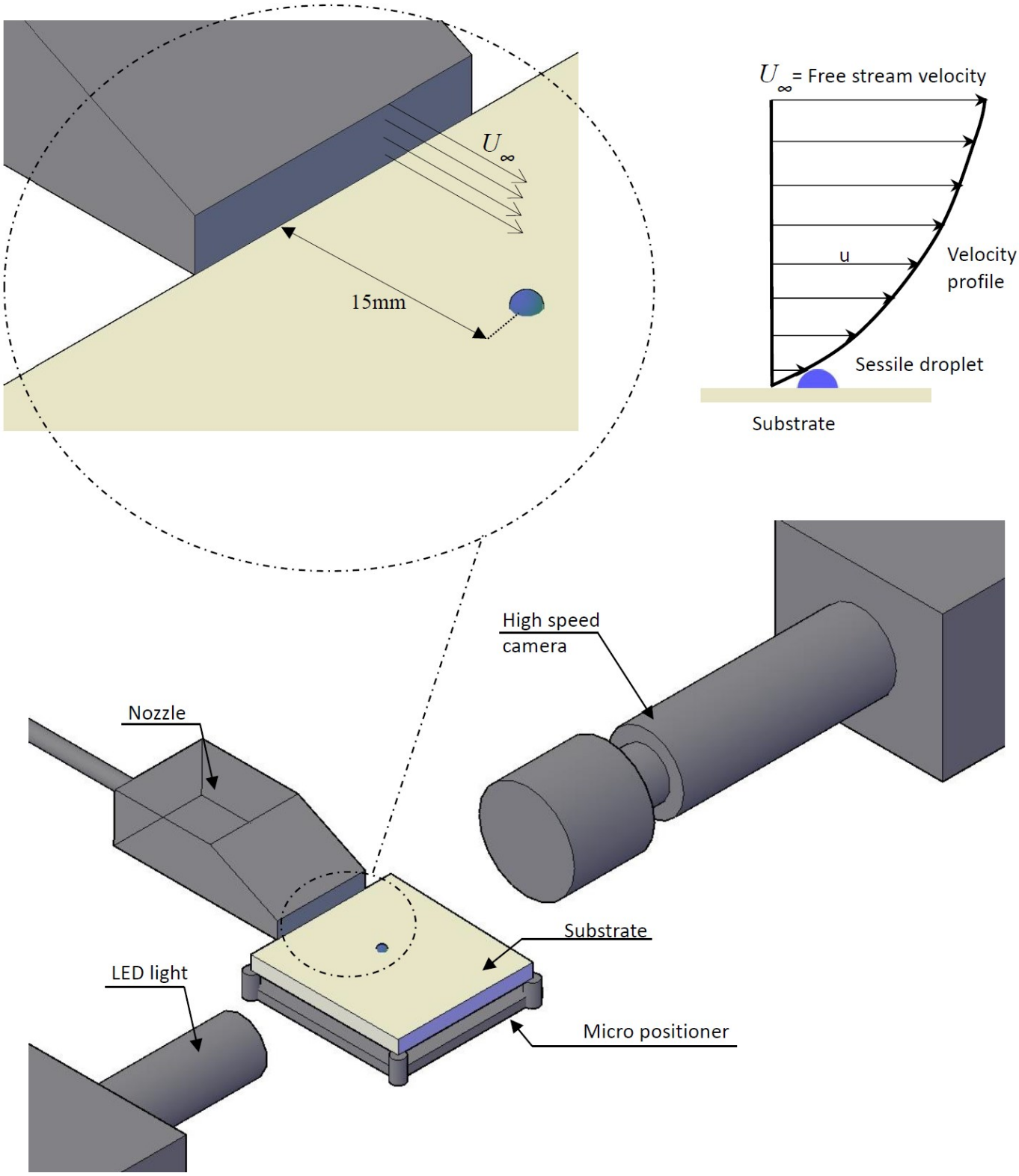

Figure 4.2 Experimental setup for droplet shedding

4.1 Controlling parameters

After neglecting viscous dissipation occurring within the droplet, its shedding will be controlled by a balance between the adhesion and drag forces. The droplet adhesion forces depend on the wetting properties of the substrate upon which the droplet is deposited. The more wettable the surface, the larger the droplet adhesion force. A measure of such adhesion force can be made by the length of the contact line, L_b and the shedding angles θ_{min} and θ_{max}. On the other hand, the drag force depends mainly on the average free stream velocity value, U_∞ *(m/s)* and the shape of the droplet with respect to its frontal area, A (m^2). The drag force needs to overcome the adhesion force in order to successfully shed the droplet. Equations of the drag and adhesion forces were explained in Chapter 1, section 1.4. A schematic of a sessile droplet that is being shed is illustrated in Figure 4.3 to demonstrate all these shedding controlling parameters.

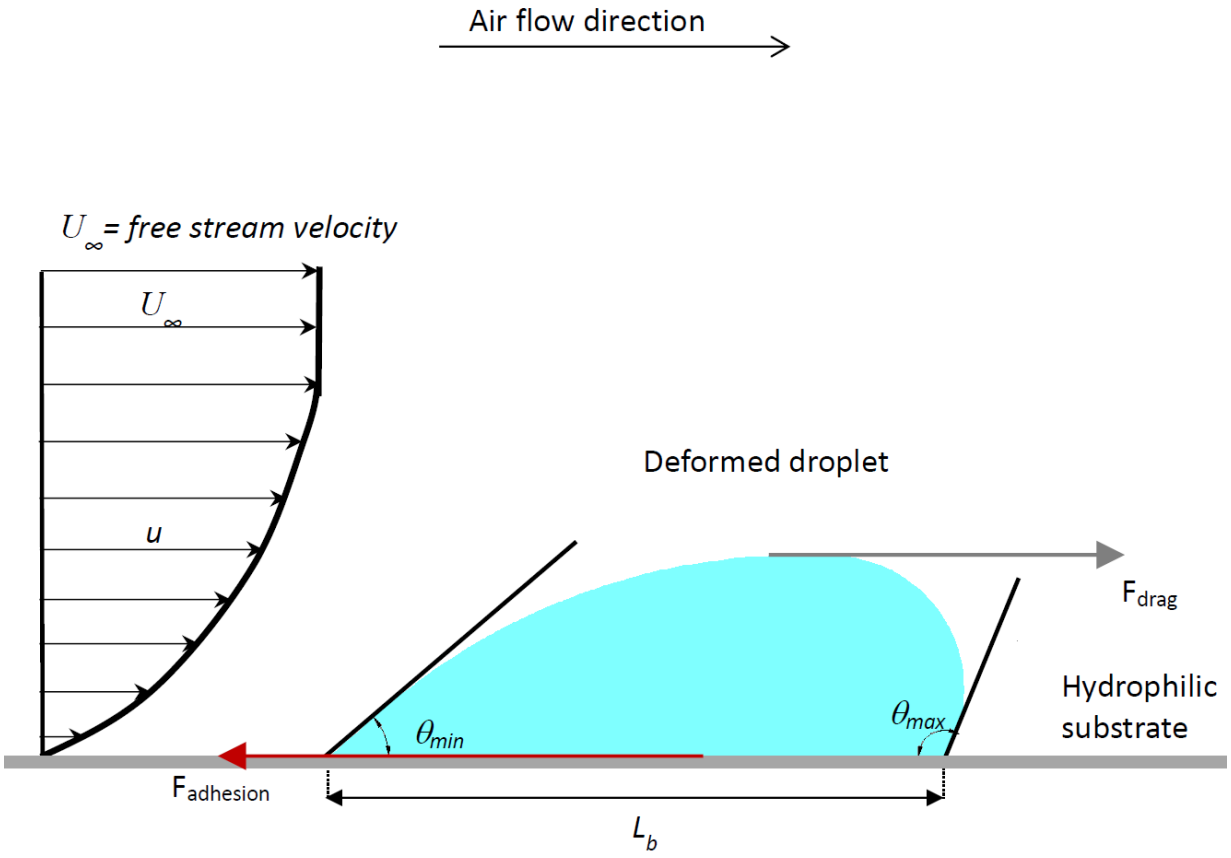

Figure 4.3 Schematic for droplet shedding

The free stream velocities are obtained experimentally using the results from the flow meter and Pitot tube described earlier in Chapter 2, section 2.6. Using the measured free stream velocity, the equivalent air velocity on the droplet, *u (m/s)*, inside the boundary layer close to the surface of the substrate, is calculated. This is done by using a numerical simulation conducted in OpenFOAM 2.1.1. For more details regarding the numerical simulation, please see Appendix C. An illustration of the velocities inside the boundary layer, *u*, that correspond to each free stream velocity for different vertical distances from the substrate is shown in Figure 4.4. The numerical simulation with its refined mesh is considered to be more accurate than the Blasius theoretical analysis which is taken as a reference. This is because the exact geometry of the system, (i.e. nozzle design, droplet position and substrate holder), is taken into consideration in the numerical analysis. On the other hand, the theoretical analysis accounts for none of these parameters. The distribution illustrates a linear velocity profile around the cloud-sized droplets.

In addition, the droplet under test, for the incipient of motion velocity, is deposited on the substrate with minimum velocity of impact. That's the minimum voltage output required for successful dispensing of a single droplet of different sizes (i.e. between 10 - 200 μm). This minimizes the impact oscillations on both substrates. More over the air velocity profile around the droplet is not affected by such impact.

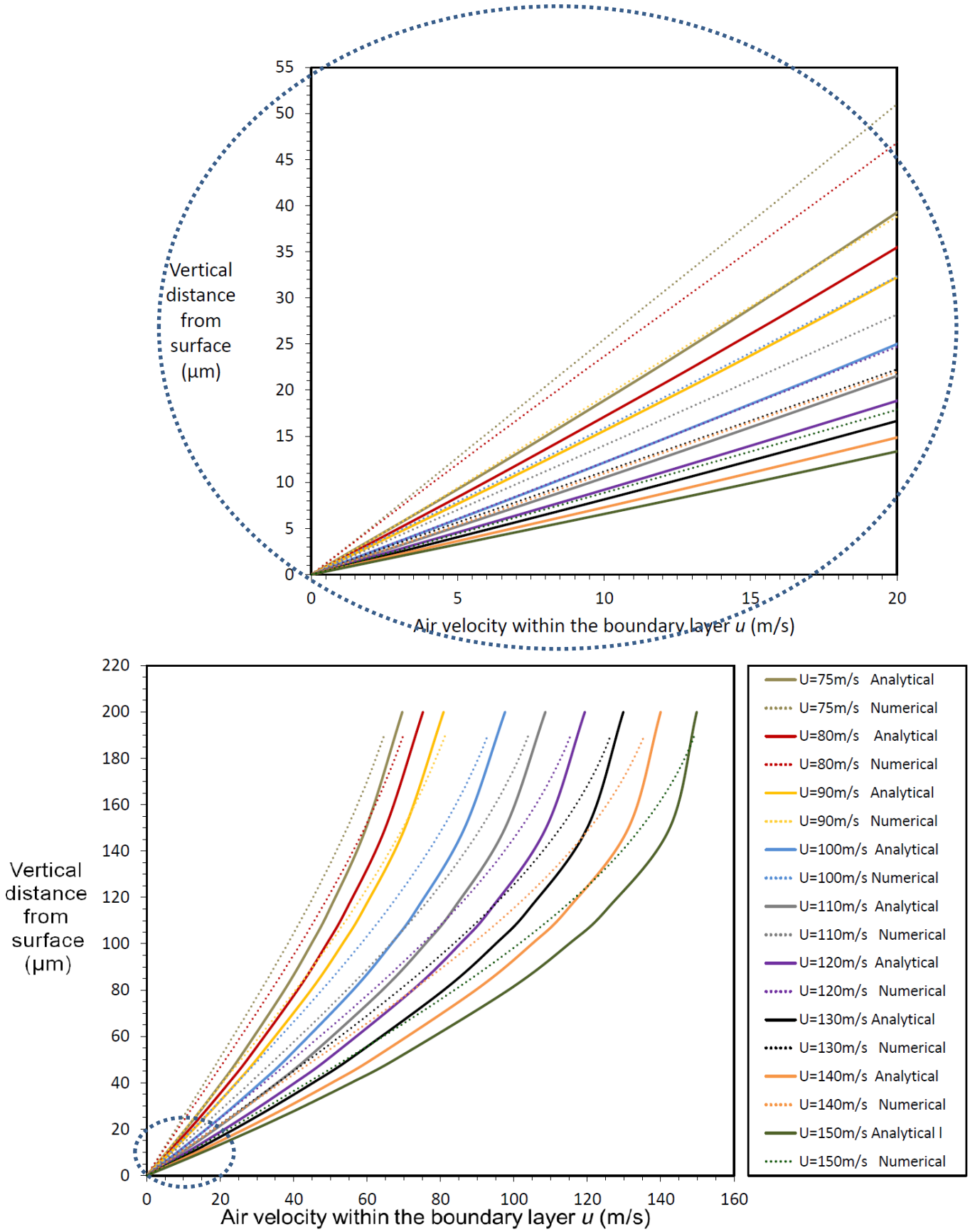

Figure 4.4 Air velocities at different heights from the substrate

Droplet height on various substrates

The shedding experiments are performed on hydrophilic and superhydrophobic surfaces. One of the main differences between these substrates is the height (h) that the sessile droplet attains when it is sitting on the surface. By considering the previously explained boundary layer analysis, it can be deduced that this height affects the incipient velocity needed to shed the droplet. Figure 4.5 illustrates a schematic of the height of the sessile droplets on different substrates. Also by investigating the drag force equation (i.e. equation 1.7), it is clear that as the value of h increases, the frontal area A increases and accordingly the drag force on the droplet increases.

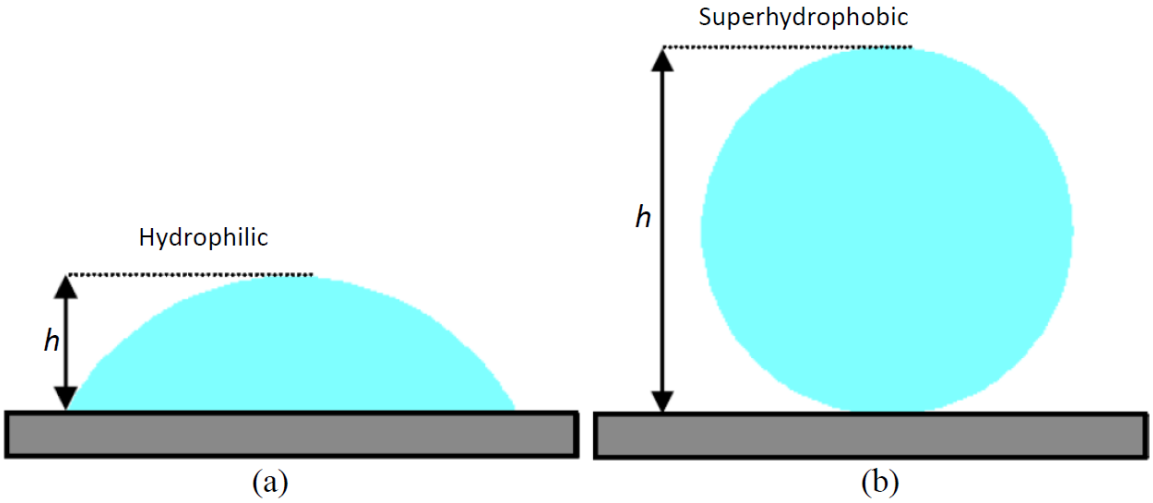

Figure 4.5 Schematic of the heights of sessile droplets on (a) hydrophilic and (b) superhydrophobic substrates

Table 4.1 describes the heights of the droplets in the range between 10 - 200 μm while settling on the hydrophilic and superhydrophobic substrates. The differences between the droplets heights for each substrate are significant for the cloud-sized droplets as they are comparable to the droplets' sizes. Such heights affects the average value of the velocity, u, on the droplet at a given free stream velocity, U_∞.

Droplet initial Diameter (μm)	Height on Superhydrophobic Surface (μm)	Height on Hydrophilic Surface (μm)
10	8.9	6.4
20	17.8	12.8
25	26.7	16
30	35.6	19.2
40	35.6	25.6
50	44.5	32
80	71.2	51.2
100	89	64
115	102.4	73.6
150	133.5	96
200	178	128

Table 4.1 Heights of sessile droplets on the different substrates

In general, the critical velocity increases as the droplet size decreases. This is demonstrated in the $U_{\infty \mathrm{crit}}$ [114] which emphasize that as the volume of a droplet decrease, the critical air velocity needed for incipient of motion increases. This is illustrated in equation 4.1 as follows;

$$U_{\infty \mathrm{crit}} = \sqrt{\frac{2kL_b\gamma(\cos\theta_{\min} - \cos\theta_{\max})}{\rho A C_D}} \qquad 4.1$$

where C_D represents the drag coefficient and k is a factor that accounts for droplets contact line distribution (i.e. continuous change). Both C_D and k depend on the droplet shape change. Such a change is a function of the surface wettability through the contact angles, θ_{min} and θ_{max}. In addition, the critical velocity depends on the degree of adhesion a droplet has on the different substrates. This is because water droplets on the SHS show the lowest $(L_b/A)^{1/2}$ as a result of the surface nature, which forces the drop to bead up leading to both decreased adhesion and increased drag. Such a combination leads to lower critical free stream air velocities when compared to other surfaces.

The snap shots illustrated in Figure 4.6 describe the main droplet shedding parameters that affect the value of $U_{\infty crit}$ on a 20 µm sessile droplet. Generally, as previously described in Chapter 1, these are the shedding angles θ_{min} and θ_{max}, the contact line length, L_b, and the height, h. As demonstrated a larger L_b is attained by the droplet on the hydrophilic substrate, Figure 4.6(a). This leads to higher adhesion force for the droplet and more deformation before and during being shed. In addition due to the small h (i.e. small values of C_D and A in equation 4.1), the drag force on the droplet is reduced which makes it more difficult to shed by requiring a much larger $U_{\infty crit}$. On the other hand, the superhydrophobic surface enables droplets rolling with minimum deformation experienced, as a result of a small L_b and a large h, see Figure 4.6 (b).

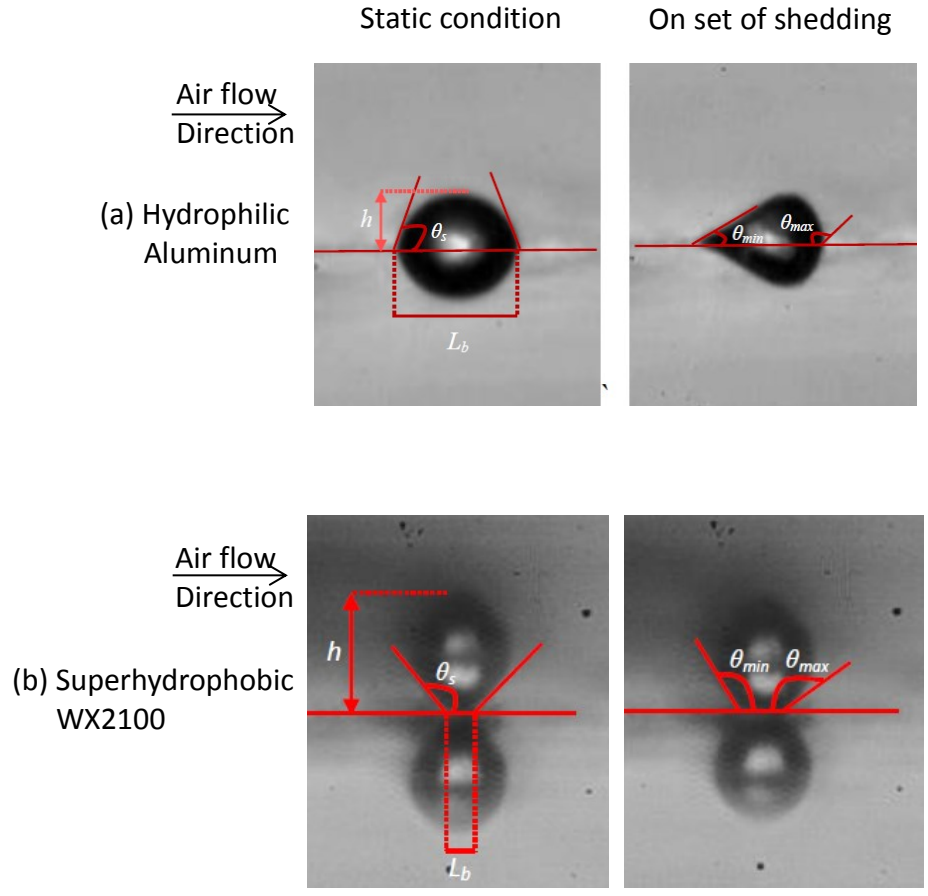

Figure 4.6 Adhesion parameters for the shedding of a 20 µm droplet on the (a) hydrophilic and (b) superhydrophobic substrates

After quantifying the droplets shedding parameters on the two different substrates, it is shown that for each droplet size, as $L_b(cos\theta_{min} - cos\theta_{max})$ decreases, subsequently does the required free stream velocity for droplet shedding. This indicates that a surface with a higher mobility i.e. lower adhesion, allows drops to shed much easier. Accordingly shedding on the SHS is much easier. Note that the usage of the factor $L_b(cos\theta_{min} - cos\theta_{max})$ is recommended in order to measure the shedding of different droplets on various substrates. This is due to the fact that the CAH obtained by calculating the difference between θ_{min} and θ_{max} is different from those found using the advancing and receding contact angles obtained earlier by the quasi-static volume changing method, see Table 4.2. The θ_{min} and θ_{max} give a better prediction for the shedding process. This is validated by comparing the $U_{\infty crit}$ values obtained from the shedding angles and the quasi-static angles to the actual experimental values especially for the SHS. Finally, for cloud-sized droplets that have higher surface-to-volume ratio, the term $(L_b/A)^{1/2}$ has greater effect on their shedding than on larger millimeter-sized droplets.

Substrate type/ Measurement Types	Maximum/advancing contact angles	Minimum/receding contact angles	$(\theta_{max} - \theta_{min})$/ CAH
Hydrophilic (75°±2°)/ Shedding(airflow)			
Droplet size < 100 μm	120° ± 3°	30° ± 3°	90°
Droplet size > 150 μm	115° ± 3°	55° ± 3°	60°
Quasi-static	92° ± 3°	52° ± 3°	40°
SHS (160°±2°)/ Shedding(airflow)			
Droplet size < 100 μm	169° ± 3°	119° ± 3°	50°
Droplet size > 150 μm	167° ± 3°	137° ± 3°	30°
Quasi-static	165° ± 3°	157° ± 3°	8°

Table 4.2 Comparison of maximum and minimum shedding contact angles for airflow and advancing and receding contact angles performed by the quasi-static method for the hydrophilic and the superhydrophobic substrates

The results illustrated in Table 4.2 show that a higher CAH is obtained for droplet that are less than 100 μm in size. This is especially true for the SHS shedding results, where high relative roughness values exist. The cloud-sized droplets are not pinned to the SHS as they attain a large static contact angle (i.e. high repellency). However they suffer from low mobility while settling on the SHS. This is due to the high SHS average surface roughness, where a large portion of the cloud-sized droplet is in contact with such roughness. This is especially true when compared to larger (submillimeter and millimeter-sized) droplets which acquire smaller CAH. Accordingly this demonstrates the difficulty encountered to shed cloud-sized droplets where higher deformation of the droplet occurs. The free stream incipient velocities results described in the following sections will further illustrate such difficulty through quantifying the $U_{\infty \mathrm{crit}}$ for the different droplets sizes.

4.2 Incipient of motion

Analysis for the droplets incipient of motion on implemented substrates was conducted. The current dedicated shedding experimental setup described in details in Chapter 2, allowed for automation, repeatability and increased accuracy of the obtained results. All experimental parameters for droplets dispensing, visualization and shedding were fixed in order to obtain high quality images and a wide viewing window to observe droplets shedding.

Examples of the results obtained for the shedding of a 20 μm droplet on the hydrophilic and the superhydrophobic surfaces are illustrated in Figures 4.7 and 4.8, respectively. Figure 4.7 (a) illustrates the initial position of the droplet as it settles on the hydrophilic aluminum substrate. After 2 ms, the air starts flowing and the droplet begins to deform, see Figure 4.7 (b). As the sessile droplet wets the hydrophilic surface, it needs a high shedding velocity in order to overcome the strong adhesion forces, and start moving the droplet. Accordingly, the droplet deformation continues further for 2 ms then it starts to move, Figure 4.7 (c). It then takes approximately 2 ms for the 20 μm droplet to slide over the aluminum substrate while showing a high CAH, see Figure 4.7 (d). This was contrary to the observations for shedding of the 20 μm on the SHS. The sessile droplet, Figure 4.8 (a), experiences minor deformation, Figure 4.8 (b), as its adhesion forces are much less than for the hydrophilic surface. It then starts to shed 1ms after the air flow starts, Figure 4.8 (c) and rolls over the surface in approximately 1 ms with a small CAH, see Figure 4.8 (d). Additional shedding images of the 20 μm droplet are illustrated in Appendix F.

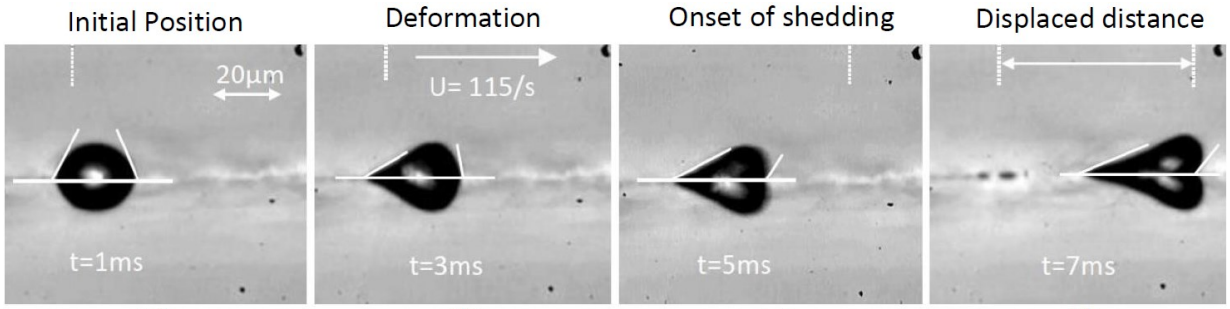

Figure 4.7 Shedding of a 20 µm water droplet on the hydrophilic surface

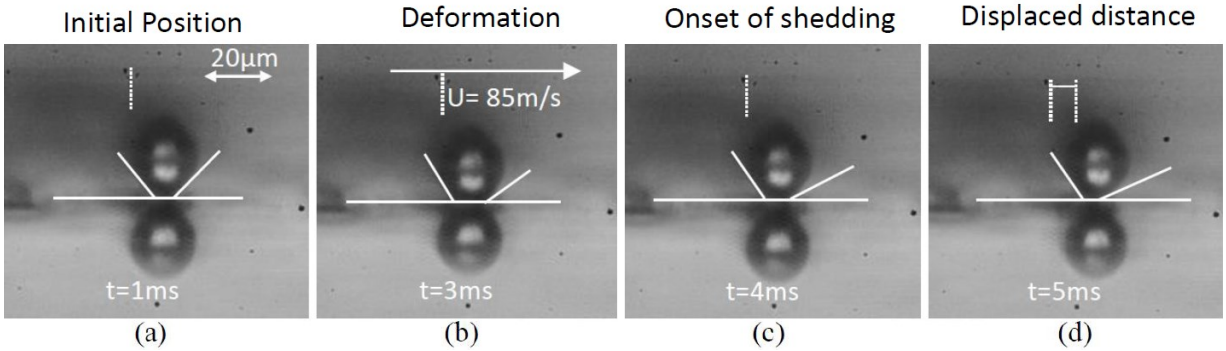

Figure 4.8 Shedding of a 20 µm water droplet on the superhydrophobic surface

The critical air free stream velocities are plotted in Figure 4.9 against the droplet diameter for the entire microdroplets size ranges, i.e. 10 – 200 µm, on various substrates. In general, the smaller the droplet size the higher free stream incipient velocity needed for its shedding. This is due to the higher surface-to-volume ratio of the small droplets in contact with the substrate. Moreover, the tiny droplet size forces it to be buried deep inside the boundary layer very close to the substrate. As a result it is more difficult to reach, requiring a higher free stream velocity to be shed from the substrate. In addition, it is easier to shed a droplet settling over a SHS than when lying on top of a hydrophilic substrate. This can be explained to result from the smaller contact line (i.e. smaller L_b) for the droplet on the SHS. Also, the height of the droplets on SHS is larger when compared to hydrophilic substrates because they tend to bead up, instead of spreading, due to the difference in substrates' wettability.

The results from Milne and Amirfazli [114] for droplets sizes between 1 – 5.8 mm are also added to the figure. These are extrapolated to smaller droplet sizes in order to be compared to the results from the current study. As demonstrated on the figure, such extrapolations do not yield the correct free stream velocities needed for the incipient of motion of the smaller droplets.

Accordingly, the results of sub-millimeter and millimeter-sized droplets cannot be used in order to obtain the incipient velocities for smaller cloud-sized droplets.

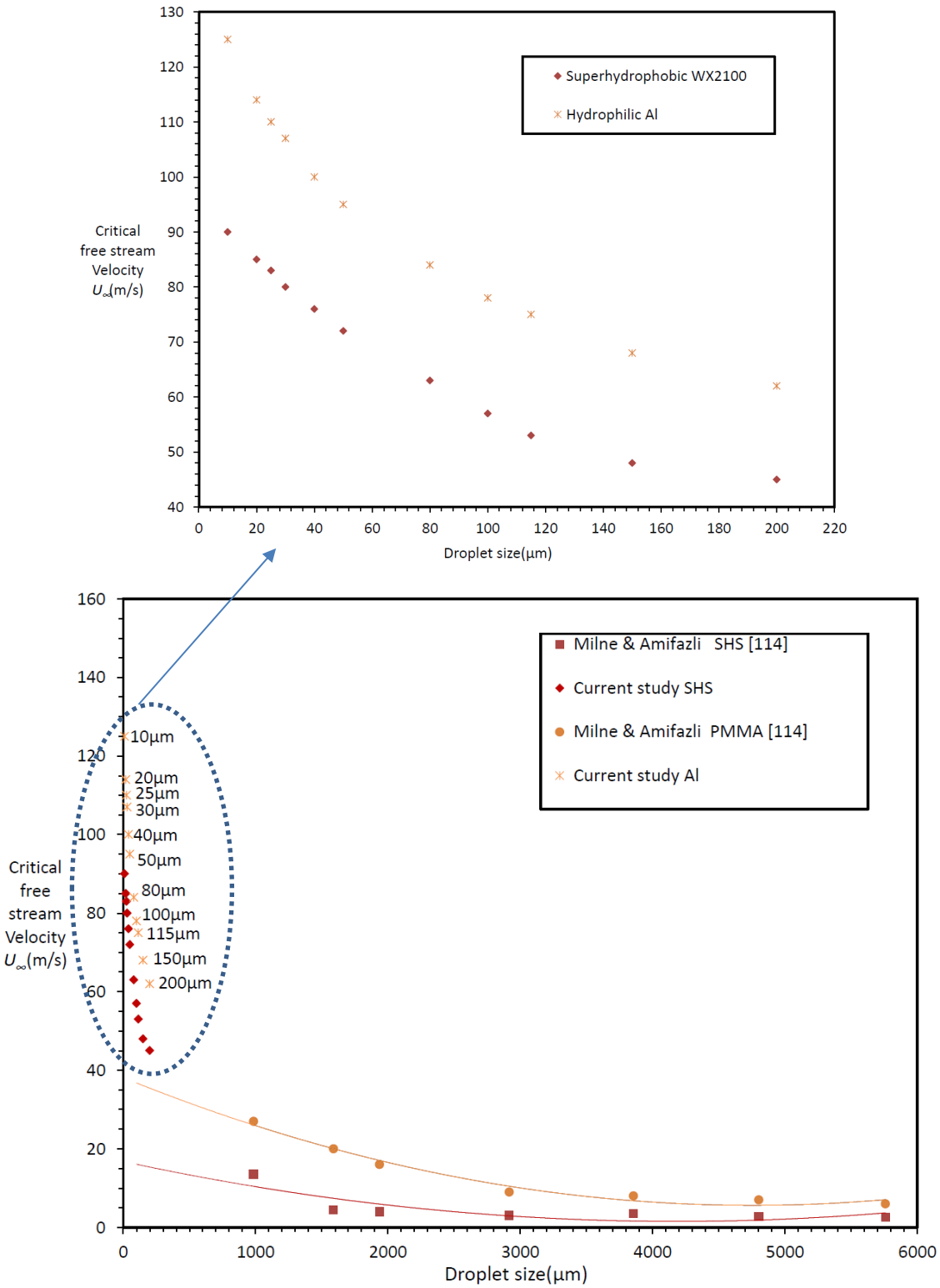

Figure 4.9 Critical free stream velocities for incipient motion vs. droplet size on substrates with various wettabilitties

It is important to note that the main differences between the current analysis and the work done by Milne and Amirfazli [114] stems from the fact that cloud-sized droplets are always entirely inside the boundary layer. As the boundary layer thickness ranges approximately between 400 - 600 μm for the range of free stream velocities needed for incipient of motion. Such a boundary layer thickness is based on the numerical analysis, described in Appendix C, using OpenFOAM 2.1.1. As mentioned earlier, the boundary layer thickness numerical result was considered more accurate than the Blasius rough theoretical estimation. Such estimation yielded an approximate maximum boundary thickness of 200 μm.

By comparing the current study's droplets sizes', (i.e. the droplets' equivalent heights while settling on the different substrates), to the boundary layer thickness, it could be deduced that those droplets are not exposed to the free stream velocities. Instead they only encounter the velocities inside the boundary layer, *u*. On the other hand, for Milne and Amirfazli [114], the droplets' heights were approximately between 0.9 - 2.5 times the boundary layer height. Therefore a large portion of their tested droplets were exposed to the free stream velocity. Accordingly, further analyses were conducted to describe the velocities inside the boundary layer, *u*, which corresponds to each incipient free stream velocity. This is performed for the entire droplets sizes on the hydrophilic and superhydrophobic substrates and illustrated in Figure 4.10. Interestingly, these velocities resemble more the values that were extrapolated from the results of Milne and Amirfazli [114] to describe similar sized droplets. This emphasize on the importance of measuring the velocities on the droplets, inside the boundary layer, and not just the free stream velocities that are responsible for the incipient of motion.

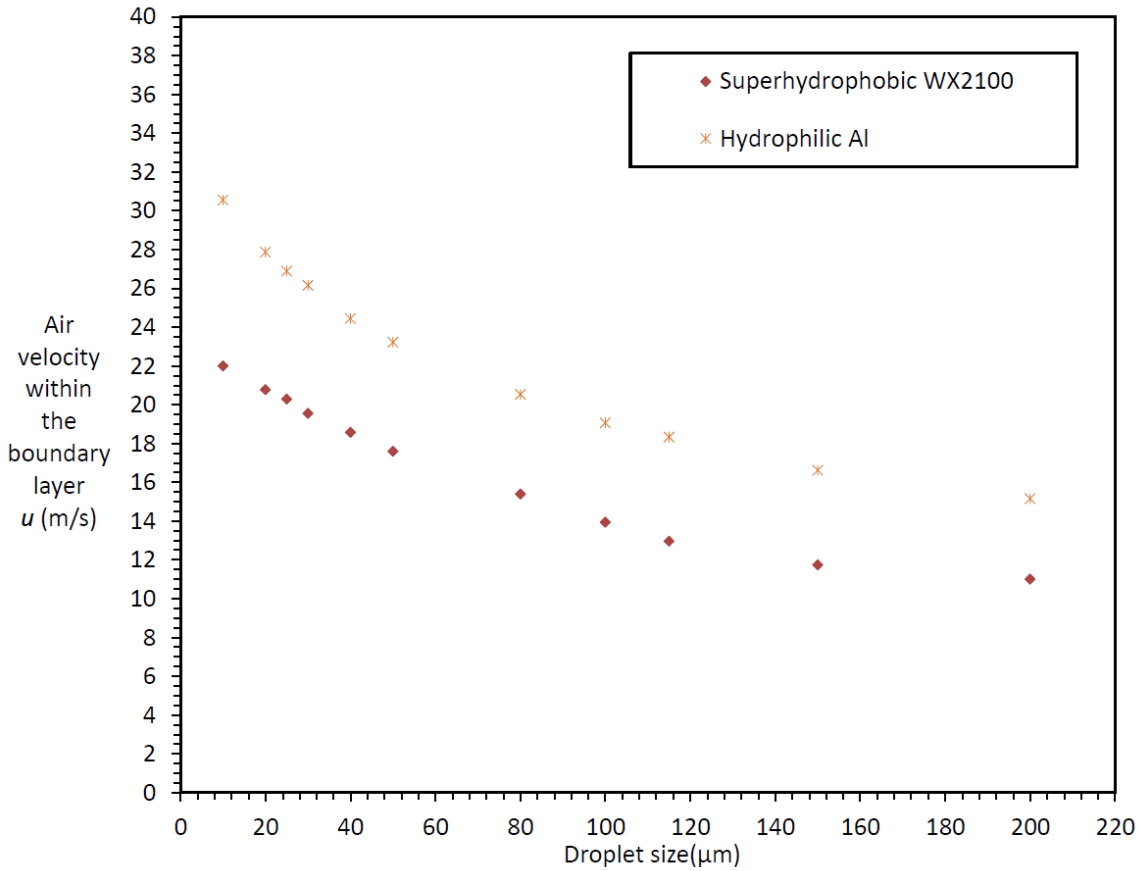

Figure 4.10 Air velocity inside the boundary layer vs. droplet size on substrates with various wettabilities

4.3 Solidification and shedding

All the previously illustrated experimental results were obtained while keeping the temperature of the substrates and the surrounding air at room temperature, i.e. 20 - 22 °C. The substrate temperature is controlled using the Peltier Plate and IR sensor, whereas the surrounding air temperature is controlled by the vortex cooler and compartment temperature sensor as discussed in details in Chapter 2, section 2.7. Generally increased pinning is observed upon the impact of droplets on different substrates at sub-zero temperatures.

In order to investigate the effect of substrate temperature on the velocity required for the incipient of motion, the substrate and surrounding temperatures were dropped down to several degrees below zero, i.e. – 7 °C. The effect of such temperature drop on the incipient velocity on hydrophilic and superhydrophobic substrates is described in Figure 4.11.

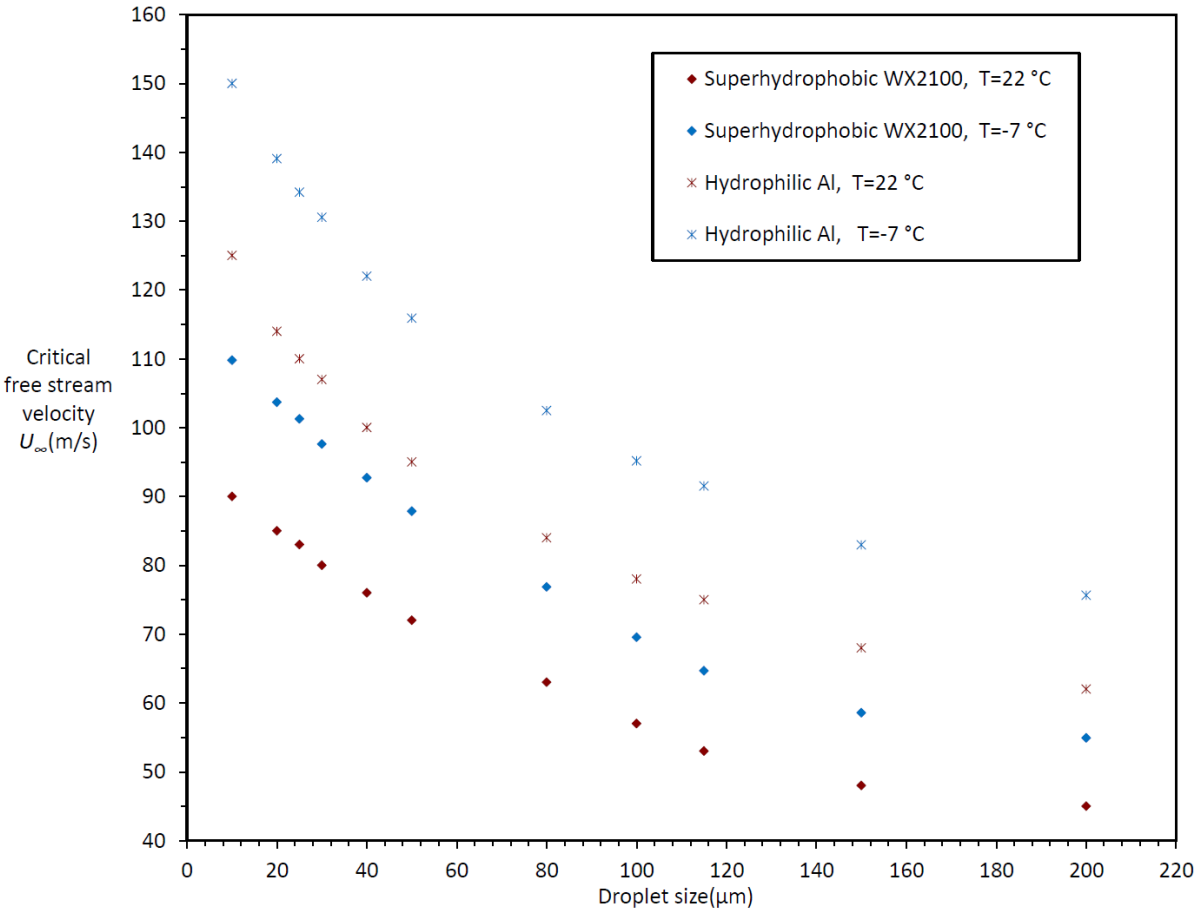

Figure 4.11 Critical free stream velocities for incipient motion vs. droplet size on different substrates at room and sub-zero temperatures

In general, the critical velocity for the incipient of motion increases as the temperature decreases. This is depicted to an increase in both the shedding CAH and contact length, L_b, as temperature decreases. The droplet impacting the substrate at a sub-zero temperature (i.e. – 7 °C) spreads to a maximum value then pins and fails to recoil. This is in contrast to the spreading and recoiling encountered earlier at room temperature. As a result a higher adhesion force is found for the droplet on the different substrates at lower temperatures. Consequently, this demonstrates the difficulty to shed droplets away from different exposed surfaces in flight sub-zero conditions.

Similar to previous analysis the velocities inside the boundary layer, u, which corresponds to each incipient free stream velocity at room and sub-zero temperatures, are analyzed. This is illustrated in Figure 4.12 again for the entire droplets sizes on the two different substrates.

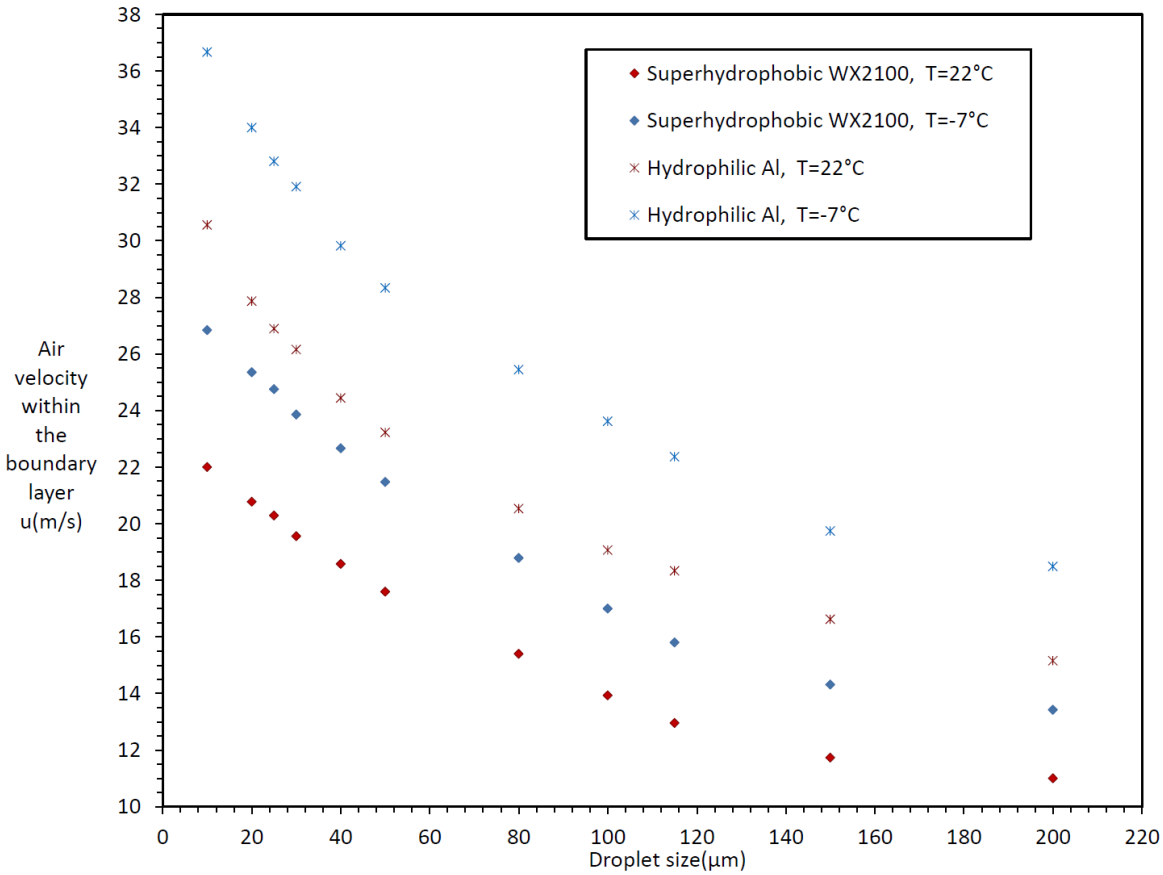

Figure 4.12 Air velocities inside the boundary layer vs. droplet size on different substrates at room and sub-zero temperatures

Chapter 5

Summary, Conclusions and Future Work

This chapter summarizes the analysis performed, explains the conclusions obtained, discusses the work contributions and states few suggestions for future followers.

5.1 Summary

This study is aimed at assessing the effect of substrate wettability, especially surface roughness, on the impact and shedding of cloud-sized, i.e. smaller than 100 μm, water droplets. The majority of work in the literature has been dedicated to the understanding of millimetre or sub-millimetre droplets impacting and/or shedding on either hydrophilic or superhydrophobic substrates. This was mainly due to the experimental feasibility of these large-sized droplets. The current study includes the following aspects:

1. Designing and manufacturing a dedicated experimental setup to study the impact and shedding of microdroplets at controlled environmental conditions. This rig has five major components; a microdroplet generator, a high speed camera with additional magnification and lighting, a slit nozzle for shedding by air flow, a vortex cooler to control the surrounding air temperature, and a Peltier Plate to control substrate temperature down to – 25 °C.
2. Implementing two types of surfaces in order to study the effect of wettability on the impact and shedding of cloud-sized droplets. These include; aluminum that is the standard aerospace building material and aluminum coated with a superhydrophobic spray. The surfaces attain different wettabilitties (with corresponding surfaces roughness), degrees of mobility and water repellency.

5.2 Conclusions

The objectives of this work, as outlined in Chapter 1, are to study the behavior of cloud-sized droplets with respect to impact and shedding and compare their results with sub-millimetre and millimetre-sized droplets. The goals achieved and conclusions made regarding these objectives are summarized as follows:

Droplet impact

In this part of the study several parameters such as oscillation height, maximum spreading diameter, contact time and restitution coefficient were obtained. The impact experiments were conducted at low Weber numbers for the entire range of droplet sizes between 10 - 2500 μm, where surface tension forces dominate the deformation, (i.e. in the capillary regime).

1. The oscillations of the small (cloud-sized) and large (sub-millimeter) droplets were obtained. This was done by comparing the impact of 20 and 200 μm droplets, We = 0.7, on the hydrophilic substrate. Results show that the 20 μm droplet has much less oscillations when compared to the 200 μm droplet due to its higher surface-to-volume ratio. In addition, an apparent lower retraction behavior for the 20 μm droplet exists. This is mainly due to the dominant effect of droplet impingement encountered by the 20 μm droplet compared to that of 200 μm droplet with a volume ratio of 10^{-3}.
2. The dimensionless analysis of normalized maximum spreading diameter, (i.e. D_{max}/D_o) against We number illustrates the difference in droplets behavior on the various substrates. D_{max}/D_o shows a slight change, with an average value of 1.36, for all the droplet sizes on the hydrophilic substrate. On the other hand, for the SHS, the value of D_{max}/D_o increases from 1.23 for the 10 μm droplets to 1.39 for the 2500 μm droplets. The surface roughness scale, which is comparable to the size of the cloud-sized droplets, is considered the main reason for such observed variation on the superhydrophobic substrate. It reduces the cloud-sized droplets spreading and increases their viscous dissipation during impact. Accordingly, the maximum spreading of the cloud-sized droplets on the SHS is much lower than for the hydrophilic smooth substrates. Finally, the roughness has lower effect on the large millimeter-sized droplets which are few orders of magnitude larger than the surface roughness.

3. Bouncing on superhydrophobic surfaces was studied for the entire droplets range between 10 - 2500 μm through the droplets contact time and restitution coefficient. The droplets contact time shows negligible dependence on their impact velocity. Instead, it is controlled by the droplets' diameters. The contact time is relatively increased for droplets diameters less than 100 μm. This is shown by the deviation made from the expected linear relation that can be obtained by extrapolating the results of large sub-millimeter and millimeter-sized droplets. Hence, the cloud-sized relatively larger surface contact with the surface roughness increases their contact time. Furthermore, the restitution coefficient for cloud-sized droplets is considerably small compared to submillimeter and millimeter sized droplets. It varies between 0.28 - 0.65 for droplets less than 100 μm, while for large millimeter-sized it is approximately 0.9 ± 0.02. This sharp decrease in the restitution coefficient for cloud-sized droplets is due to their inability to completely spread or recoil on the superhydrophobic surface as a result of surface roughness. In addition, the relative increase in the microdroplets contact time increases their energy dissipation. This again leads to a reduction in the restitution coefficient value by reducing the rebounding velocity. The decreasing trend obtained for the restitution coefficient against the relative roughness demonstrates that cloud-sized droplets of the order $R_a/D_o \geq 0.07$ are the most affected by surface roughness.

Droplet shedding

In this part of the study, the free stream velocities needed for incipient of motion for different droplets' sizes (i.e. 10 - 200 μm) on different substrates with various wettabilitties were examined. This was done for substrates' temperatures at 20 °C and – 7 °C with the surrounding air at room and sub-zero temperatures, respectively.

4. In general, the smaller a sessile droplet, the higher the incipient velocity that is required to shed it. The high surface-to-volume ratio of the cloud-sized droplet ensures that a relatively larger portion of its surface is in contact with the substrates. This yields a large adhesion force to the substrates. In addition, the tiny droplets' sizes force them to sit very close to the substrate surface. Accordingly, they are not subjected to the free stream velocity, U_∞. Instead, they encounter smaller velocities that depend upon the velocity

distribution inside the boundary layer, u. As a result, higher free stream velocities are needed to reach the incipient of motion of the cloud-sized droplets.

5. It is much easier to shed droplets resting on the SHS than on the hydrophilic substrate. This is mainly due to the higher adhesion and lower drag forces on the hydrophilic surfaces when compared to the SHS. The adhesion is caused by the spreading of droplets on the hydrophilic surface that yields a much larger contact line than the SHS. In contrary, the droplets are forced to bead out, (i.e. holding their shape), while being sessile on the SHS. This makes a larger portion of their frontal area subjected to the shedding velocities and hence increases the drag forces, compared to when sitting on the hydrophilic substrates.
6. Unlike sub-millimeter and millimeter-sized droplets, the cloud-sized droplets lack mobility while settling on the superhydrophobic surface. This is apparent from the relatively large CAH that those microdroplets show upon shedding. Such a large CAH increases the microdroplet adhesion. Hence the $U_{\infty \mathrm{crit}}$ required for shedding is also increased.
7. The critical air velocity that is required for droplet shedding increases when the substrate temperature decreases below freezing point, as a result of ice formation. This is due to the increase in droplet's adhesion that is caused by the increase in the CAH and contact line, L_b, as the substrate temperature drops.

5.3 Contributions

The current work serves as a building block to improve the understanding of cloud-sized droplets impingement and sliding on different substrates. The provided experimental test rig can be utilized to further investigate several parameters regarding cloud-sized droplets. For example, the behavior perceived by droplets spray inside an icing wind-tunnel can be better comprehended by analyzing fundamentally the performance of a single microdroplet under icing and flying conditions. The current obtained results can also be utilized for the improvement of several industrial applications such as painting, spray coating, ink-jet printing, spray cooling, anti-icing and de-icing, to name a few.

1. The maximum droplet spreading to roughness relation on the various substrates can be used to better comprehend and improve the coating or ink-jet printing processes research

analysis done in [3-5, 9, 38, 47, 48, 65]. In these cases, the roughness of used substrates and the droplet size can be manipulated to control the quality of produced outcome where researches on droplet surface interactions [81, 89] play an important role. In addition an extension to the curve given by Clanet *et al*. [101] for spreading over superhydrophobic surfaces can be achieved by providing experimental results for spreading below $We = 2$.

2. The implications made for the restitution coefficient are vital for different applications. For example it pinpoints that a cloud-sized droplet might not bounce away completely from the SHS. Instead, it can eventually settle closer to its initial impact position. This is hazardous especially if the droplet is surrounded by an environment that allows it to solidify on top of the surface. This could create a snow ball effect for the next impacting droplet, where the primary droplet made the surface lose its hydrophobicity by forming a cushion for the coalesce droplets. If this phenomenon occurred at a wing of an airplane, the mechanical carburetor, or an electrical device of an exposed structure, then it might lead to a catastrophe. Removal of these impinged droplets requires heating the structure or shedding by a continuous air bleed. This consumes a considerable amount of energy in the de-icing process. As a result alteration and improvement of anti-icing and de-icing processes explained earlier in plenty of researches [11-13, 25, 26, 75, 79], can be achieved.

5.4 Future work

Should the reader be interested in future experimentation and study of impact, shedding and solidification of cloud-sized droplets, there are a variety of suggestions that can be made. Few of which are reviewed as follows;

1. The next step would be repeating the conducted experiments with different liquids for generality of the obtained results, and in order to determine the effect of viscosity on the processes of impact and shedding. An investigation to find a correlation factor that can allow the results of various liquids to coincide on top of one another can be made. Such a study may be interesting for different applications such as combustion, surfaces' coloring, electroplating and many more.
2. The possibility of a sessile cloud-sized droplet to be removed by a shedded incoming droplet at different offsets should also be investigated. The understanding of this

mechanism is important since it contributes to understanding the degree of repellency of superhydrophobic surfaces, particularly when exposed to cloud-sized droplets. This can represent real life situations where cloud droplets adhered to the surface of an exposed structure, could be removed by other droplets through shedding.

3. There is a future potential for studies on the evaporation time of microdroplets, while being sessile on different substrate. The effects of substrate temperatures and wettability, (i.e. contact angle and roughness), can then be quantified and related to the droplet evaporation rate.
4. The solidification front of microdroplets can be examined. This help in understanding the exact mechanism occurring during solidification. The experiments are designed to visualize the solidification line as it propagates through the droplet. This can then be numerically simulated to characterize such propagation with different parameters such as substrate wettability and droplet size. Finally the numerical model can be validated using the experimental results in order to obtain the most accurate model to represent the solidification process.
5. The bubble entrapment upon the impact of microdroplets on different substrates can also be investigated. In the literature few studies report the appearance of such bubbles and others argues differently that they do not exist. Further analysis need to be done on the appearance of those bubbles in cloud-sized droplets upon their impact on different substrates with various impact velocities. This can lead to better control over such bubble formation and hence improve industrial applications that depend upon droplets impact for their outcome, such as spray coating, ink-jet printing, painting and many more.
6. improvement The effect of the method implemented to produce the SHS on the obtained results can be vital to pinpoint the most suitable technique to work with microdroplets. For the current study, as mentioned earlier, a mirror finish aluminum substrate was coated by a superhydrophobic WX2100 commercial spray. Such coating was not fragile but showed the tendency to be removed with any little scratch. The produced uncontrolled surface roughness, with valleys and peaks on the surface, is generally encountered in real life situations of exposed structures. However, different approaches can be followed in order to produce superhydrophobic substrates. Commercial coatings (Hydrobead, Waterbeader...etc.), different spraying methods, chemical treatment and surface etching,

see Figure 5.1, to name a few. Therefore it is a potential investigation to apply few of those methods and compare the results obtained for the cloud-sized droplets on each.

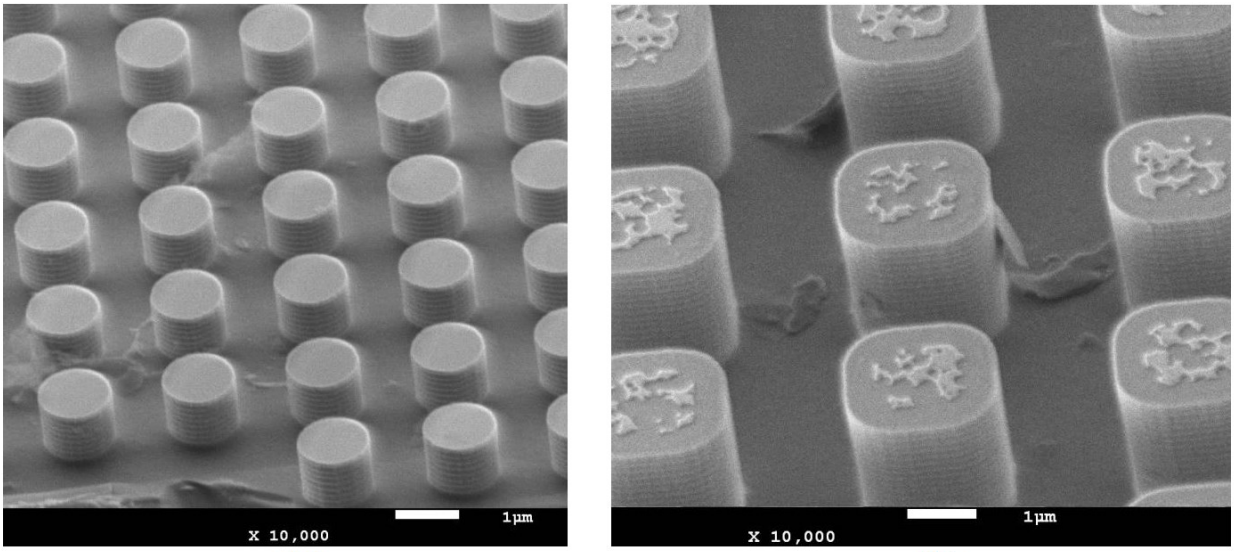

(a) (b)

Figure 5.1 Micro etched substrates with diameter, height and pitch of (a) 1 x 1 x 1 µm and (b) 2 x2 x 2 µm with θ_s = 155 ° - 165 ° and CAH = 8 °- 10 °

References

[1] A. M. Worthington, "The Splash of a Drop," London: Society for promoting Christian knowledge, 1895.

[2] A. M. Worthington, “A Study of Splashes," Davenport: The Royal Naval Engineering College, 1908.

[3] R. Danzebrink and A. M. Aegerter, “Deposition of Micropatterned Coating Using an Ink-Jet Technique,” *Journal of Thin Solid Films*, vol. 351, no. 1–2, p. 115–118, 1999.

[4] J. Stringer and B. Derby, "Limits to the Feature Size and Resolution in Ink Jet Printing," *Journal of the European Ceramic Society*, vol. 29, no. 5, p. 913–918, 2009.

[5] D. Soltman and V. Subramanian, "Inkjet-Printed Line Morphologies and Temperature Control of the Coffee Ring Effect," *Langmuir,* vol. 24, no. 5, p. 2224–2231, 2008.

[6] R. Dhiman and S. Chandra, "Freezing-Induced Splashing During Impact of Molten Metal Droplets with High Weber Numbers," *International Journal of Heat and Mass Transfer*, vol. 48, no. 25-26, p. 5625–5638, 2005.

[7] S. Shakeri and S. Chandra, "Splashing of Molten Tin Droplets on a Rough Steel Surface," *International Journal of Heat and Mass Transfer*, vol. 45, no. 23, p. 4561–4575, 2002.

[8] K. Davood and T. Cameron, "Spray Impact onto Flat and Rigid Walls: Empirical Characterization and Modelling," *International Journal of Multiphase Flow,* vol. 33, no. 5, p. 525–544, 2007.

[9] D. Sivakumar and H. Nishiyama, "Spreading and Solidification of a Molten Metal Droplet Impinging on a Heated Surface," International Journal of Heat and Mass Transfer, vol. 47, no. 19-20, p. 4469–4478, September 2004.

[10] S. D. Aziz and S. Chandra, "Impact, Recoiling and Splashing of Molten Metal Droplets," *International Journal of Heat and Mass transfer,* vol. 43, no. 16, p. 2841-2857, 15 August 2000.

[11] L. Mishchenko, B. Hatton, V. Bahadur, J. A. Taylor, T. Krupenkin, and J. Aizenberg, "Design of Ice-free Nanostructured Surfaces Based on Repulsion of Impacting Water Droplets, " *ACS Nano*, vol. 4, no. 12, p. 7699–7707, 9 November 2010.

[12] S. K. Thomas, R. P. Cassoni and C. D. MacArthur, "Aircraft Anti-Icing and De-Icing Techniques and Modeling," *Journal of Aircraft*, vol. 33, no. 5, p. 841-854, September-October 1996.

[13] G. Fortin and J. Perron, "Wind Turbine Icing and De-Icing," *47th AIAA Aerospace Sciences Meeting including The New Horizons Forum and Aerospace Exposition,* 5-8 January 2009.

[14] A. Turhan, S. Kim, M. Hatzell, and M. M. Mench, "Impact of Channel Wall Hydrophobicity on Through-Plane Water Distribution and Flooding Behavior in a Polymer Electrolyte Fuel Cell," *Electrochimica Acta* , vol. 55, no. 8, p. 2734–2745, March 2010.

[15] J. G. Carton, V. Lawlor, A. G. Olabi, C. Hochenauer and G. Zauner, "Water Droplet Accumulation and Motion in PEM (Proton Exchange Membrane) Fuel Cell Mini-Channels," *Journal of Energy*, vol. 39, no. 1, p. 63–73, March 2012.

[16] A. Theodorakakos, T. Ous, M. Gavaises, J. M. Nouri, N. Nikolopoulos and H. Yanagihara, "Dynamics of Water Droplets Detached from Porous Surfaces of Relevance to PEM Fuel Cells," *Journal of Colloid and Interface Science*, vol. 300, no. 2, p. 673–687, 15 August 2006.

[17] R. Li, N. Ashgriz, S. Chandra, J. R. Andrews and S. Drappel, "Coalescing of Two Droplets Impacting a Solid Surface," *Experiments in Fluids*, vol. 48, no. 6, p. 1025-1035, 2010.

[18] R. Li, N. Ashgriz, S. Chandra, J. R. Andrews and J. Williams, "Drawback During Deposition of Overlapping Molten Wax Droplets," *Journal of Manufacturing Science and Engineering*, vol. 130, no. 4, p. 1011-1021, 15 July 2008.

[19] R., Rioboo, M. Marengo and C. Tropea, "Time Evolution of Liquid Drop Impact onto Solid Dry Surfaces," *Experiments in Fluids*, vol. 33, p. 112-124, 2002.

[20] B. Blocken and J. Carmeliet, "On the Errors Associated with the Use of Hourly Data in Wind-Driven Rain Calculations on Building Facades," *Atmospheric Environment*, vol. 41, no. 11, p. 2335-2343, April 2007.

[21] M. Fernández-Raga, R. Fraile, J. J. Keizer, M. E. V. Teijeiro, A. Castro, C. Palencia, A. I. Calvo, J. Koenders and R. L. Marques, "The Kinetic Energy of Rain Measured With an Optical Disdrometer: An Application to Splash Erosion," *Atmospheric Research*, vol. 96, no. 2–3, p. 225–240, May 2010.

[22] J. L. Laforte, M. A. Allaire and J. Laflamme, "State-of-the-Art on Power Line De-Icing," *Atmospheric Research*, vol. 46, no. 1–2, p. 143–158, 1998.

[23] W. Shaohua, "Influence of Ice Accretions on Mechanical and Electrical Performance of Overhead Transmission Lines," *Journal of Electrical and Mechanical Engineering*, 2010.

[24] C. Ryerson, "Ice protection of offshore platforms," *Cold Regions Science and Technology*, vol. 65, p. 97–110, 2011.

[25] M. Farzaneh and C. Ryerson, "Anti-Icing and De-Icing Techniques," *Cold Regions Science and Technology*, vol. 65, no. 1, p. 1–4, 2011.

[26] O. Parent and A. Ilinca, "Anti-Icing and De-Icing Techniques for Wind Turbines: Critical Review," *Cold Regions Science and Technology*, vol. 65, no. 1, p. 88–96, 2011.

[27] N. Dalili, A. Edrisy and R. Carriveau, "A Review of Surface Engineering Issues Critical to Wind Turbine Performance," *Renewable and Sustainable Energy Reviews*, vol. 13, no. 2, p. 428–438, 2009.

[28] N. Czernkovich, "Understand In-Flight Icing," Transport Canada Aviation Safety Seminar, 2004.

[29] J. Hallett, G. A. Isaac, M. Politovich, D. L. Marcotte, A. Reehorst and C. Ryerson, "Aliance Icing Research Study II (AIRS II)," Science Plan, 2003.

[30] The Globe and Mail. (2012, Dec. 28) Nunavut plane crash that killed baby the result of hard landing: report [Online]. Available: http://www.theglobeandmail.com/news/national/nunavut-plane-crash-that-killed-baby-the-result-of-hard-landing-report/article6771725/

[31] W. Barthlott, "Scanning Electron Microscopy of the Epidermal Surface in Plants," *Clarendon Press:Oxford*, vol. 41, p. 69–94, 1990.

[32] W. Barthlott and C. Neinhuis, "Purity of the Sacred Lotus, or Escape from Contamination in Biological Surfaces," *Planta*, vol. 202, p. 1-8, 1997.

[33] W. Barthlott, "Self-Cleaning Surfaces of Objects and Process for Producing Same". US Patent 6660363 B1, 9 December 2003.

[34] X. Gao and L. Jiang, "Water-Repellent Legs of Water Striders," *Biophysics*, vol. 432, p. 36, 4 November 2004.

[35] H. J. Ensikat, P. Ditsche-Kuru, C. Neinhuis, and W. Barthlott, "Superhydrophobicity in Perfection: the Outstanding Properties of the Lotus Leaf," *Beilstein Journal Nanotechnology*, vol. 2, p. 152–161, 2011.

[36] 10Wallpaper.com. (2011, July 17) Drops of Water Rolling on a Lotus Leaf Wallpaper. [Online]. Available: http://www.10wallpaper.com/down/drops_of_water_on_a_lotus_leaf_wallpaper_1366x768_wallpaper.html [March 2, 2015].

[37] A. Solga, Z. Cerman, B. F. Striffler, M. Spaeth, and W. Barthlott, "The Dream of Staying Clean: Lotus and Biomimetic Surfaces," *Bioinspiration & Biomimetics*, vol. 2, p. 126–134, 2007.

[38] S. Kulinich and M. Farzaneh, "On Ice-Releasing Properties of Rough Hydrophobic Coatings," *Cold Region Science Technology*, vol. 65, no. 1, p. 60–64, 2011.

[39] R. Menini, Z. Ghalmi and M. Farzaneh, "Highly Resistant Icephobic Coatings on Aluminum Alloys," *Cold Region Science Technology*, vol. 65, no. 1, p. 65–69, 2011.

[40] V. Petrenko, C. Sullivan, V. Kozlyuk, F. Petrenko and V. Veerasamy, "Pulse Electro-Thermal De-Icer (PETD)," *Cold Region Science Technology*, vol. 65, no. 1, p. 70–78, 2011.

[41] A. Marmur, "The Lotus Effect: Superhydrophobicity and Metastability," *Langmuir*, vol. 20, no. 9, p. 3517–3519, 2004.

[42] M. K. Politovich, "AIRCRAFT ICING," *Elsevier Science Ltd*, p. 68-75, 2003.

[43] A. Dolatabadi, *et al., et al.* "Ice phobic Evaluation of Superhydrophobic Coatings for Aircraft Icing Protection," Montreal, PWC, 2010.

[44] M. B. Lesser and J. E. Field, "The Impact of Compressible Liquids," *Annual Review of Fluid Mechanics*, vol. 15, p. 97–122, 1983.

[45] M. Rein, "Phenomena of Liquid Drop Impact on Solid and Liquid Surfaces," *Fluid Dynamics Research*, vol. 12, no. 2, p. 61–93, 1993.

[46] A. Yarin, "Drop Impact Dynamics: Splashing, Spreading, Receding, Bouncing…," *Annual Review of Fluid Mechanics*, vol. 38, p. 159–192, January 2006.

[47] D. B. Van Dam and C. Le Clerc, "Experimental Study of the Impact of an Inkjet Printed Droplet on a Solid Substrate," *Physics of Fluids*, vol. 16, p. 3403–3414, 2004.

[48] H. Dong, W. W. Carr, D. G. Bucknall and J. F. Morris, "Temporally-Resolved Inkjet Impaction on Surfaces," AIChE Journal, vol. 53, p. 2606–2617, 2007.

[49] T. Young, "An Essay on the Cohesion of Fluids," Philosophical Transactions of the Royal Society of London, vol. 95, p. 65-87, 1805.

[50] F. Cebeci, Z. Wu, L. Zhai, R. Cohen and M. Rubner, “Nanoporosity- Driven Superhydrophilicity: a Means to Create Multifunctional Antifogging Coatings,” *Langmuir*, vol. 22, no. 6, p. 2856–2862, 2006.

[51] T. Sun, L. Feng, X. Gao, and L. Jiang, “Bioinspired Surfaces with Special Wettability,” Accounts of Chemical Research, vol. 38, p. 644-652, 2005.

[52] N. Verplanck, Y. Coffinier, V. Thomy, and R. Boukherroub, “Wettability Switching Techniques on Superhydrophobic Surfaces,” *Nanoscale Research Letters*, vol. 2, p. 577–596, 2007.

[53] J. Fox and W. Zisman, “The Spreading of Liquids on Low Energy Surfaces. I. polytetrafluoroethylene,” *Journal of Colloid Science*, vol. 5, no. 6, p. 514-531, 1950.

[54] W. Zisman, “Relation of the Equilibrium Contact Angle to Liquid and Solid Constitution”, *Advances in Chemistry Series*, vol. 43, p. 381, 1964.

[55] L. Gao and T. J. McCarthy, “Contact Angle Hysteresis Explained”, *Langmuir*, vol. 22, p. 6234–6237, April 2006.

[56] S. S. Latthe, C. Terashima, K. Nakata and A. Fujishima “Superhydrophobic Surfaces Developed by Mimicking Hierarchical Surface Morphology of Lotus Leaf,” *Journal of Molecules*, vol. 19, p. 4256-4283, 2014.

[57] J. Genzer and K. Efimenko, "Recent Developments in Superhydrophobic Surfaces and their Relevance to Marine Fouling: A review," *Biofouling*, vol. 22, p. 339-360, 2006.

[58] K. Koch and W. Barthlott, "Superhydrophobic and Superhydrophilic Plant Surfaces: an Inspiration for Biomimetic Materials," *Philosophical Transactions of the Royal Society A*, vol. 367, p. 1487-1509, 2009.

[59] J. A. Nychka and M. M. Gentleman, "Implications of Wettability in Biological Materials Science," *Biological and Biomedical Materials*, vol. 62, p. 39-48, 2010.

[60] X. Zhang, F. Shi, J. Niu, Y. Jiang, and Z. Wang, "Superhydrophobic Surfaces: from Structural Control to Functional Application," *Journal of Material Chemistry*, vol. 18, p. 621-633, 2008.

[61] The Biomimicry Institute: AskNature. (November 14, 2008) Surface allows self-cleaning: sacred lotus [Online]. Available: http://www.asknature.org/strategy/ [January 24, 2015].

[62] R. N. Wenzel, “Resistance of Solid Surfaces to Wetting by Water,” *Industrial & Engineering Chemistry*, vol. 28, no. 8, p. 988–994, 1936.

[63] R. N. Wenzel, “Surface Roughness and Contact Angle,” *Journal of Physical Chemistry*, vol. 53, no. 9, p. 1466–1467, 1949.

[64] A. B. D. Cassie and S. Baxter, “Wettability of Porous Surfaces,” *Transaction of the Faraday Society*, vol. 40, p. 546-551, 1944.

[65] D. Quere, “Wetting and Roughness,” *The Annual Review of Material Research*, vol. 38, p. 71-99, 2008.

[66] A. Marmur, "Wetting on Hydrophobic Rough Surfaces: To Be Heterogeneous or Not To Be?," *Langmuir*, vol. 19, no. 20, p. 8343-8348, June 2003.

[67] R. E. Johnson and R. H. Dettre, "Contact Angle, Wettability and Adhesion," *Advanced Chemistry*, vol. 43, p. 112–135, 1964.

[68] A. Milne and A. Amirfazli “The Cassie Equation: How it is Meant to be Used,” *Advances in Colloids and Interface Science*, vol. 170, no. 1–2, p. 48–55, 2012.

[69] M. Callies, Y. Chen, F. Marty, A. Pépin, and D. Quére, “Microfabricated Textured Surfaces for Superhydrophobicity Investigations,” *Microelectronic Engineering*, vol. 78–79, p. 100–105, 2005.

[70] J. B. Lee, H. R. Gwon, S. H. Lee and M. Cho, "Wetting Transition Characteristics on Microstructured Hydrohpobic Surfaces," *Materials Transactions*, vol. 51, no. 9, p. 1709-1711, 2010.

[71] N. A. Patankar, "Transition between Superhydrophobic States on Rough Surfaces," *Langmuir*, vol. 20, no. 17, p. 7097–7102, 2004.

[72] Y. C. Jung and B. Bhushan, "Wetting Transition of Water Droplets on Superhydrophobic Patterned Surfaces," *Scripta Materialia*, vol. 57, no. 12, p. 1057–1060, 2007.

[73] E. Bormashenko, T. Stein, R. Pogreb, and D. Aurbach, “"Petal Effect "on Surfaces Based on Lycopodium: High-Stick Surfaces Demonstrating High Apparent Contact Angles,” *Journal of Physical Chemistry C* , vol. 113, no. 14, p. 5568-5572, 2009.

[74] P. Tsai, R. G. H. Lammertink, M. Wessling, and D. Lohse, "Evaporation-Triggered Wetting Transition for Water Droplets upon Hydrophobic Microstructures," *Physical Review Letters*, vol. 104, no. 11, 18 March 2010.

[75] C. Antonini, M. Innocenti, T. Horn, M. Marengo and A. Amirfazli, "Understanding the Effect of Superhydrophobic Coatings on Energy Reduction in Anti-Icing System," *Cold Region Science Technology*, vol. 67, no. 1-2, p. 58–67, 2011.

[76] A. Alizadeh, M. Yamada, R. Li, W. Shang, S. Otta, S. Zhong, L. Ge, A. Dhinojwala, K.R. Conway, V. Bahadur, A. J. Vinciquerra, B. Stephens, and M. L. Blohm, "Dynamics of Ice Nucleation on Water Repellent Surfaces," *Langmuir*, vol. 28, no. 6, p. 3180–3186, 2012.

[77] D. Li, and Z. Chen, "Experimental Study on Instantaneously Shedding Frozen Water Droplets from Cold Vertical Surface by Ultrasonic Vibration," *Experimental Thermal and Fluid Science*, vol. 53, p. 17-25, 2014.

[78] L. Yin, Q. Xia, J. Xue, S. Yang, Q. Wang and Q. Chen, "In Situ Investigation of Ice Formation on Surfaces with Representative Wettability," *Applied Surface Science*, vol. 256, no. 90, p.6764–6769, 2010.

[79] S. Farhadi, M. Farzaneh and S. A. Kulinich "Anti-Icing Performance of Superhydrophobic Surfaces," *Applied Surface Science*, vol. 257, no. 14, p. 6264-6269, May 2011.

[80] F. Wang, C. Li, Y. Lv, F. Lv and Y. Du "Ice Accretion on Superhydrophobic Aluminum Surfaces Under Low-Temperature Conditions," *Cold Region Science Technology*, vol. 62, no. 1, p.29–33, June 2010.

[81] D. Kannangara, H. Zhang and W. Shen, "Liquid-Paper Interactions During Liquid Drop Impact and Recoil on Paper Surfaces," *Colloids and Surfaces A: Physicochemical and Engineering Aspects*, vol. 280, no. 1–3, p. 203–215, 2006.

[82] S. Sikalo, C. Tropea and E. Ganic, "Dynamic Wetting Angle of a Spreading Droplet," *Experimental Thermal and Fluid Science*, vol. 29, no. 7, p. 795–802, 2005.

[83] D. Roux and J. Cooper-White, "Dynamics of Water Spreading on a Glass Surface," *Journal of Colloid and Interface Science*, vol. 277, no. 2, p. 424–436, 2004.

[84] R. Li, N. Ashgriz and S. Chandra, "Maximum Spread of Droplet on Solid Surface: Low Reynolds and Weber Numbers," *ASME J. Fluids Eng*., vol. 132, no. 6, p. 061302–5, 2010.

[85] H. Marmanis and S.Thoroddsen, "Scaling of the Fingering Pattern of an Impacting Drop," *Physics of Fluids*, vol. 8, p. 1344, 1996.

[86] L. Cheng, "Dynamic Spreading of Drops Impacting onto a Solid Surface," *Ind. Eng. Chem. Process Des. Dev.*, vol. 16, no.2, p. 192-197, 1977.

[87] S. Lunkad, V. Buwa, and K. Nigam, "Numerical Simulations of Drop Impact and Spreading on Horizontal and Inclined Surfaces," *Chemical Engineering Science*, vol. 62, p. 7214–7224, 2007.

[88] H. Mukherjee and J. Abraham, “Investigations of Drop Impact on Dry Walls with a Lattice-Boltzmann Model,” *Journal of Colloid and Interface Science*, vol. 312, p. 341–354, 2007.

[89] S. Chandra, and C. Avedisian, “On the Collision of a Droplet with a Solid Surface,” *Proc. Royal Society of London*, vol. 432, no. 1884, p. 13-41, 1991.

[90] A. Frohn and N. Roth, Dynamics of Droplets, Berlin: Springer, 2000.

[91] M. Rein, Drop–Surface Interactions, Berlin: Springer, 2000.

[92] D. Richard and D. Quére, “Bouncing Water Drops,” *Europhysics Letters*, vol. 50, no. 6, p. 769–775, 2000.

[93] V. L. Roisman, R. Rioboo, and C. Tropea, "Normal Impact of a Liquid Drop on a Dry Surface: Model for Spreading and Receding," *Proc. Royal Society of London A*, vol. 458, p. 1411-1430, 2002.

[94] R. Rioboo, M. Marengo and C. Tropea, “Time Evolution of Liquid Drop Impact onto Solid Dry Surfaces,” *Experiments in Fluids*, vol. 33, p. 112-124, 2001.

[95] R. Rioboo, C. Tropea and M. Mareng, "Outcomes from a Drop Impact on Solid Surfaces," *Atomization and Sprays*, vol. 11, no. 2, 2001.

[96] S. Sikalo, H. D. Wilhelm, I. V. Roisman, S. Jakirlic and C. Tropea, “Dynamic Contact Angle of Spreading Droplets: Experiments and Simulations,” *Physics of Fluids*, vol. 17, p.062103-01 - 062103-13, 2005.

[97] M. Pasandideh-Fard, Y. Qiao, S. Chandra and J. Mostaghimi, "Capillary Effects During Droplet Impact on a Solid Surface," *Physics of Fluids*, vol. 8, no. 3, p. 650, 1996.

[98] E. Chibowski, "Surface Free Energy of a Solid from Contact Angle Hysteresis," *Advances in Colloid and Interface sciences*, vol. 103, no. 2, 25 April 2003.

[99] C. Ukiwe and D. Y. Kwok, "On the Maximum Spreading Diameter of Impacting Droplets on Well-Prepared Solid Surfaces," *Langmuir*, 2005.

[100] D. Vadillo, A. Soucemarianadin, C. Delattre, and D. Roux, "Dynamic Contact Angle Effects onto the Maximum Drop Impact Spreading on Solid Surfaces," *Physics of Fluids,* vol. 21, no. 12, p. 122002-8, 2009.

[101] C. Clanet, C. Beguin, D. Richard and D. Quére, ”Maximal Deformation of an Impacting Drop,” *Journal of Fluid Mechanics*, vol. 517, p. 199-208, September 2004.

[102] P. Tsai, M. Hendrix, R. Dijkstra, L. Shui and D. Lohse, "Microscopic Structure Influencing Macroscopic Splash at High Weber Number," *Soft Matter*, vol. 7, no. 24, p. 11325-11333, 13 September 2011.

[103] L. Chen, Z. Xiao, P.C.H Chan, Y.K. Lee and Z. Li, "A Comparative Study of Droplet Impact Dynamics on a Dual-Scaled Superhydrophobic Surface and Lotus Leaf," *Applied Surface Science*, vol. 257, p. 8857– 8863, 2011.

[104] C. Visser, Y. Tagawa, C. Sun and D. Lohse, "Microdroplet Impact at Very High Velocity," *Soft Matter*, vol.8, no. 41, p. 10732-10737, June 2012.

[105] Y. Tagawa, N. Oudalov, C. Visser, I. Peters, D. van der Meer, C. Sun, A. Prosperetti and D. Lohse, "Highly Focused Supersonic Microjets," *Physical Review X*, vol. 2, no. 3, p.1002-1010, 2012.

[106] C. Visser, P. Frommhold, W. Sander, R. Mettin, D. Lohse, and C. Sun, "Dynamics of High-Speed Micro-Drop Impact: Numerical Simulations and Experiments at Frame-to-Frame Times Below 100ns," *Soft Matter*, vol. 11, no. 9, p. 1708-1722, 2015.

[107] S. H. Davis, "Moving Contact Lines and Rivulet Instabilities Part 1. The static rivulet," *Journal of Fluid Mechanics*, vol. 98, p .225–242, 1980.

[108] S. K. Chen, M. A. Hickner and D. R. Noble, "Simplified Models for Predicting the Onset of Liquid Water Droplet Instability at the Gas Diffusion Layer/Gas Flow Channel Interface," *International Journal of Energy Research*, vol. 29, no. 12, p. 1113–1132, 10 October 2005.

[109] E. C. Kumbur, K. V. Sharp and M. M. Mench, "Liquid Droplet Behavior and Instability in a Polymer Electrolyte Fuel Cell Flow Channel," *Journal of Power Sources*, vol. 161, p.333–345, 2006.

[110] M. Mahé, M. Vignes-Adler and P. M. Adler, "Adhesion of Droplets on a Solid Wall and Detachment by a Shear Flow," *Journal of Colloid and Interface Science*, vol. 126, no. 1, 1998.

[111] F. Y. Zhang, X. G. Yang and C. Y. Wang, "Liquid Water Removal from a Polymer Electrolyte Fuel Cell," *Journal of The Electrochemical Society*, vol. 153, no. 2, p. A225-A232, 2006.

[112] G. Minor, "Experimental Study of Water Droplet Flows in a Model PEM Fuel Cell Gas Microchannel," M.S. thesis, Department of Mechanical Engineering, University of Victoria, Victoria, Canada, 2007.

[113] E. B. White and Schmucker, "A Runback Criterion for Water Drops in a Turbulent Accelerated Boundary Layer," *ASME J. Fluids Eng.*, vol. 130, no. 6, p. 1302-1308, 19 May 2008.

[114] A. J. B. Milne and A. Amirfazli, "Drop Shedding by Shear Flow for Hydrophilic to Superhydrophobic Surfaces," *Langmuir*, vol. 25, no. 24, p. 14155-14164, 2009.

[115] C. Antonini, F. J. Carmona, E. Pierce, M. Marengo and A. Amirfazli, "General Methodology for Evaluating the Adhesion Force of Drops and Bubbles on Solid Surfaces," *Langmuir*, vol. 25, no. 11, p. 6143–6154, 2009.

[116] Schott North America. LLS - LED Light Source. Southbridge, USA, 2009.

[117] MicroFab TECHNOLOGIES. INC: Manuals http://www.microfab.com/manuals. Accessed on 01 - 05 - 2012

[118] Photron, FASTCAM SA1.1 Hardware Manual, Tokyo, Japan: Photron Limited, E0706013518U, 2007.

[119] Navitar: 12X Zoom High Mag. Zoom Lenses http://www.qmt.ch/pdf/Products/Lens_Navitar_12xZoom.pdf. Accessed on 01 - 01 - 2013.

[120] F-Number. [Online] [Cited: July 12, 2012.] http://www.photography.com/articles/basic-concepts/f-number. Accessed on 01 - 01 - 2013.

[121] Nikon Microscopy. Numerical Aperture. [Online] [Cited: July 11, 2012.] http://www.microscopyu.com/articles/formulas/formulasna.html. Accessed on 01 - 11 - 2012.

[122] Navitar: Field of view, "12X Zoom" http://www.navitar.com/pdf/12X_field_of_view_matrices.pdf. Accessed on 01 - 06 - 2012.

[123] MATLAB, "Mathworks," http://www.mathworks.com/help/images/boundary-tracing-in-images.html. Accessed on 05 - 01 - 2012.

[124] LoggerPro " Vernier: LoggerPro" http://www.vernier.com/products/software/lp/ Accessed on 05 - 01 - 2012.

[125] A. F. Stalder, G. Kulik, D. Sage, L. Barbieri and P. Hoffmann, "A Snake Based Approach to Accurate Determination of Both Contact Points and Contact Angles," *Colloids Surfaces A*, vol. 286, p. 92–103, 2006.

[126] A. F. Stalder, T. Melchior, M. Müller, D. Sage, T. Blu and M. Unser, "Low-Bond Axisymmetric Drop Shape Analysis for Surface Tension and Contact Angle Measurements of Sessile Drops," *Colloids and Surfaces A: Physicochemical and Engineering Aspects*, vol. 364, no. 1-3, p. 72-81, 20 July, 2010.

[127] K. Smyth, A. Paxon, H. Kwon, T. Deng and K. Varanasi, "Dynamic Wetting on Superhydrophobic Surfaces: Droplet Impact and Wetting Hysteresis," *Thermal and Thermomechanical Phenomena in Electronic Systems (ITherm)*, 12th IEEE Intersociety Conference, June 2010.

[128] Y. Xia, Z. Ming, J. Da-lin, L. Jian and C. Lan "Transition of Superhydrophobic States on Droplet on Rough Surface," *Journal of Central South University*, vol. 17, p. 554-559, 2010.

[129] M. Farhangi, G. Percival, N. Choudhury and A. Dolatabadi, "Induced Detachment of Coalescing Droplet on Superhydrophobic Surfaces," *Langmuir*, vol. 28, no. 2, p. 1290–1303, December 2012.

[130] L. Yin, L. Zhu, Q. Wang, J. Ding and Q. Chen, "Superhydrophobicity of Natural and Artificial Surfaces Under Controlled Condensation Conditions," *ACS Applied Material Interfaces*, vol. 4, p. 117, 2011.

[131] B. Mockenhaupt, H. J. Ensikat, M. Spaeth and W. Barthlott, "Superhydrophobicity of Biological and Technical Surfaces Under Moisture Condensation: Stability in Relation to Surface Structure," *Langmuir*, vol. 24, no.23, p. 13591–13597, 2008.

[132] D. Richard, C. Clanet and D., Quéré "Contact time of a bouncing drop," *Nature*, vol. 417, p. 811-812, June 2002.

[133] H. Rusche, "Computational Fluid Dynamics of Dispersed Two-Phase Flows at High Phase Fractions," Ph.D. thesis, Imperial College of London, UK, 2002.

[134] S. Kistler, "On Hydrodynamics of Wetting," Berg, J. C., Ed.; Wettability; Marcel Dekker Inc.: New York; pp 311−429, 1993.

Appendix A

Characteristics of produced substrates

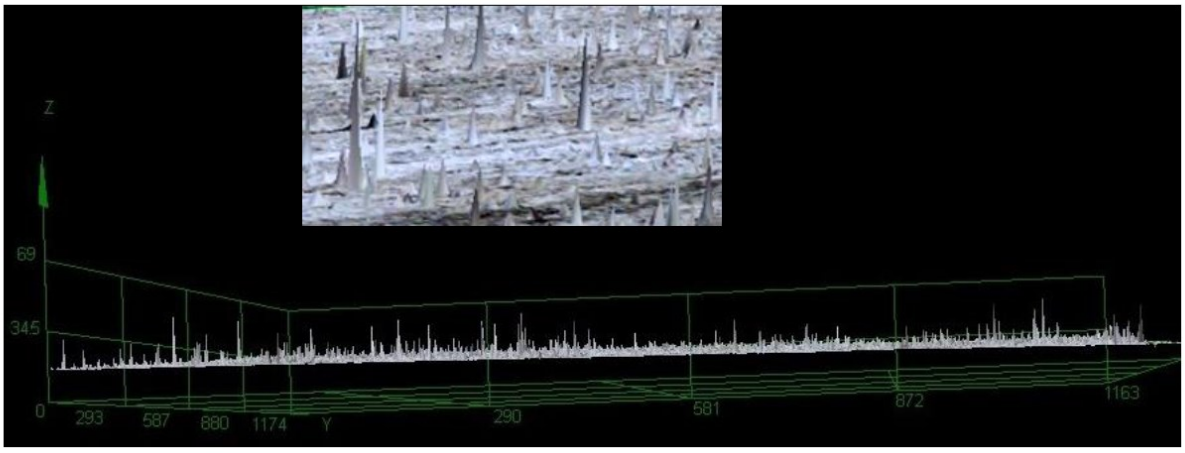

Figure A1 Micrograph images of tested smooth Aluminuim

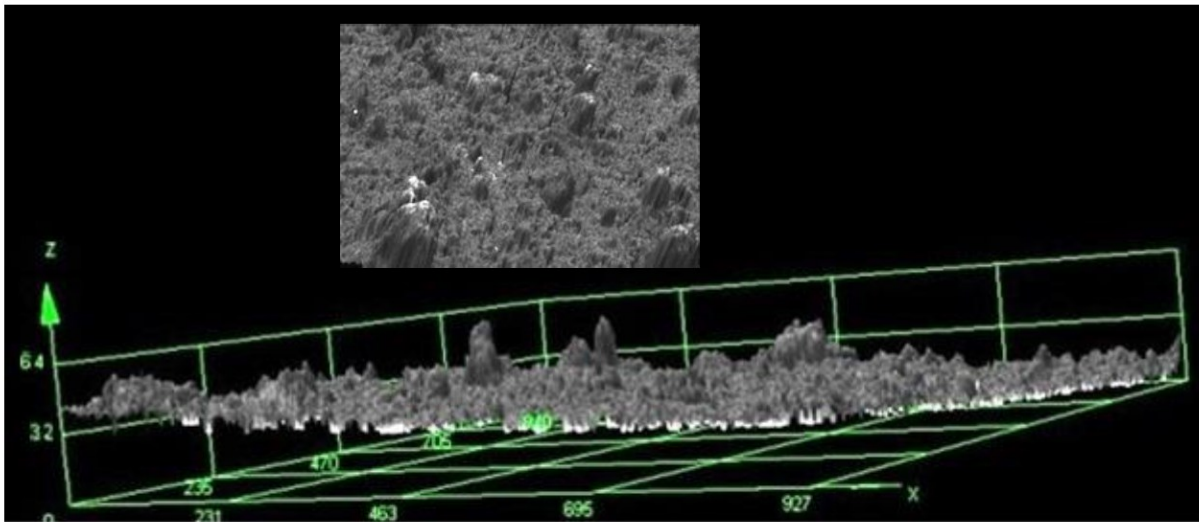

Figure A2 Laser micrograph images of SHS

Figure A3 Image of produced superhydrophobic WX2100 substrates

Appendix B

Nozzle design

The detailed design of the nozzle with its entire configuration is illustrated in the exploded and 3d views explained in the following figures. The nozzle upper part is being placed and fixed using 6 different screws. This is to give additional freedom to change the height of the output slit from a minimum of 2 mm to a maximum of 10 mm.

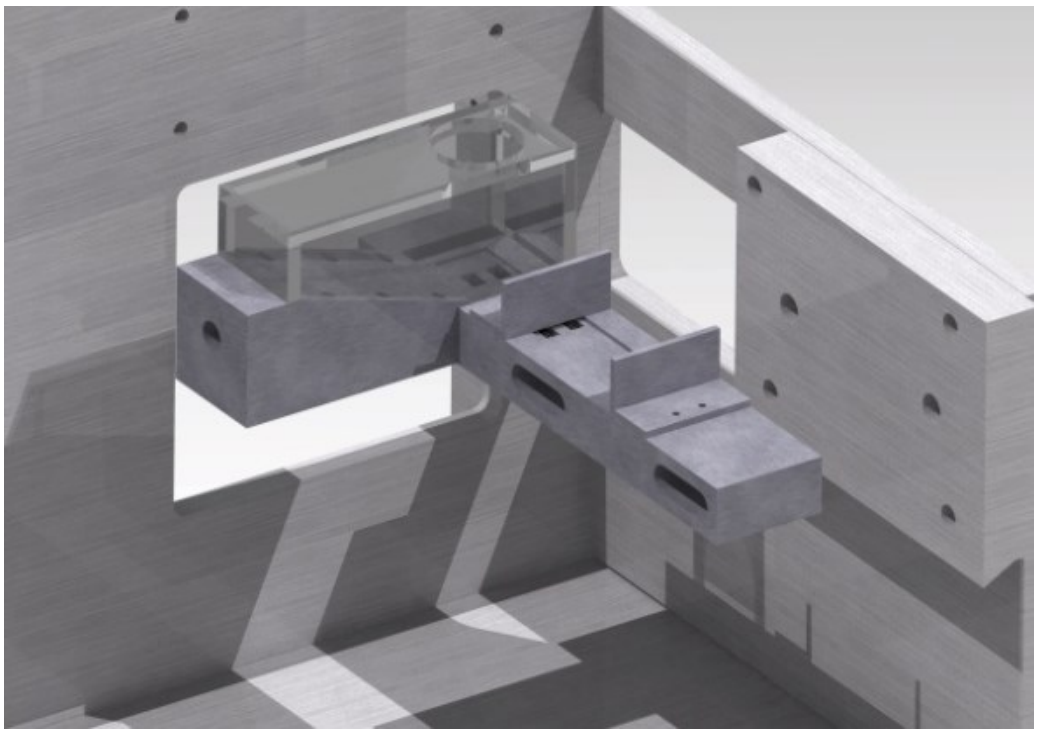

Figure B1 Schematic of the frame used for droplets shedding tests

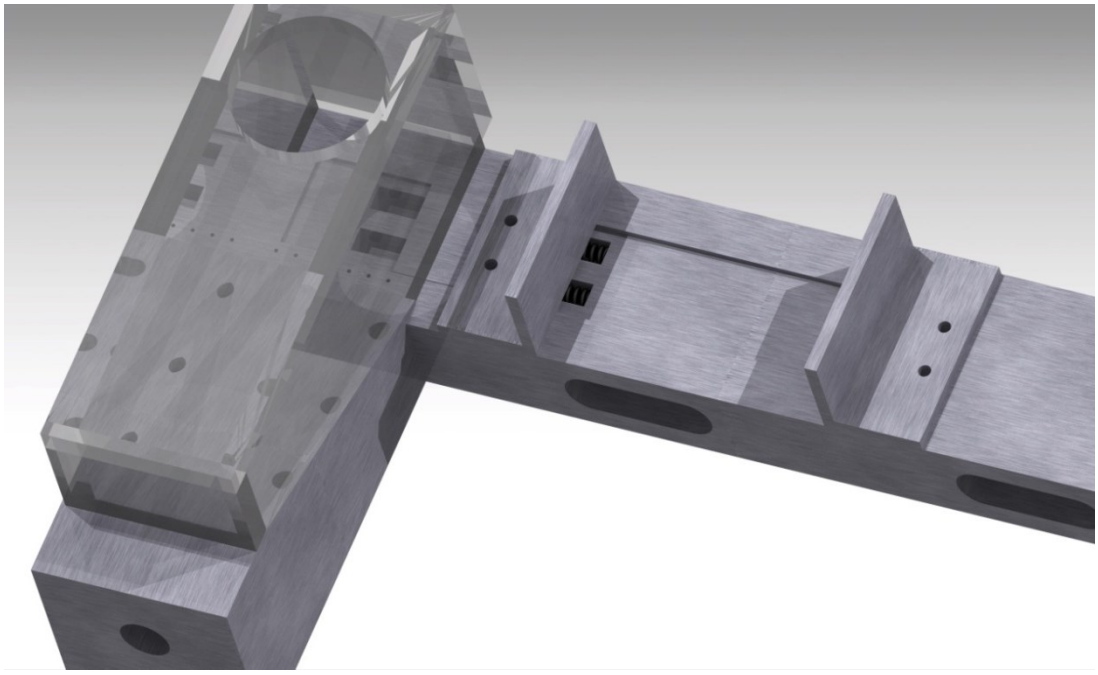

Figure B2 Top view of the enclosed chamber with fixing handle

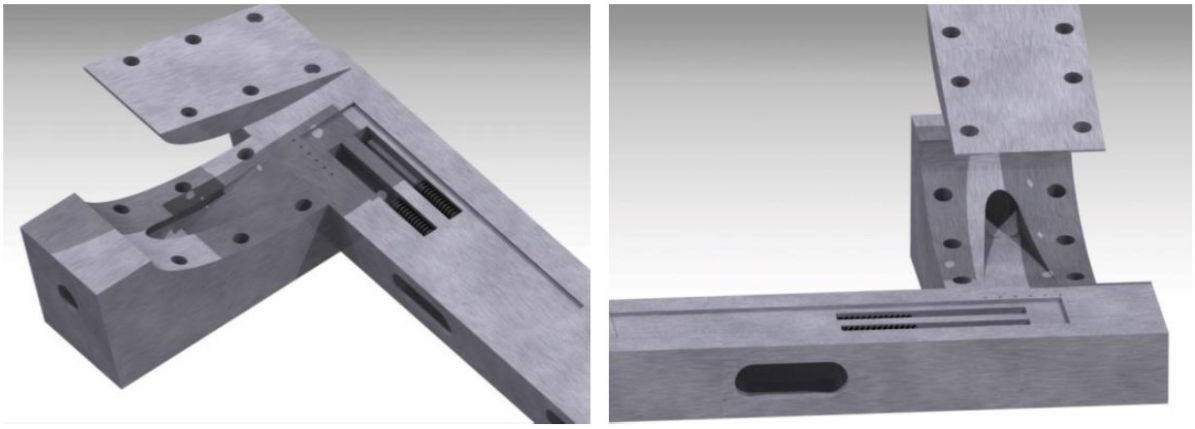

(a) (b)

Figure B3 Designed nozzle upper surface (a) side view and (b) top view

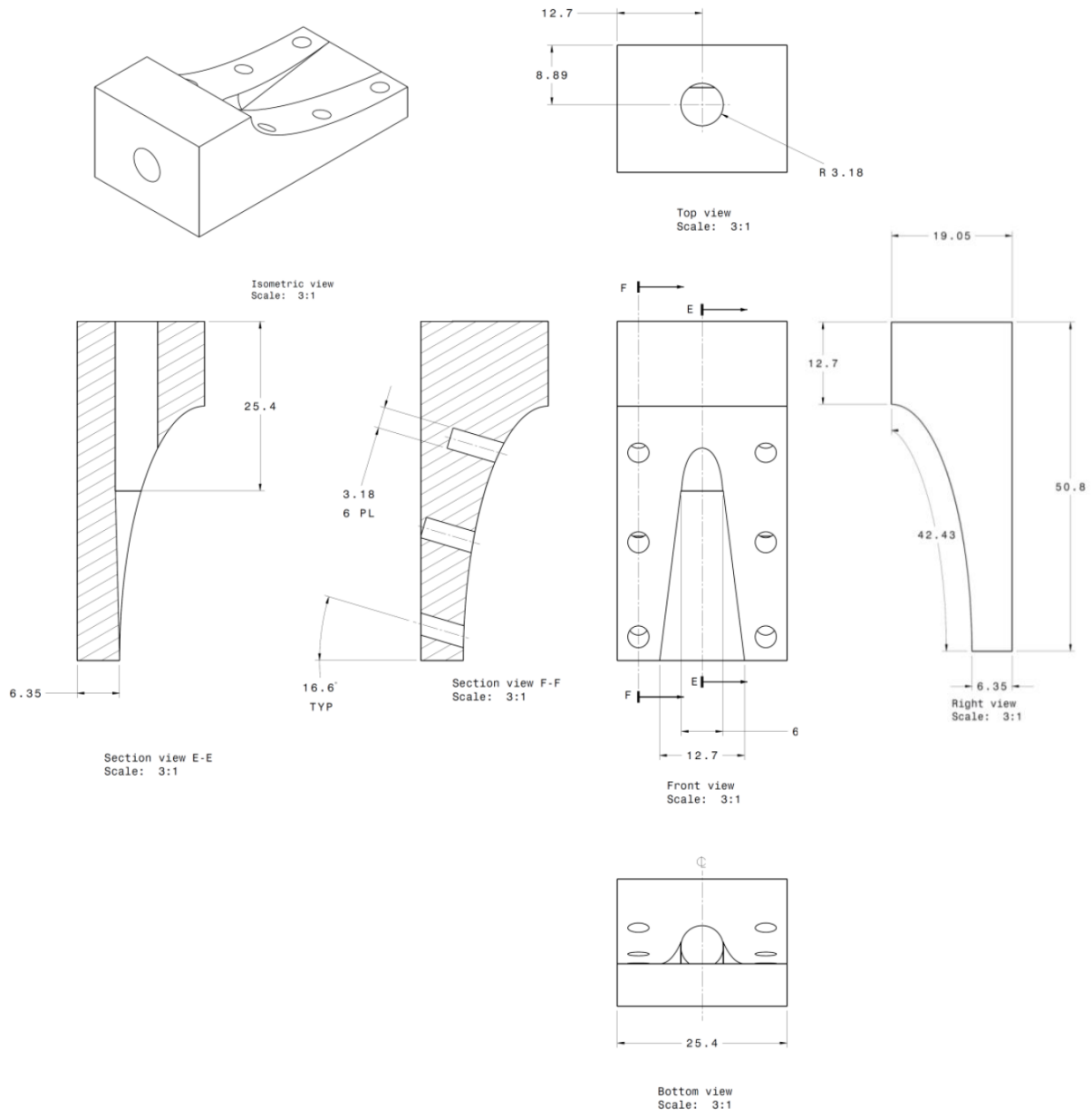

Figure B4 Dimensions of designed nozzle

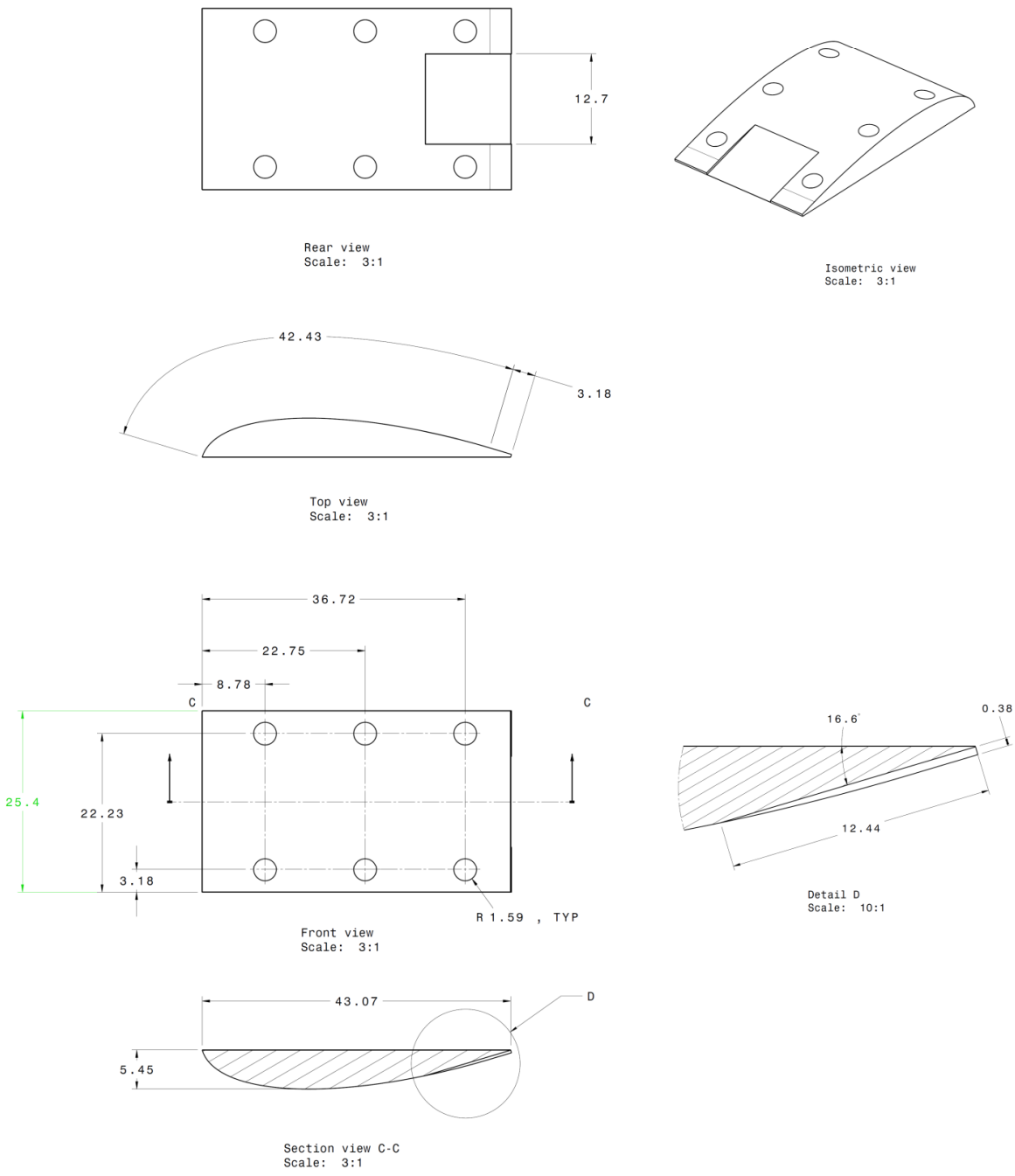

Figure B5 Slit nozzle adjustable cover

Appendix C

Boundary layer numerical analysis (A collaborative analysis by Mr. Mohamed Reza)

Numerical analysis of the boundary layer for various air inlet velocities (up to 150 m/s) was performed, to understand the interaction of air-droplet at the instant of shedding. Simulation was done using an open source C++ toolbox, OpenFOAM 2.1.1. The model successfully matched the Blasius theory. The boundary layer thickness was calculated at different sections. Figure C1 illustrated below describes the associated mesh and the 3D geometrical configuration of the model. For the sake of the computation time, the 3D geometrical features are simplified as a strip along the nozzle.

The simulation is divided into two models. In the first model, the air flow simulation for different air inlet velocities was obtained to determine the air velocity distribution around the region where the droplet is expected to be found. The semi implicit for pressure linked equation in steady flow is used to solve the pressure and velocity as the primitive variables. In the second model, the region where the micro-droplet is located was extracted, and is subjected to the air velocity that was obtained in the first model to calculate drag force and the shedding velocities. In this model, the volume of fluid (VOF), interface tracking method was used to solve the two phase problem, impact and shedding of the droplet. Finally in order to increase the convergence time, the mesh composed of hexahedral elements is made with adaptive mesh refinement at the interfacial cells.

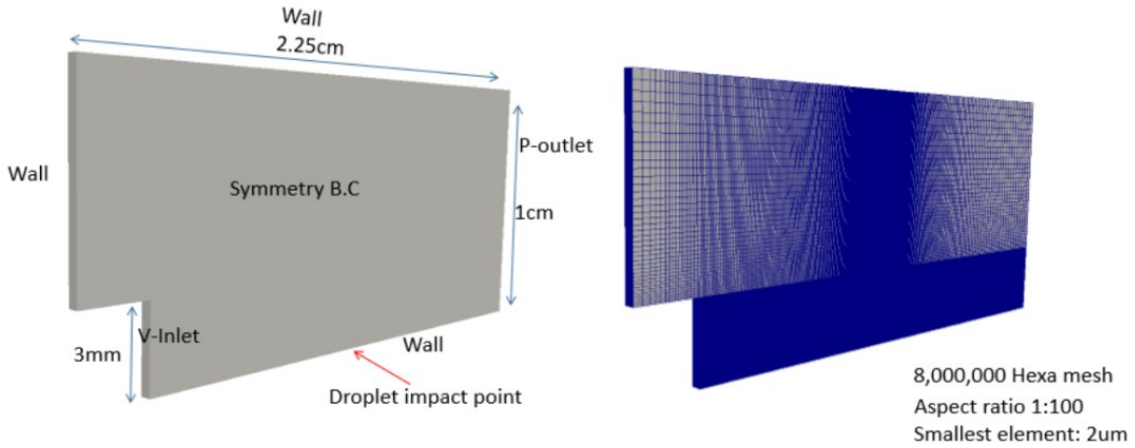

Figure C1 A schematic of the 3D mesh used for analysis of the flow inside the boundary layer

Appendix D

Vortex cooler design

The Vortex cooling principle implements a vortex where the fluid (air) rotates around a certain axis in a tornado like structure. This is created by the vortex tube using compressed air that separates it into hot and cold airstreams. The compressed air flow passes through a designed vortex generation chamber that starts the rotation of the air stream. It then exits this chamber at approximately 1000000 rpm, being forced along the inner wall of the vortex tube. A small portion of the air exits through a needle control valve as hot exhaust. The cooled air flows back through the center of the vortex generation part and exits through the opposite side as cold air into the needed chamber.

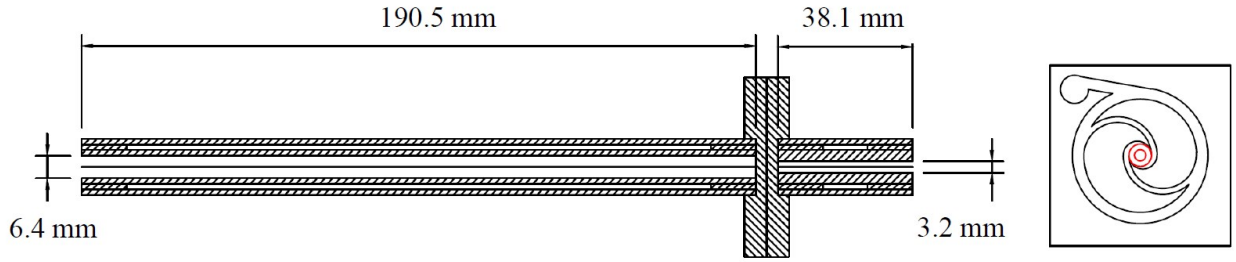

(a)

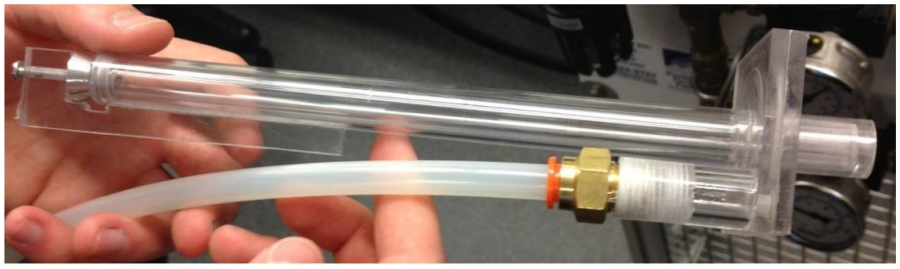

(b)

Figure D1 Designed vortex cooler (a) schematic drawing (b) actual picture

Appendix E

Tables of impact tests velocities and Weber and Reynolds numbers

Impact Velocity *(m/s)*	*We for* D_o *=10μm*	*We for* D_o *=20μm*	*We for* D_o *=25μm*	*We for* D_o *=40μm*	*We for* D_o *=50μm*	*We for* D_o *=80μm*	*We for* D_o *=100μm*	*We for* D_o *=150μm*	*We for* D_o *=200μm*	*We for* D_o *=250μm*	*We for* D_o *=300μm*	*We for* D_o *=400μm*	*We for* D_o *=500μm*	*We for* D_o *=2500μm*
0.2	0.01	0.01	0.01	0.02	0.03	0.04	0.05	0.08	0.11	0.14	0.16	0.22	0.27	1.37
0.3	0.01	0.02	0.03	0.05	0.06	0.10	0.12	0.19	0.25	0.31	0.37	0.49	0.62	3.08
0.4	0.02	0.04	0.05	0.09	0.11	0.18	0.22	0.33	0.44	0.55	0.66	0.88	1.10	5.48
0.45	0.03	0.06	0.07	0.11	0.14	0.22	0.28	0.42	0.56	0.69	0.83	1.11	1.39	6.94
0.5	0.03	0.07	0.09	0.14	0.17	0.27	0.34	0.51	0.69	0.86	1.03	1.37	1.71	8.57
0.6	0.05	0.10	0.12	0.20	0.25	0.39	0.49	0.74	0.99	1.23	1.48	1.97	2.47	12.34
0.7	0.07	0.13	0.17	0.27	0.34	0.54	0.67	1.01	1.34	1.68	2.01	2.69	3.36	16.79
0.8	0.09	0.18	0.22	0.35	0.44	0.70	0.88	1.32	1.75	2.19	2.63	3.51	4.39	21.93
0.9	0.11	0.22	0.28	0.44	0.56	0.89	1.11	1.67	2.22	2.78	3.33	4.44	5.55	27.75
1	0.14	0.27	0.34	0.55	0.69	1.10	1.37	2.06	2.74	3.43	4.11	5.48	6.85	34.26
1.1	0.17	0.33	0.41	0.66	0.83	1.33	1.66	2.49	3.32	4.15	4.98	6.63	8.29	41.46
1.2	0.20	0.39	0.49	0.79	0.99	1.58	1.97	2.96	3.95	4.93	5.92	7.89	9.87	49.34
1.3	0.23	0.46	0.58	0.93	1.16	1.85	2.32	3.47	4.63	5.79	6.95	9.27	11.58	57.91
1.4	0.27	0.54	0.67	1.07	1.34	2.15	2.69	4.03	5.37	6.72	8.06	10.75	13.43	67.16
1.5	0.31	0.62	0.77	1.23	1.54	2.47	3.08	4.63	6.17	7.71	9.25	12.34	15.42	77.09
1.6	0.35	0.70	0.88	1.40	1.75	2.81	3.51	5.26	7.02	8.77	10.53	14.03	17.54	87.72
1.7	0.40	0.79	0.99	1.58	1.98	3.17	3.96	5.94	7.92	9.90	11.88	15.84	19.80	99.02
1.8	0.44	0.89	1.11	1.78	2.22	3.55	4.44	6.66	8.88	11.10	13.32	17.76	22.20	111.02
1.9	0.49	0.99	1.24	1.98	2.47	3.96	4.95	7.42	9.90	12.37	14.84	19.79	24.74	123.69
2	0.55	1.10	1.37	2.19	2.74	4.39	5.48	8.22	10.96	13.71	16.45	21.93	27.41	137.06
2.1	0.60	1.21	1.51	2.42	3.02	4.84	6.04	9.07	12.09	15.11	18.13	24.18	30.22	151.11
2.2	0.66	1.33	1.66	2.65	3.32	5.31	6.63	9.95	13.27	16.58	19.90	26.53	33.17	165.84
2.3	0.73	1.45	1.81	2.90	3.63	5.80	7.25	10.88	14.50	18.13	21.75	29.00	36.25	181.26
2.4	0.79	1.58	1.97	3.16	3.95	6.32	7.89	11.84	15.79	19.74	23.68	31.58	39.47	197.36
2.5	0.86	1.71	2.14	3.43	4.28	6.85	8.57	12.85	17.13	21.42	25.70	34.26	42.83	214.15

Table E1 All tested impact velocities, droplets sizes and corresponding Weber numbers

Impact Velocity *(m/s)*	*Re for D_O =10μm*	*Re for D_O =20μm*	*Re for D_O =25μm*	*Re for D_O =40μm*	*Re for D_O =50μm*	*Re for D_O =80μm*	*Re for D_O =100μm*	*Re for D_O =150μm*	*Re for D_O =200μm*	*Re for D_O =250μm*	*Re for D_O =300μm*	*Re for D_O =400μm*	*Re for D_O =500μm*	*Re for D_O =2500μm*
0.20	2.00	3.99	4.99	7.98	9.98	15.96	19.96	29.93	39.91	49.89	59.87	79.82	99.78	498.89
0.30	2.99	5.99	7.48	11.97	14.97	23.95	29.93	44.90	59.87	74.83	89.80	119.73	149.67	748.33
0.40	3.99	7.98	9.98	15.96	19.96	31.93	39.91	59.87	79.82	99.78	119.73	159.64	199.55	997.77
0.45	4.49	8.98	11.22	17.96	22.45	35.92	44.90	67.35	89.80	112.25	134.70	179.60	224.50	1122.50
0.50	4.99	9.98	12.47	19.96	24.94	39.91	49.89	74.83	99.78	124.72	149.67	199.55	249.44	1247.22
0.60	5.99	11.97	14.97	23.95	29.93	47.89	59.87	89.80	119.73	149.67	179.60	239.47	299.33	1496.66
0.70	6.98	13.97	17.46	27.94	34.92	55.88	69.84	104.77	139.69	174.61	209.53	279.38	349.22	1746.10
0.80	7.98	15.96	19.96	31.93	39.91	63.86	79.82	119.73	159.64	199.55	239.47	319.29	399.11	1995.55
0.90	8.98	17.96	22.45	35.92	44.90	71.84	89.80	134.70	179.60	224.50	269.40	359.20	449.00	2244.99
1.00	9.98	19.96	24.94	39.91	49.89	79.82	99.78	149.67	199.55	249.44	299.33	399.11	498.89	2494.43
1.10	10.98	21.95	27.44	43.90	54.88	87.80	109.76	164.63	219.51	274.39	329.27	439.02	548.78	2743.88
1.20	11.97	23.95	29.93	47.89	59.87	95.79	119.73	179.60	239.47	299.33	359.20	478.93	598.66	2993.32
1.30	12.97	25.94	32.43	51.88	64.86	103.77	129.71	194.57	259.42	324.28	389.13	518.84	648.55	3242.76
1.40	13.97	27.94	34.92	55.88	69.84	111.75	139.69	209.53	279.38	349.22	419.06	558.75	698.44	3492.21
1.50	14.97	29.93	37.42	59.87	74.83	119.73	149.67	224.50	299.33	374.17	449.00	598.66	748.33	3741.65
1.60	15.96	31.93	39.91	63.86	79.82	127.72	159.64	239.47	319.29	399.11	478.93	638.58	798.22	3991.09
1.70	16.96	33.92	42.41	67.85	84.81	135.70	169.62	254.43	339.24	424.05	508.86	678.49	848.11	4240.54
1.80	17.96	35.92	44.90	71.84	89.80	143.68	179.60	269.40	359.20	449.00	538.80	718.40	898.00	4489.98
1.90	18.96	37.92	47.39	75.83	94.79	151.66	189.58	284.37	379.15	473.94	568.73	758.31	947.88	4739.42
2.00	19.96	39.91	49.89	79.82	99.78	159.64	199.55	299.33	399.11	498.89	598.66	798.22	997.77	4988.87
2.10	20.95	41.91	52.38	83.81	104.77	167.63	209.53	314.30	419.06	523.83	628.60	838.13	1047.66	5238.31
2.20	21.95	43.90	54.88	87.80	109.76	175.61	219.51	329.27	439.02	548.78	658.53	878.04	1097.55	5487.75
2.30	22.95	45.90	57.37	91.80	114.74	183.59	229.49	344.23	458.98	573.72	688.46	917.95	1147.44	5737.20
2.40	23.95	47.89	59.87	95.79	119.73	191.57	239.47	359.20	478.93	598.66	718.40	957.86	1197.33	5986.64
2.50	24.94	49.89	62.36	99.78	124.72	199.55	249.44	374.17	498.89	623.61	748.33	997.77	1247.22	6236.08

Table E2 All tested impact velocities, droplets sizes and corresponding Reynolds numbers

Appendix F

Example of results for impact and shedding on hydrophobic (i.e. Teflon that is a standard commercial hydrophobic material) surface

A hydrophobic substrate was prepared with the following parameters:

Material	Static	Advancing	Receding	CAH	State
Teflon320	138° ± 3°	155° ± 3°	111° ± 3°	44°	Wenzel

Table G1 Hydrophobic surface characteristics

The hydrophobic substrate results were midway between both hydrophilic and superhydrophobic substrates.

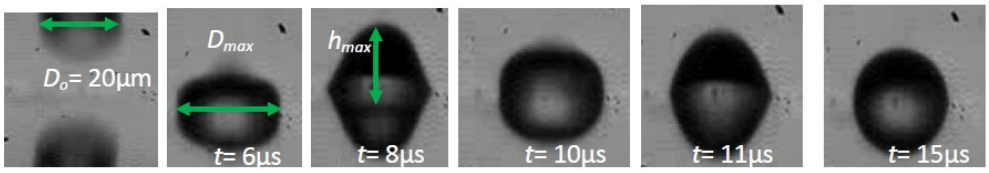

Figure F1 Sequential images of a single 20μm droplet impact on the hydrophobic surface

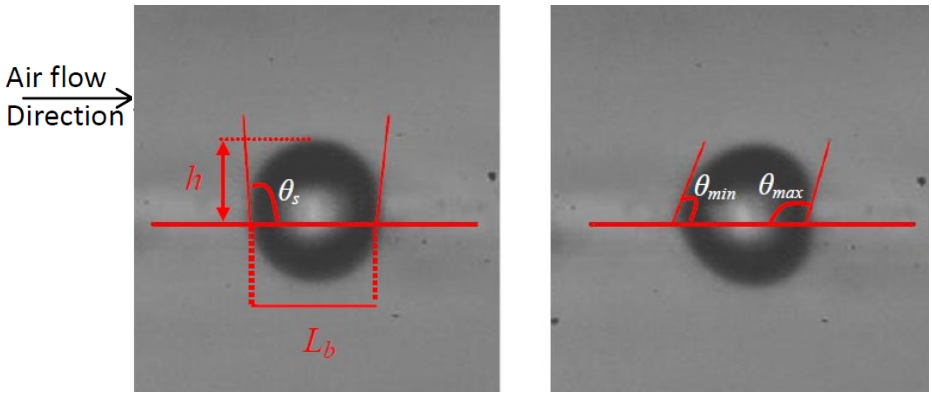

Figure F2 Adhesion parameters for the shedding of a 20 μm droplet on the hydrophobic substrates

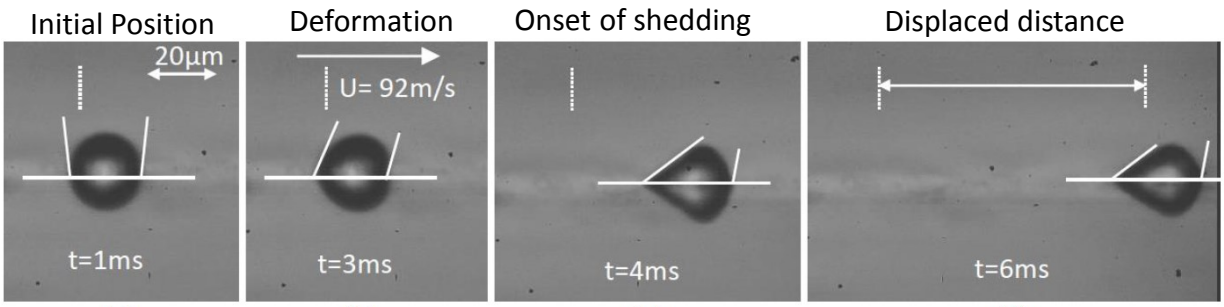

Figure F3 Shedding of a 20 µm water droplet on a hydrophobic surface

Appendix G

Impact velocity effect on the restitution coefficient

The change in the impacting velocity showed almost a negligible effect on the restitution coefficient at such a low impact velocity range, see Figure H1. This confirms that for such a low impact velocity range, the major controlling parameter is the droplets size.

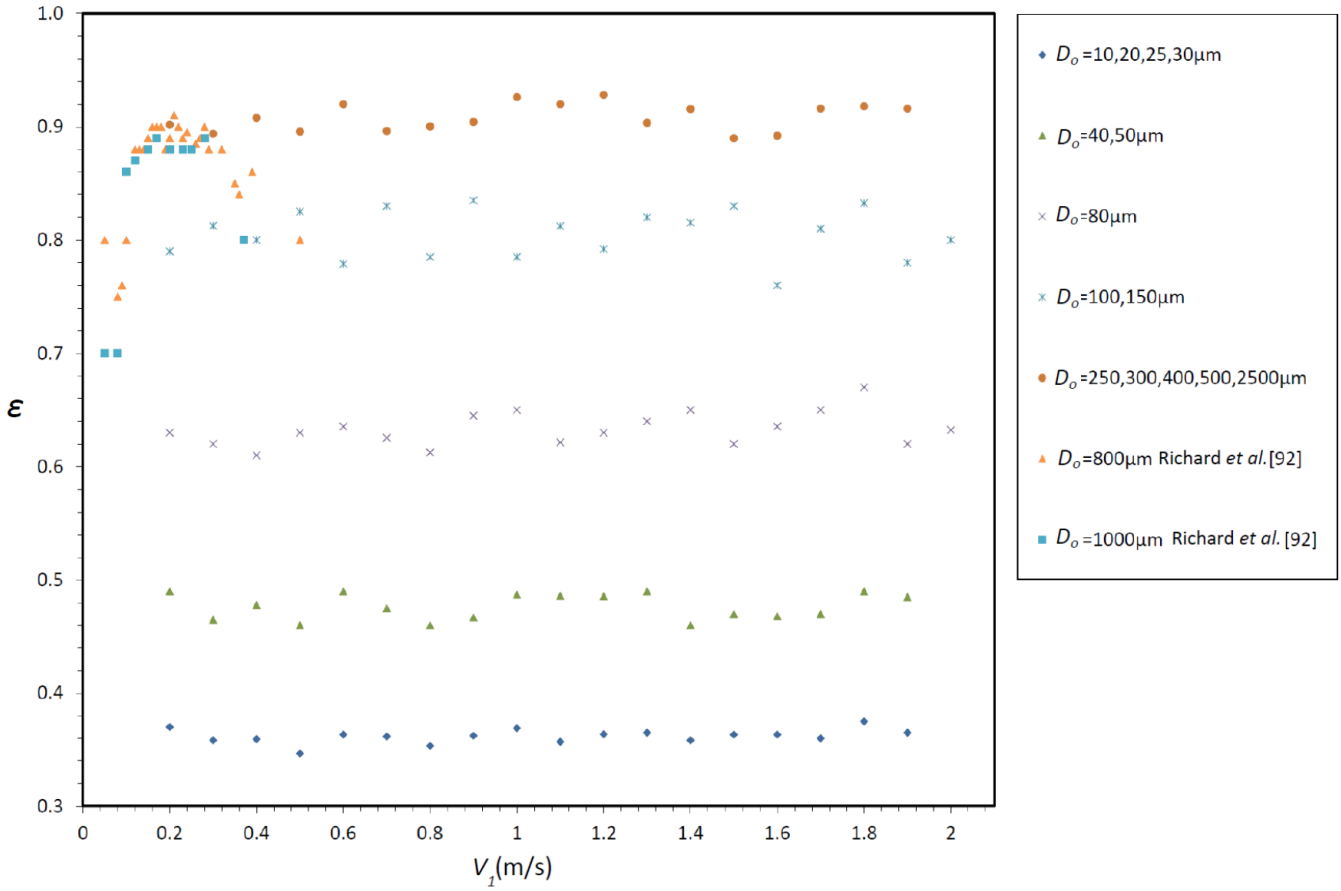

Figure G1 Effect of impact velocity on the restitution coefficient of different droplets